Activation and Inhibition of Autophagy and the Lysosome: Potential Therapeutic Avenues for Prenatal Zika Virus Infection

Team VIRAL

Clara Abdelmalek, Ademide Adeyemo, Aubrey Alexander, Hannah Camacho, Zofia Dyba, Caroline Hobson, Haider Hussain, Erin Li, Soumya Maturi, Arnav Patel, Nandi Patel, Ashley Pocasangre, and Janet Ruan

Gemstone Honors Program

Table of Contents

Chapter 1 - A Humanized Preclinical System Mimics Prenatal Zika Virus Infection

Preprint

Horvath, A. R., Abdelmalek, C. M., Park, E., Alexander, A. P., Maheswaran, S. A., Patel, A. H., Patel, N. G., Ruan, J. E., Adeyemo, A. T., Li, E. C., Helmicki, K. E., Lin, S., Wang, P. C., Li, Z., Wang, L., Gordish-Dressman, H. A., Haydar, T. F., Mansour, T. A., & Kousa, Y. A. (2025). A humanized mouse model system mimics prenatal Zika infection and reveals premature differentiation of neural stem cells. bioRxiv : the preprint server for biology, 2025.02.21.639556. https://doi.org/10.1101/2025.02.21.639556

Authors

Allison R. Horvath,[1, 2†] **Clara M. Abdelmalek**,[1, 2†] Eunbin Park,[1, 2] **Aubrey P. Alexander**,[1, 2] Natthawan Chaimongkol,[1, 2] Jelard Aquino,[3] Whitney Dolan,[3] Martin Gerlein,[1, 2] Sadhana A. Matheswaran,[1, 2] **Arnav H. Patel**,[1, 2] **Nandi G. Patel**,[1, 2] **Janet E. Ruan**,[1, 2] **Ademide T. Adeyemo**,[1, 2] **Erin C. Li**,[1, 2] Katherine E. Helmicki,[1, 2] Stephen Lin,[4] Paul C. Wang,[4, 5] Zhen Li,[2] Li Wang,[2] Heather A. Gordish-Dressman,[6] Wai Lim Ku,[3] Tarik F. Haydar,[2] Tamer A. Mansour,[7, 8] Youssef A. Kousa[1, 2, 9-12]*

[†]Co-first authors

Affiliations

[1]Center for Precision Medicine and Genomics Research and [2]Center for Neuroscience Research, Children's National Research Institute; Washington, DC, 20012.
[3]Department of Medicine, Howard University; Washington, DC, 20060.
[4]Department of Radiology, Howard University; Washington, DC, 20060.
[5]Department of Physics, Fu Jen Catholic University; New Taipei City, Taiwan.
[6]Center of Translational Research, Children's National Hospital; Washington, DC, 20010.
[7]Department of Population Health and Reproduction, University of California Davis; CA, 95616.
[8]Department of Clinical Pathology, College of Medicine, Mansoura University; Egypt.
[9]Division of Neurology, and [10]Division of Neurophysiology, Epilepsy, and Critical Care, Children's National Hospital; Washington, DC, 20010.
[11]Departments of Pediatrics, and [12]Neurology, The George Washington University School of Medicine and Health Sciences; Washington, DC, 20010.
*Corresponding author. Youssef A. Kousa, MS, DO, PhD, Center for Genetic Medicine, Children's National Research and Innovation Campus, 7144 13th Pl NW, Suite 1247, Washington, DC 20012. Phone: (201) 774-7794. Email: YKousa@ChildrensNational.org.

Note: The manuscript included in Chapter 1 differs from the published preprint, as it has undergone further development since publication of the preprint. As of this writing, the updated version of the manuscript is under review at *Nature Communciations*.

1.1 Abstract

Zika virus (**ZIKV**), a mosquito-borne flavivirus, has been found in 87 countries and territories. Global outbreaks peaked in 2016. Prenatal Zika virus infection was found to be associated with microcephaly, arthrogryposis, intracranial calcifications, fetal growth restriction, and fetal demise. The most severely affected children were diagnosed with congenital Zika syndrome, which impacts thousands worldwide. With no approved treatment or preventative measures for Zika virus, future viral outbreaks have the potential to cause epidemic levels of prenatal brain injury, as seen over the past 70 years. Therefore, there is a great need for a reliable and clinically translational experimental system that mimics the human condition of prenatal Zika virus infection. To this end, we developed a novel, humanized, immunocompetent preclinical system of virally induced brain injury from prenatal Zika virus infection, which ranges from mild to severe. Here, we describe the extent to which this system mirrors the human phenotypic spectrum. Using our thorough preclinical system, we find that prenatal Zika virus infection of mice impacts survival rate, anthropometric measurements, tissue formation, and neurological outcomes, all of which are typically affected by prenatal infection. Current and future applications include the identification of genetic or environmental modifiers of brain injury, molecular or mechanistic studies of pathogenesis, and preclinical evaluation of future therapies.

1.2 Introduction

Prenatal viral infections can cause severe damage to the developing brain. Among the most threatening prenatal pathogens, the Zika virus is a positive-stranded RNA flavivirus, mainly transmitted by the *Aedes aegypti* mosquito. It was first isolated in 1947 from a Rhesus monkey in Uganda. Following its discovery, the virus remained largely confined to Africa and parts of Asia until 2015, when it spread to the Americas and caused a major epidemic.[1] Shortly after, it was shown that Zika virus can cross the placental and fetal blood-brain barriers during pregnancy, causing adverse outcomes for a developing fetus.[2] This constituted a Public Health Emergency of International Concern, as declared by the World Health Organization (**WHO**).[3] Severe outcomes after prenatal Zika virus exposure can include microcephaly, ocular abnormalities, congenital contractures, seizures, motor impairments, cognitive deficits, and fetal demise.[4] These outcomes range from infants who are unaffected to those who appear normal at birth but later develop delays, and extending to those who suffer from severe neurological deficits and demise in early life. While the severity of outcomes after prenatal viral infection can vary, the pattern of phenotypes in the most severely affected infants is termed congenital Zika syndrome (**CZS**). Currently, there is no standard of care or treatment for prenatal Zika virus infection, irrespective of degree of injury or severity of outcome. Further, lower levels of Zika virus transmission currently reduce herd immunity and increase risk for large outbreaks in the future.[1,5] Hence, there is a pressing need for translational experimental systems of prenatal infection that effectively mimic humans in terms of viral propagation, brain development and injury, and the spectrum of outcomes.

Animal models are integral in studying and treating viral diseases. These models have enabled the characterization of key features of Zika virus infection, including maternal and fetal viremia, placental injury, fetal resorption, growth restriction, brain malformations, neuronal loss, ocular defects, neurological impairments, and the maternal immune response to infection.[6–18] However, no single model fully replicates human disease, and species-specific differences in antiviral immunity remain an important limitation.

Murine models have been widely used due to their accessibility and experimental flexibility.[6] However, the murine immune response to Zika virus differs significantly from that of humans. In particular, Zika virus is unable to effectively antagonize the murine type I interferon response because its nonstructural protein NS5 cannot degrade mouse STAT2.[19,20] As a result, mice mount a strong interferon-mediated antiviral response that restricts viral replication. To address this limitation, several modified mouse models have been developed including those with suppressed interferon signaling, altered immune pathways, or direct intracranial viral inoculation.[6] These approaches have enabled the study of aspects of human infection, including maternal and fetal viremia,[7,8] fetal resorption,[9] fetal growth restriction,[8,10] brain malformations,[8,10] and ocular defects[10]. Additionally, immunocompetent strains such as SJL mice provided insight into prenatal Zika infection within the context of an intact host immune system and have furthered understanding of viral pathogenesis and neurological injury.[11–18] Despite these advances, fundamental differences in immune responses continue to limit the translational relevance of murine models.

Non-human primate (**NHP**) models have therefore emerged as a critical complementary system, as primates are susceptible to multiple members of the *Flaviviridae* family and more closely reflect the immune interactions observed in human infection.[21,22] Notably, Zika virus can evade the primate type I interferon response through NS5-mediated degradation of STAT2, a mechanism not observed in mice. [19,23] Studies using these models have demonstrated maternal and fetal viremia,[24–26] placental injury,[26,27] fetal demise,[26,28,29] and fetal brain malformations.[26,29,30] Furthermore, experimental approaches such as intravenous inoculation have been used to overcome peripheral antiviral barriers and further characterize the maternal immune response to infection.[10,31–33]

Although each model is informative, no single system captures the full spectrum of outcomes seen after prenatal viral infection or reflects the natural disease pathophysiology. Murine models that artificially suppress or eliminate interferon signaling to permit Zika virus replication may create non-physiological immune states that independently affect placental development, fetal viability, and neurodevelopment. Experimental approaches such as neonatal intracranial or intravenous inoculation bypass the maternal-fetal interface and therefore fail to replicate the timing, route, and immunologic context of natural infection.[10,31–33] While NHP models reproduce many aspects of human pregnancy, their high cost, low throughput, and reliance on specialized infrastructure limit their broader use.[34] Consequently, a translational system capable

of capturing the biological variability of prenatal viral infection, particularly central nervous system (**CNS**) outcomes, remains needed to better understand viral pathogenesis and evaluate candidate therapies for preventing fetal brain injury.

To address these issues, Gorman et al., 2018 developed an experimental system that replicates viral teratogenesis after prenatal Zika virus infection.[35] They created a knock-in (**KI**) mouse model by inserting the human *STAT2* (hSTAT2) gene into the mouse Stat2 locus via homologous recombination. This modification restores the ability of Zika virus to antagonize STAT2 and evade the type I interferon response, thereby enabling viral replication in a manner more consistent with human infection while preserving an intact immune system. The researchers demonstrated that prenatal infection of these humanized mice resulted in placental infection and fetal viremia more effectively than in wildtype C57BL6 controls, all without compromising the immune system.[35] With this murine allele, to extensively characterize neural development and CNS outcomes after prenatal infection, we developed a novel experimental system that evaluates the maternal immune response, viral transmission to the fetal brain, neural injury, brain development, and developmental outcomes.

We used a mouse-adapted Zika virus strain (ZIKV-Dak-MA) for all experiments. This variant was generated by Gorman et al. through serial passage of an African isolate (ZIKV-Dak-41525) in $Rag1^{-/-}$ mice to select mutations that enhance replication in the murine host. The adapted virus carries an NS4B substitution (G18R) that increases viral replication and reduces interferon-β induction, resulting in higher viral burdens in the brain and spleen compared with the parental strain.[35] Importantly, this mutation results in a particularly neurotropic phenotype that promotes efficient CNS infection, enabling robust placental and fetal brain infection in mice without requiring broad immunosuppression. Accordingly, ZIKV-Dak-MA provides a reproducible system for studying vertical transmission and the mechanisms of prenatal viral infection and neural injury.

We selected intraperitoneal (**IP**) inoculation as the route of administration because it provides reliable and systemic delivery through the highly vascularized peritoneal cavity, enabling efficient dissemination of the viral inoculum.[36] The large absorptive surface of the peritoneum supports consistent entry into circulation and accommodates larger injection volumes that are well tolerated in small animals.[36,37] This route is also widely used in experimental virology because of its reproducibility and its ability to cause consistent maternal infection dynamics, making it well suited for establishing robust systemic infection in our model.[36,38] We selected embryonic days 9.5 (**E**9.5) and 10.5 (E10.5) as infection timepoints to model prenatal infection during a developmental window analogous to the end of the first trimester in humans, a critical period for placentation and early neurogenesis. In murine development, placentation is completed at E12.5[39] and neural differentiation begins around E10.5 with the formation of the cortical replate and continues through E17.5.[40] Infecting dams at E9.5 and E10.5 allowed us to assess infection prior to placentation and during the early stages of neural differentiation.

Here, using an immunocompetent humanized preclinical model and an approach that mimics human exposure, we developed a novel experimental system that includes several characteristics previously documented in human prenatal viral infections, including: 1) vertical transmission of virus from dam to fetus,[41,42] 2) detection of comparable amounts of virus in the developing brain,[43,44] 3) dose- and time-dependent brain injury and fetal growth restriction,[45–47] 4) global and regional brain injury, as evaluated prenatally and postnatally,[42,43,48,49] 5) developmental delays in the postnatal period,[50,51] 6) mild neurological deficits in neurological outcomes, [51,52] and 7) overall variability in trajectory, ranging from mild neurological delays to demise. [51,53,54]

In several domains, our system mimics the human condition and sheds light on the pathogenesis of prenatal Zika virus infection. Our manuscript is the first to thoroughly evaluate prenatal brain and postnatal neurological development after transplacental infection. The data and findings have wide-ranging implications for how the brain develops after a prenatal infection. Importantly, these results establish the use of this preclinical system in future research on viral pathogenesis, genetic susceptibility, and testing preventative therapies for prenatal viral infection.

1.3 Methods

1.3.1 Study Design

The objective of this research was to develop and characterize a humanized, immunocompetent, and comprehensive preclinical model of prenatal viral infection. To do so, we designed a series of controlled laboratory experiments involving mock- or ZIKV-infected mice. Mice were randomly assigned either to the mock or infected condition. We evaluated mice at several critical prenatal and postnatal endpoints with a variety of techniques. We withdrew from the study any animals that were chronically lethargic, lost 20% of their baseline weight, were failing to gain weight, or displaying any obvious discomfort (unable to groom, loss of activity, or abnormal movements), and immediately euthanized them. All individual tests and sample sizes are described in supplemental files. All mice were treated independently for statistical analysis and further analyzed for differences between litters.

1.3.2 hSTAT2KI/KI Colony Generation

C57BL/6-Stat2tm1.1(STAT2)Diam/AgsaJ mice were obtained from Jackson Labs and genotyping was completed according to their protocol with primers AGG AGG CTG AGG TAG AAT CAC T (forward) and TGG AGA GAT GGC TCA GAG GT (reverse). All animal care was in accordance with institutional guidelines.

1.3.3 Zika Virus Strain

A mouse-adapted strain of Zika virus was used for all experiments in this study. The strain was generated by the authors of Gorman et al. by passaging an African Zika virus strain (ZIKV-Dak-41525) through Rag1-/- mice to obtain a more virulent, mouse-adapted virus (ZIKV-Dak-MA). Specifically, the mouse-adapted strain contains a mutation in the NS4B protein (G18R) that

enhances viral replication and diminishes interferon-β production, leading to increased viral burden in the brain and spleen compared to the parental wild-type strain.[35]

1.3.4 Zika Virus Preparation

Vero cells were obtained from the American Type Culture Collection (ATCC). At 95% confluency, all media was removed and replaced with Zika virus inoculum (5mL, MOI 0.001, 225mL tissue culture flask). The flask was continuously rocked for 10 mins, and an additional 5mL of FBS-free media was added. Next, the flask was returned to the incubator. After one hour, 45mL of media containing 2.5% FBS was added to the flask. After an additional 48 hrs, 6mL of 10X Sucrose-Phosphate-Glutamate was mixed with the cell supernatant and filtered through a 0.1µm polyethersulfone vacuum filter (Nalgene). The virus was aliquoted into 2mL cryovials, flash frozen in a dry ice/ethanol bath, and stored at -80°C. The concentration of virus was quantified by plaque forming assay.

1.3.5 Zika Virus Infections

$hSTAT2^{KI/KI}$ mice were mated, and vaginal plug was confirmed by E0.5. At E9.5 or E10.5, Zika virus or DPBS control was administered via intraperitoneal injection. For Zika virus infection, virus was thawed quickly at 37°C. All mice were housed in a BSL-2+ animal facility. Dams were monitored for adverse reactions after infection and throughout pregnancy. Embryos were either extracted at E12.5 or E15.5 for prenatal analyses or allowed to deliver for postnatal analyses. There was no evidence of viremia (virus in saliva and blood) at P35 and mice were moved from BSL-2+ containment to the standard housing facility for behavioral/outcome testing.

1.3.6 Gross Measurements/Scoring

CellSens software was used to take images of embryos. ImageJ was used to quantify embryo, placenta, and brain measurements. All measurements were completed by two blind reviewers and averaged, with the exception of MRI data. If the difference between the two measurements differed by 25% or greater, they were analyzed by a third reviewer and averaged. Representative data is shown throughout the manuscript.

1.3.7 Tissue Preparation

For molecular profiling, brain and placenta tissue were harvested and stored in TRIzol. Regions were operationally defined as cortex and hindbrain; the midbrain was not separately identified and may be included within adjacent sections. For histological analysis, brain and placenta tissue were harvested and placed in 4% paraformaldehyde for 24hrs prior to placement into PBS. Tissue was embedded by the Children's National Hospital Pathology Core. Tissue was sectioned with a microtome into 7µm slices for histological analyses.

1.3.8 RNA Isolation

Tissue was collected and stored in 500µL of TRIzol. Next, 100µL of phenol-chloroform was added, and tissues were disrupted using a vortex. Samples were centrifuged for 15 mins at

12,000g. Next, 100µL of the aqueous layer was removed and transferred to a round bottom Qiagen tube with 250µL lysis solution. Samples were run on the QIAcube using the *RNeasy* protocol.

1.3.9 Viral RNA Quantification (TaqMan RT-qPCR)

The genome copy number of Zika virus was determined in several tissues using a one-step RT-qPCR system. Following RNA extraction, RNA concentrations were measured and diluted to 500ng per reaction. The TaqMan™ Fast Virus 1-Step Master Mix (Thermo Fisher Scientific) was used in combination with a newly designed set of TaqMan™ MGB Probe and primers targeting the NS5 (RdRp) gene of Zika virus, developed in this study. Quantification was performed using an RNA standard (custom-made Zika virus RNA, Integrated DNA Technologies (IDT)) curve generated from eight 10-fold serial dilutions ranging from 10^{10} to 10^{3} copies/mL. All qPCR reactions were carried out on a QuantStudio™ 7 Pro Real-Time PCR System (Thermo Fisher Scientific) according to the manufacturer's protocol.

1.3.10 Gene Expression Analysis (SYBR Green RT-qPCR)

SYBR Green-based RT-qPCR was used to quantify the expression of reference and host genes in tissue samples. Following RNA extraction, RNA concentrations were measured and normalized prior to cDNA synthesis. cDNA was generated using the High-Capacity cDNA Reverse Transcription Kit (Thermo Fisher Scientific), with RNA diluted to 20 ng/µL. Quantitative PCR reactions were performed using Applied Biosystems™ Fast SYBR™ Green Master Mix (Thermo Fisher Scientific) according to the manufacturer's protocol. Reference gene amplification was performed using HPRT1 as an endogenous control, and relative quantification was calculated using standard ΔCt-based methods. All reactions were run on a QuantStudio™ 7 Pro Real-Time PCR System (Thermo Fisher Scientific). Statistical significance was assessed using two-way ANOVAs followed by Tukey's multiple-comparisons test on Ct values, and expression is visualized as $\log_2$ (fold change) relative to matched mocks.

1.3.11 H&E Staining

Sectioned tissue was deparaffinized, hydrated, stained with hematoxylin and eosin for nuclei and cytoplasm visualization, dehydrated, and cleared. Slides were mounted with an organic mounting media and #1 cover slips. A Leica DM6B microscope was used to image samples at 10x, as well as 40x for areas of interest.

1.3.12 Nissl Staining

Sectioned tissue was deparaffinized, hydrated, stained with cresyl violet solution for nuclei visualization, dehydrated, and cleared. Slides were mounted with an organic mounting media and #1 cover slips. A Leica DM6B microscope was used to image samples at 10x, as well as 40x for areas of interest.

1.3.13 Immunohistochemistry

The tissue was deparaffinized with xylene and rehydrated. Antigen retrieval was completed using Sodium Citrate Buffer (10mM Sodium Citrate, with or without 0.05% Tween 20, pH 6.0). Blocking was completed using goat serum or bovine serum albumin (BSA), and antibodies were diluted in blocking solution. Nuclei were stained with Hoescht 33342. Virus was stained with Monoclonal Anti-Flavivirus Group Antigen, Clone D1-4G2-4-15 (produced in vitro, VR-1852). The Click-iT™ Plus TUNEL Assay Kit was used for in situ apoptosis detection. Ki67 was stained using recombinant Anti-Ki67 antibody [SP6] (ab16667). TBR2 was stained using Anti-TBR2/Eomes antibody [EPR19012]. TBR1 was stained using Anti-TBR1 antibody [EPR8138(2)]. NeuN was stained using Anti-NeuN antibody, clone A60 (MAB377). MAP2 was stained using Anti-MAP2 antibody (ab5392). A confocal was used to image samples at 40x.

1.3.14 P3-P12 Gross Motor Milestone Testing

Animals were videotaped performing set tasks between P3-P12. Videos were renamed to deidentify conditions and distributed to lab members for blinded evaluation and scoring. Scores from each test were averaged from two trained scorers, unless their scores deviated more than one point and/or 2 seconds, at which point lab members re-scored that video for validation prior to final averaging.

1.3.15 Righting Reflex

The righting reflex is a component of sensory-motor development. The reflex evaluates the ability of a mouse to turn themselves from side-position to prone-position (preferred). The scoring, done with visual inspection, is based on the time it takes to return to prone position, and is as follows (with numerical score): 0-2 seconds (6); 2-4 seconds (5); 4-7 seconds (4); 7-10 seconds (3); 10-15 seconds (2); 15-30 seconds (1); and > 30 seconds (0). Testing was performed at P3, P6, P9, and P12.

1.3.16 Locomotor Movement

Typically developing mice crawl from birth to five days postnatal age, and transition to walking by 10 days postnatally. This sensory-motor assessment places a mouse in an open field for two minutes and evaluates movement. The scoring is as follows (with numerical score): fast crawling/walking (3); crawling with symmetric limb movement (2); slow crawling with asymmetric limb movement (1); and no movement (0). Annotations are made for symmetric limb movement (hindlimbs meet front paws during each step with smooth transition between steps) and asymmetric limb movement (inconsistent paw placement and irregular stepping pattern). Testing was performed at P3, P6, P9, and P12.

1.3.17 Hindlimb Foot Angle

Hindlimb foot angle is an indicator of both sensory-motor and motor development. A picture is taken while a mouse is ambulating in a straight line. Then, the hindlimb foot angle is measured by superimposing a line from the heel to the tip of the middle toe for each foot and identifying

the angle made by the dorsal intersection of these two lines. This evaluation identifies abnormal development of the hindlimb as the mouse matures from crawling to walking. In the typical case, the hindlimb angle is reduced in walking compared to crawling. Testing was performed at P6, P9, and P12.

1.3.18 Hindlimb Strength

The hindlimb suspension test is used to test hindlimb strength. Mice are positioned with their hindlimbs at the rim of a 50mL conical tube. Pads are placed at the bottom of the conical tube to cushion a fall, if needed. Testing is performed with two attempts to determine if a mouse can (with numerical score): hold the position for three seconds (4); weakly maintain the position (3); touch the tube with inconsistency (2); clasp hindlimbs to maintain position (1); or fail to hold the position during any of the attempts (0). Secondary measures included latency to fall (number of seconds). Testing was performed at P6, P9, and P12.

1.3.19 Forelimb Strength

The forelimb suspension test is used to evaluate forelimb and paw strength. Mice are positioned with their forelimbs grasping the rim of a 50mL conical tube. Pads are placed at the bottom of the conical tube to cushion a fall, if needed. Testing is performed with two attempts to determine (with numerical score): normal limb muscle tone (2); muscle weakness (1); or loss of muscle tone or paralysis (0). Secondary measures included latency to fall (number of seconds). Testing was performed at P6, P9, and P12.

1.3.20 Open Field Test

The open field testing examines basic locomotion levels and anxiety-like behavior. Each mouse is gently placed in a corner of an open field Plexiglas clear chamber (21 cm x 21 cm x 30 cm) and allowed to move freely for 30 mins. Locomotion data is collected using the open field activity monitoring system (AccuScan Instruments, Inc. Columbus, OH), which uses photocell emitters and receptors forming an x-y grid of invisible infrared beams at the base of the chambers. As animals move, the analyzer records beam-break data to assess their locomotion patterns. Testing was performed from P35-P40.

1.3.21 Social Interaction Assay

The socialization chamber, used to evaluate social deficits in mice, is composed of three partitions separated by retractable doorways. A single mouse is placed in the middle chamber and allowed to explore freely. After 10 mins, the mouse is given free access to the other two chambers for another 10 mins. After this exploratory period, an inverted empty wire cup (novel object) is placed in one of the chambers, and an unfamiliar (novel) sex- and age-matched mouse (i.e., males with males and females with females) is placed inside an identical inverted wire cup in the other chamber. To control for the possibility of innate side preferences, the wire cups with and without the novel mouse are randomly placed on the left or right chambers, and the placement is changed between mice. After the acclimation period, mice are video recorded for 10

mins. Total time spent sniffing the novel object, novel mouse, as well as the total time spent in each chamber are recorded and scored. Testing was performed from P40-P45.

1.3.22 Rotarod

An accelerating Rotarod apparatus (TSE Instruments) assesses learning, balance, and motor coordination. Rotarod testing involves placing mice on a rotating bar and determining the length of time that they can retain their balance as the rate of rotation is increased. Mice complete one five-minute acclimation session at 15 rotations per minute (RPM) prior to the testing phase. They then undergo two trials (5 mins per trial, 30-minute break between trials) per day for four consecutive days (Max 40 rpm, ~0.2 rpm increase/second). The latencies to fall from the rotarod are recorded. Testing was performed from P50-P55.

1.3.23 Y-Maze

The Y-Maze test evaluates short-term memory and cognition in mice by observing tendencies to explore new areas or stay in a familiar place. The maze consists of three arms (labeled A, B, and C). Mouse movements are tracked over a ten-minute session, and steps are recorded in sets of three to analyze three parameters. Spontaneous Alternation Performance (SAP) measures sequences of three consecutive visits to different arms (ABC, BCA, etc.). Frequency of Alternation Returns (AAR) records non-consecutive same-arm returns (BAB, ACA, etc.). Same Arm Returns (SAR) documents consecutive same-arm returns (BBA, CAA, etc.). No acclimation period was needed. Each mouse underwent one trial. Testing was performed from P116-P120.

1.3.24 Elevated Plus Maze

The elevated plus maze is used to quantify anxiety levels. The maze consists of four arms: two closed arms, and two open arms. Anxious mice usually spend more time on the closed arms, and non-anxious mice tend to explore the open arms more. Mice are placed in the center of the maze for 5 mins of testing. The frequency and duration of entries into each arm are recorded. No acclimation period is needed. Each mouse underwent one trial. Testing was performed from P123-P130.

1.3.25 Magnetic Resonance Imaging (MRI)

MRI was used to investigate the effects of prenatal viral infection on the adult brain. Adult mice were euthanized with isoflurane. After perfusion with PFA and decapitation, mouse heads were stored in PFA and transferred from Children's National Hospital to Howard University for imaging. MRI was performed on a preclinical 9.4T 89mm vertical bore Avance400 system (Bruker BioSpin Corp., Billerica, MA). The mouse heads were placed in a glass vial, immersed in perfluorinated fluid (Galden LS 200, Solvay Specialty Polymers, Alpharetta, GA), and packed with cotton gauze for stability. Whole-brain images were acquired with a 25mm inner diameter RF volume coil. T2-weighted 3D RARE (Rapid Acquisition with Refocused Echoes) fast spin echo anatomical images (TE_{eff} = 36ms, TR = 1500ms, Echo Train Length = 8, FOV = 1.7×1.28×0.72cm, Matrix = 340×256×72, Averages = 10) and 3D spin echo DTI (Diffusion

Tensor Imaging) images (TE = 26.5ms, TR = 275ms, 15 directions, 1 A0 image, single shell, B = 1000s/mm2, FOV = 1.7×1.4×1.4cm, Matri = 128×96×96, Averages = 1) were acquired. Imaging was performed in adulthood, with an age range of five to eight months.

1.3.26 BioRender

Icons used in figures 1, 5, 6, 7, and supplemental figures 1 and 2 were available to the authors through an institutional license to biorender.com.

1.3.27 Statistical Analysis

All statistics were completed using GraphPad Prism software. All data was first assessed for normality. Normal data was analyzed using one-way ANOVA, two-way ANOVA, two-way ANOVA with mixed effects model, Fisher's Exact test, individual unpaired t-test, one-tailed student t-test, or simple linear regression. Nonparametric data was analyzed using the Mann-Whitney test or the Kruskal-Wallis test with Dunn's multiple comparisons. All error bars display the standard error of the mean. Some error bars are not shown because standard error of the mean is smaller than the space covered by the data point. Figure legends indicate the biggest sample sizes (n) used. We reported P values in the New England Journal of Medicine (NEJM) style. A P value < 0.05 was considered statistically significant; we used (*) when $P < 0.05$; (**) when $P < 0.01$; and (***) when $P < 0.001$. All individual tests are described in supplemental files.

1.4 Results

1.4.1 An experimental system of prenatal Zika virus infection in a humanized immunocompetent mouse

In our experimental system, hSTAT2 KI pregnant dams were injected intraperitoneally either with a mouse-adapted Zika virus (ZIKV-infected, various doses) or Dulbecco's phosphate buffered saline (DPBS, mock-infected) on E9.5 or E10.5 (**Fig. 1a**). For prenatal analyses, embryos were harvested on E12.5 or E15.5 and underwent a series of evaluations, including molecular profiling, histological analysis, and anthropometric measurements. For postnatal analyses, mice were monitored for survival and weight progression following birth, assessed for the achievement of gross motor milestones and advanced neurological outcomes, and underwent whole-brain magnetic resonance imaging (MRI).

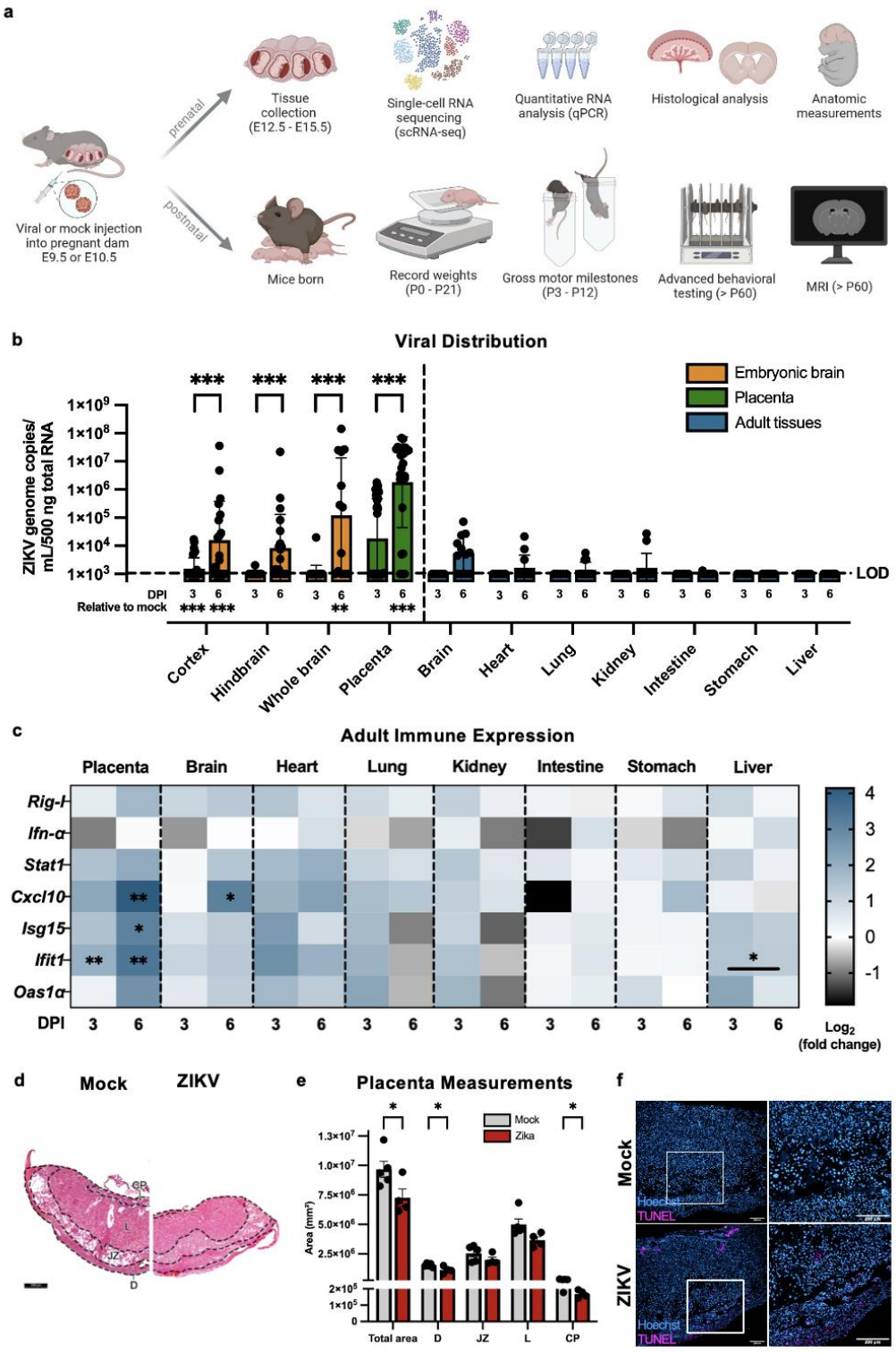

Fig. 1. **Zika virus evades the maternal immune system and injures the placenta. (a)** Experimental design of prenatal Zika virus infection in a humanized immunocompetent (hSTAT2 KI) preclinical system with pipelines for both prenatal and postnatal analyses. Created

in BioRender. Kousa, Y. (2025) https://BioRender.com/z27p901. **(b)** Viral RNA levels in adult and embryonic tissues were measured by TaqMan qPCR at E12.5 (3 DPI) and E15.5 (6 DPI), with viral RNA detected predominantly in embryonic tissues. **(c)** qPCR analysis of type I interferon pathway genes in maternal tissues at E12.5 (3 DPI) and E15.5 (6 DPI) shows the strongest transcriptional induction in placental tissue. **(d)** Representative H&E image of mock- or ZIKV-infected placentas, with designations of regions measured in 1e, infected at E9.5 and collected at E15.5 (scalebar is 500µm). **(e)** Gross measurements of placental histology (total area, decidua (d), junctional zone (JZ), labyrinth (L), and chorionic plate (CP)) confirm that infection at E9.5 causes placental injury by E15.5, most notably within the decidua and chorionic plate. **(f)** Immunostaining of mock- and ZIKV-infected placenta with TUNEL staining identifies DNA breaks resulting from apoptosis. We used (*) when $P < 0.05$; (**) when $P < 0.01$; and (***) when $P < 0.001$.

1.4.2 Zika virus evades the maternal immune system and injures the placenta

Penetration and Injury. In humans, Zika virus has been found to cross the maturing placental and blood-brain barriers, localize to the fetal brain, and cause injury.[43,55] As such, we performed quantitative PCR (qPCR) analyses to determine viral distribution in both males and pregnant females at 3 and 6 days post-infection (DPI) (**Fig. 1b**). Pregnant dams were infected at E9.5, and maternal and fetal tissue were collected at E12.5 (3DPI) and E15.5 (6DPI). Mice were either mock- or ZIKV-infected ($2.33x10^8$ PFU). Using a TaqMan probe system and a limit of detection (LOD) of 10^3 viral particles in 500ng of total RNA, we detected no virus in the adult stomach, heart, intestine, lung, liver, kidney, or brain at 3DPI. Notably, at E12.5, we detected virus in the placenta, embryonic cerebral cortex, hindbrain, and whole brain, indicating maternal systemic infection and viral entry into the brain. Just three days later, at 6DPI we observed some amplification of Zika virus RNA in adult heart, lung, kidney, and brain, as well as a notable increase of viral load in embryonic tissues. There was significantly more virus in embryonic tissues at E15.5 compared to E12.5, unlike in the adult tissues.

Maternal Immune Response. To characterize maternal antiviral signaling following infection, expression of key type I interferon pathway genes was quantified, including markers of viral sensing (*Rig-I*), signaling (*Ifn-α, Stat1*), and interferon-stimulated effector responses (*Cxcl10, Isg15, Ifit1, Oas1a*) (**Fig. 1b**). Pregnant dams were either mock- or ZIKV-infected at E9.5 ($2.33x10^8$ PFU). Maternal tissue, including placenta, liver, brain, stomach, intestine, kidney, lung, and heart were evaluated at E12.5 (3DPI) and E15.5 (6DPI) using qPCR. Transcriptional induction of these antiviral factors was most pronounced in the placenta, whereas most non-placental maternal organs showed minimal or nonsignificant changes. Interestingly, *Ifn-α* did not significantly increase in the placenta, even though downstream antiviral response genes were strongly induced.

Placental Injury. Next, we evaluated the placenta of mock- and ZIKV-infected embryos. We found that ZIKV-infected embryos (E9.5) had smaller placentas, likely resulting from reductions

in the decidua and chorionic plate, most notably in peripheral regions (**Fig. 1d-e**). The junctional zones and labyrinth also trended smaller for ZIKV-infected mice, but did not achieve statistical significance. We performed TUNEL immunostaining to evaluate DNA fragmentation of apoptotic cells and confirmed the decidua and chorionic plate had more dying cells (**Fig. 1f**).

1.4.3 Prenatal Zika virus infection causes brain injury and fetal growth restriction in a dose-dependent manner

It has been shown that NS5 degrades the STAT2 protein in a dose-dependent manner, suggesting that increased viral dose causes higher rates of infection and more frequent and severe brain injury.[19] To evaluate for this relationship in our experimental system, we tested for an association between infectious dose and fetal tissue injury (**Fig. 2a**). We compared five doses of Zika virus infection (7.78×10^7 PFU (200 µL), 1.56×10^8 PFU (400 µL), 2.33×10^8 PFU (600 µL), 3.11×10^8 PFU (800 µL), and 3.89×10^8 PFU (1 mL)) to 100 µL DPBS, with an infection point of E10.5 and a collection point of E15.5. We observed dose-dependent fetal growth restriction and brain volume loss. The size of the placenta did not change with higher infectious doses. We did not find a dose-dependent response in embryo size (2D area measurement), brain area, brain length, or hindbrain width (data not shown). Higher viral doses were associated with higher prenatal lethality, although this trend was not statistically significant by a logrank (Mantel-Cox) test (**Fig. 2b**). Lethality was observed as resorbed clumps of tissue along the uterine horns from aborted embryos. An infectious dose of 2.33×10^8 PFU demonstrated 83% survival with concomitant brain injury and atrophy at E15.5 and was thereby chosen for additional prenatal experiments.

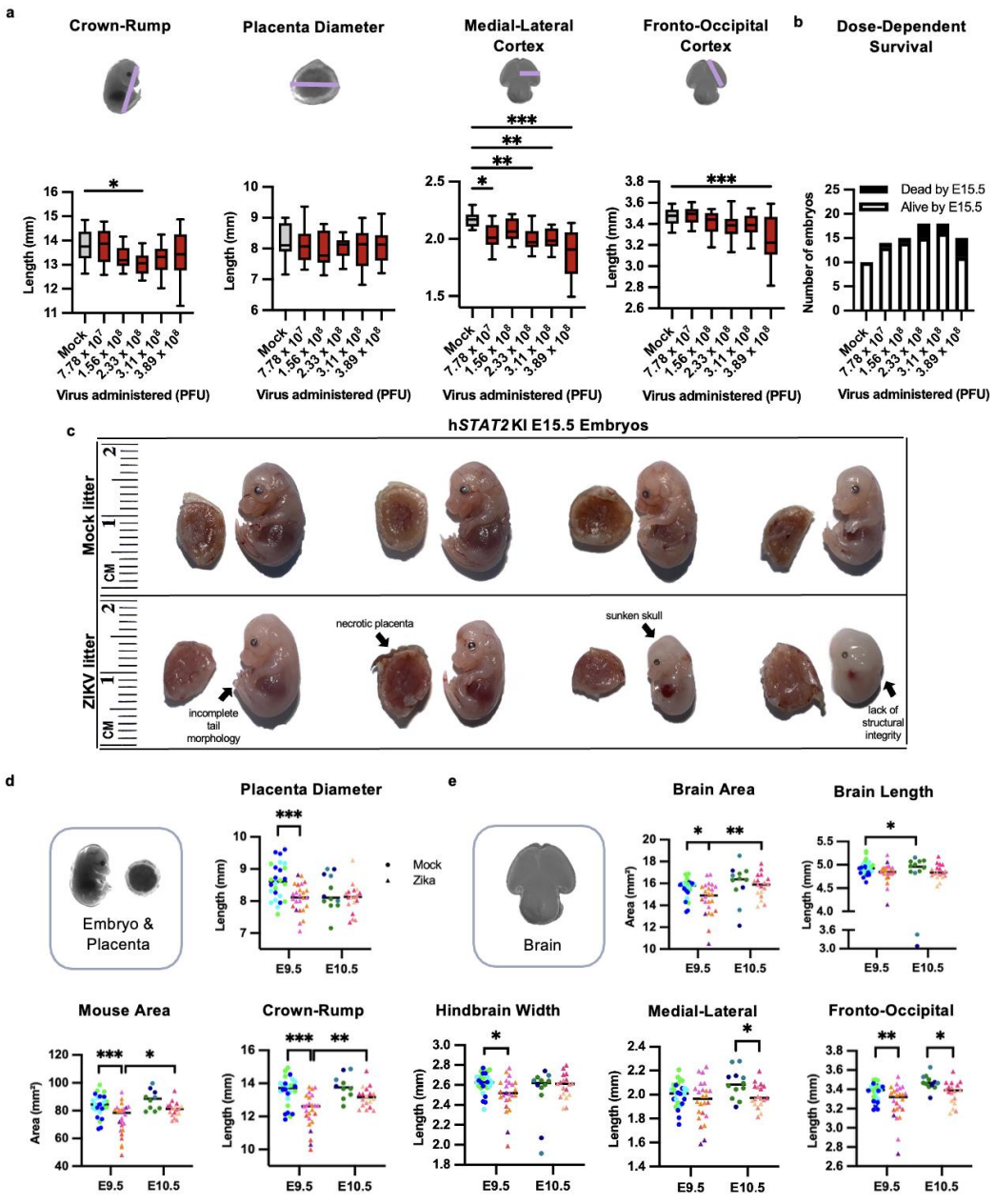

Fig. 2. Prenatal Zika virus infection causes brain injury and fetal growth restriction in a dose- and time-dependent manner, on a clinically relevant spectrum. (a) A dose titration experiment, with infection at E10.5 and embryonic collection at E15.5, demonstrates a dose-dependent response of fetal growth restriction and brain volume loss. Data were analyzed using one-way ANOVA followed by Tukey's multiple comparisons test. **(b)** Embryo loss at varying viral doses at E10.5 showed a trend toward increased lethality with higher viral doses, although not significant by one-way ANOVA. **(c)** Scaled images of mock- or ZIKV-infected embryos (infected at E9.5 and collected at E15.5), demonstrating variability within litters. Injuries observed in the ZIKV-infected litter include (from left to right embryo) an incompletely formed

tail, necrosis of placenta tissue, a collapsed skull, and loss of body wall integrity. **(d-e)** Gross measurements of E15.5 embryos mock- or ZIKV-infected at E9.5 or E10.5. Each color in the figure corresponds to a different litter. There is significant fetal growth restriction, brain volume loss, and placental hypoplasia at E15.5. Earlier infection causes more severe fetal growth restriction and microcephaly. All measurements were performed by two blind reviewers and showed consistent trends, and representative data are shown here. Data were analyzed using two-way ANOVA with a mixed-effects analysis (REML). We used (*) when $P < 0.05$; (**) when $P < 0.01$; and (***) when $P < 0.001$.

1.4.4 Prenatal Zika virus infection causes brain injury and fetal growth restriction in a dose- and time-dependent manner, on a clinically relevant spectrum

Variability in Clinical Outcomes. There are noted differences in how prenatal Zika virus infection can affect humans, with some infants having mild delays by five to six years of age and others having severe brain injury and neurological deficits with prenatal onset.[51,53,54] To determine if our experimental system produced a similar spectrum of outcomes, we evaluated how a single viral dose and time of infection affected embryos and led to variability in prenatal injury (**Fig. 2c**). We injected pregnant dams with DPBS or $2.33x10^8$ PFU of Zika virus at E9.5 and observed the resulting injury at E15.5. We observed a spectrum of phenotypes ranging from mild to severe fetal teratogenesis among prenatally infected embryos, even when comparing littermates. For example, **Fig. 2c** shows a representative mock (top row) and ZIKV-infected litter (bottom row); while some embryos appeared unaffected by visual inspection, others lacked several anatomical structures and/or displayed embryonic malformations. Such abnormalities included incomplete formation of the tail, necrosis of the placenta, sunken skull shape, and lack of structural integrity of the body wall and limbs. The location of the embryo within the uterine horn did not seem to correlate with severity of injury (data not shown).

Time-Dependent Growth Restriction and Microcephaly. Beyond visual inspection, we performed detailed quantitative measurements to evaluate each mock- or ZIKV-infected embryo in our experiment. To perform this work, we developed a protocol to evaluate embryonic growth at E15.5 (after injection at E9.5 or E10.5) using a series of 2D measurements modeled after standard human prenatal care. As seen in humans, prenatal infection at E9.5 resulted in embryos with significant growth restriction (smaller bodies), brain volume loss, and smaller placentas at E15.5 (**Fig. 2d-e**). Notably, infection just one day later, at E10.5, resulted in more limited effects between mock-and ZIKV-infected mice. A two-way ANOVA with a mixed model confirmed that viral infection at E9.5 caused significant volume loss in mouse area, crown-rump length, brain area, medial-lateral length, and fronto-occipital length compared to infection at E10.5. This is comparable to the human condition, where earlier infection has been associated with increased fetal teratogenicity and demise.[45] Expected biological variability was observed within mock- and ZIKV-infected litters for infections at both timepoints. We continued our studies with E9.5 infections to comprehensively evaluate the extent of brain injury and neurological disabilities,

both prenatally and postnatally. Data were evaluated by litter to account for potential effects of maternal age and were found to be normally distributed (data not shown).

1.4.5 Zika virus causes global and regional injury in the developing brain

Global and Regional Brain Injury. In addition to global brain atrophy leading to volume loss, prenatally exposed infants often also suffer from structure-specific injury and focal neurological deficits. To assess for these injuries in our mice, we collected data from three coronal regions of the forebrain and midbrain (anterior and posterior), representative of the cerebrum, with the most observable, consistent, and severe injury (**Fig. 3**). Histological analyses showed injury in the developing brain after infection at E9.5, particularly manifested as cortical thinning, neuronal dropout in the pons, and reduced cellularity in multiple thalamic nuclei, including the lateral geniculate nucleus (**Fig 3a-c**). To quantitatively determine if specific brain structures were more severely affected than others, we measured the area of the lateral ventricle, germinal zone, cortical plate, midbrain, and hemispheres (**Fig. 3d-f**). We found that infection results in significant structure- and region-specific volume loss affecting the cortical plate, germinal zone, midbrain, and overall hemisphere. Differences in the size of these structures were not uniform among the three brain regions evaluated.

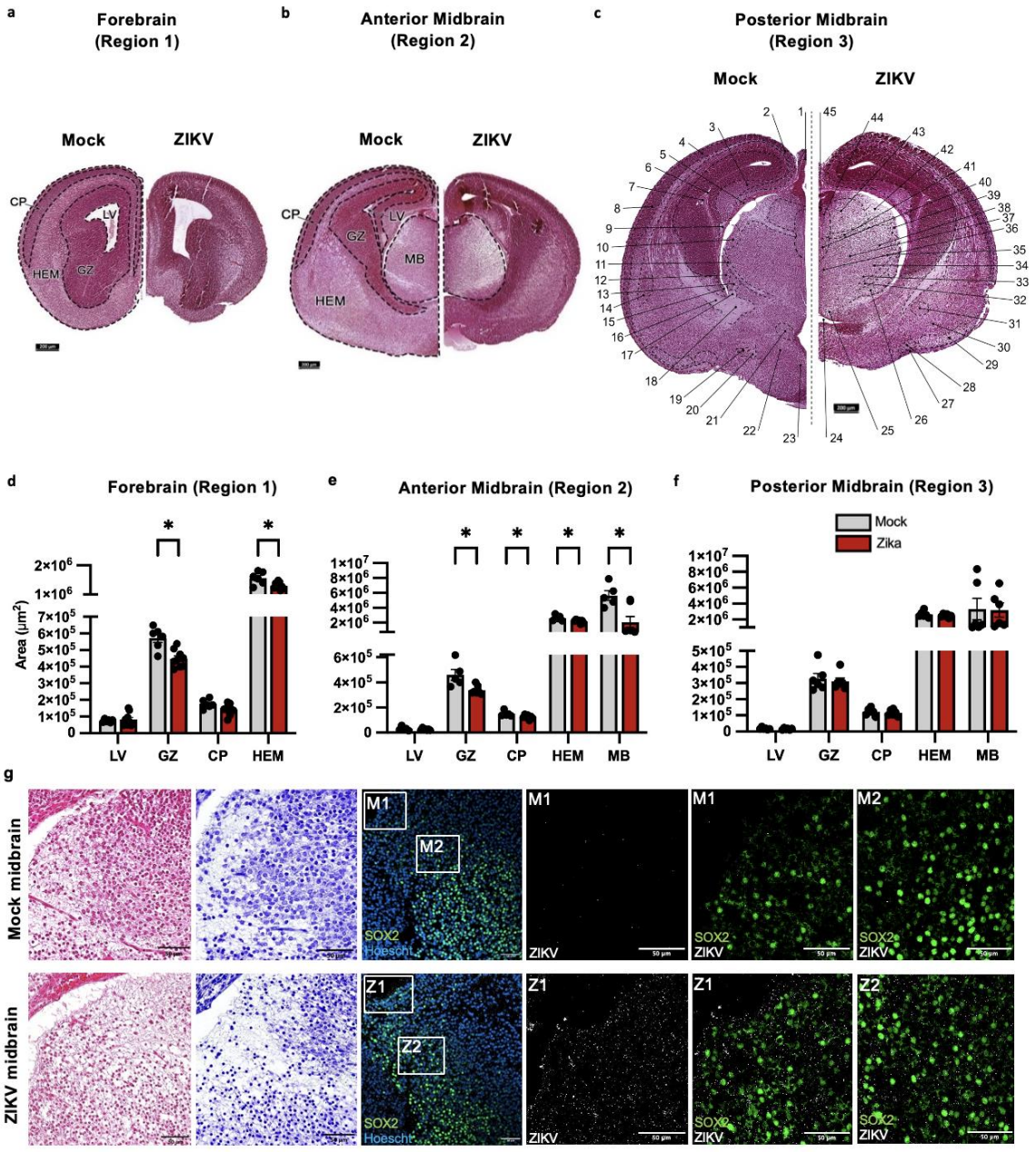

Fig. 3. Zika virus causes global and regional injury in the developing brain. (a-c) Scaled images of mock- or ZIKV-infected brains in the forebrain (region 1), anterior midbrain (region 2), and posterior midbrain (region 3), infected at E9.5 and collected at E15.5 (scalebars are 200µm). Hematoxylin & eosin staining reveals global cerebral loss, cortical thinning, neuronal dropout in the pons, and reduced cellularity in the thalamus. **(c)** 1) Pineal gland, 2) Retrosplenial cortex, 3) Hippocampus, 4) Somatosensory cortex, 5) Dentate gyrus, 6) Lateral ventricle, posterior horn, 7) Choroid plexus, 8) Piriform cortex, 9) Fimbria, 10) Dorsal lateral geniculate nucleus, 11) External medullary lamina, 12) Ventral lateral geniculate nucleus, 13) Reticular thalamic nucleus, 14) Lateral amygdaloid nucleus, 15) Stria terminalis, 16) Internal capsule, 17)

Lenticular fasciculus, 18) Cerebral peduncle, 19) Medial forebrain bundle, 20) Fornix, 21) Paraventricular hypothalamic nucleus, 22) Anterodorsal hypothalamic nucleus, 23) Anteroventral hypothalamic nucleus, 24) Third ventricle, 25) Reuniens thalamic nucleus, 26) Zona incerta, 27) Lateral olfactory tract, 28) Nucleus of lateral olfactory tract, 29) Cortical amygdaloid nucleus, 30) Anterior amygdaloid area, 31) Central amygdaloid nucleus, 32) Medial lemniscus, 33) Ventral medial thalamic nucleus, 34) Ventral posterior medial thalamic nucleus, 35) Ventral posterior lateral thalamic nucleus, 36) Central medial thalamic nucleus, 37) Mediodorsal thalamic nucleus, 38) Posterior thalamic nucleus, 39) Lateral posterior thalamic nucleus, 40) Paraventricular thalamic nucleus, 41) Fasciculus retroflexus, 42) Stria medullaris, 43) Lateral habenular nucleus, 44) Medial habenular nucleus, 45) Habenular commissure. **(d-f)** Brain area measurements of the lateral ventricle (LV), germinal zone (GZ), cortical plate (CP), midbrain (MB), and hemisphere (HEM), taken from three representative forebrain and midbrain regions. Data reveals that infection results in significant structure and region-specific volume loss affecting the cortical plate, germinal zone, midbrain, and overall hemisphere. **(g)** H&E and Nissl staining of coronal sections of mock- or ZIKV-infected fetal brains show reduced cellularity in the lateral habenula of the midbrain. Immunostaining with a flavivirus antibody, 4G2, reveals viral protein in the midbrain. Some of this viral protein appears in neural stem cells, marked by SOX2 (scalebars are 50μm).

Cellular Injury. Similarly, in fetal brain tissues, hematoxylin and eosin (H&E) and Nissl staining revealed reduced cellularity throughout the brain, most notably affecting the lateral habenula in both afferent (stria medullaris) and efferent (fasciculus retroflexus) pathways (**Fig. 3g**). Immunostaining showed Zika virus penetrating the midbrain, with some viral protein colocalizing with neural stem cells (marked by SOX2) by E15.5, six days after infection (**Fig. 3g Z1**/**Z2**).

1.4.6 Zika virus may induce differential developmental expression in the embryonic brain

Differential Expression. To assess how Zika virus infection alters the gene expression patterns that underlie brain development, we performed qPCR on cortical and hindbrain tissues infected at E9.5 and collected at E12.5 (3DPI) and E15.5 (6DPI) (**Fig. 4a**). This analysis included markers of radial glia (*Sox2*, *Hes1*, *Nestin*, *Emx1*, *Ki67*), neuroblasts (*Eomes*/Tbr2, *Dlx1*, *Dcx*, *Ncam1*, *Tubb3*), and neurons (*Tbr1*, *Rbnfox3*/NeuN, *Map2*). These data suggest some differences between mock- and ZIKV-infected hindbrains, with more limited differences observed in the cortex. The data also indicate variation associated with developmental stages (E12.5 and E15.5).

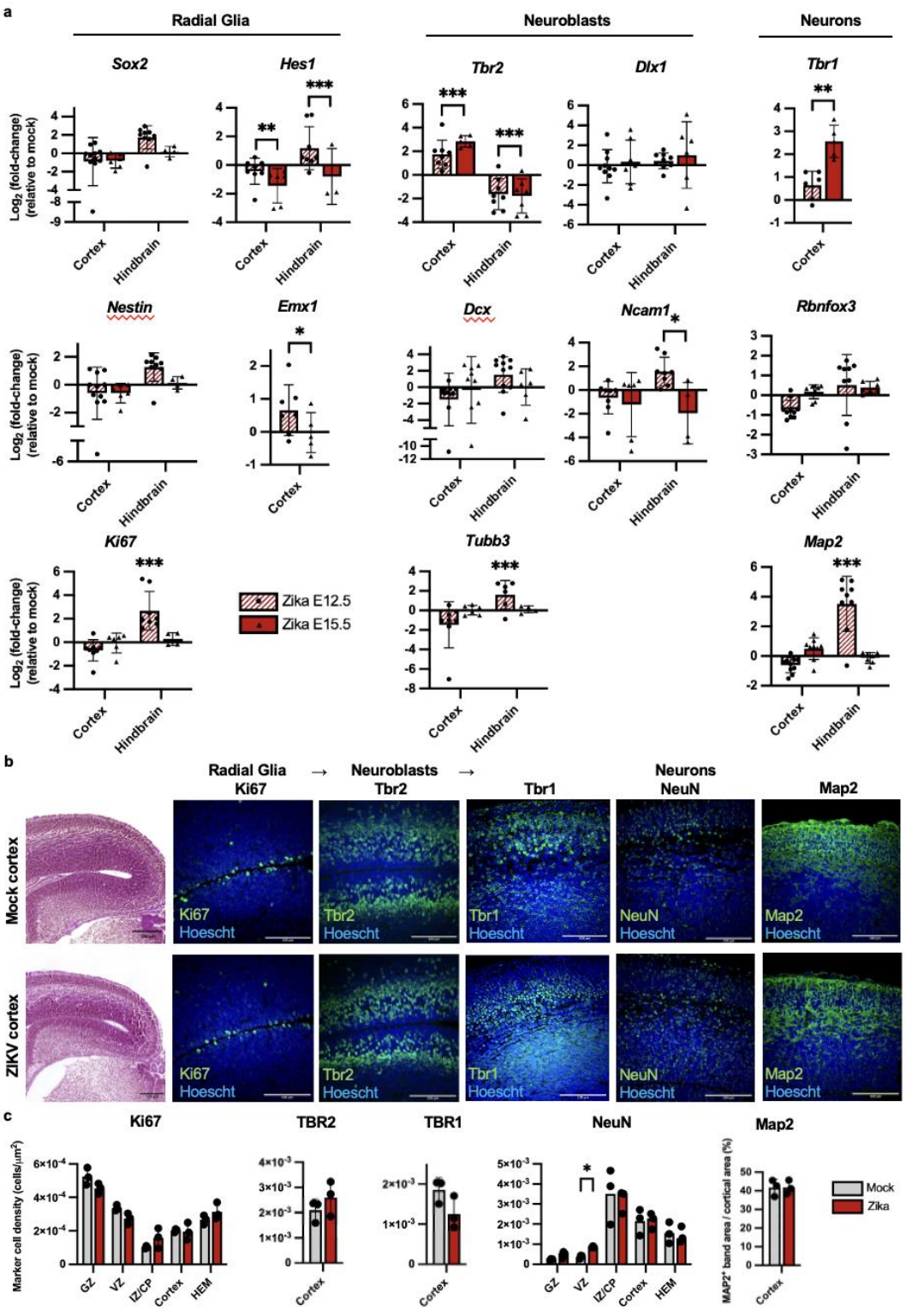

Fig. 4. Zika virus may induce differential developmental expression in the embryonic brain. (a) qPCR analysis of gene expression for markers indicative of radial glia (*Sox2*, *Hes1*, *Nestin*, *Emx1*, *Ki67*), neuroblasts (*Eomes*/Tbr2, *Dlx1*, *Dcx*, *Ncam1*, *Tubb3*), and neurons (*Tbr1*,

Rbnfox3/NeuN, *Map2*) in the cortex and hindbrain at E12.5 and E15.5. Asterisks denote statistically significant differences relative to matched mock controls, while bracketed comparisons indicate significant differences between timepoints (3DPI vs 6DPI). **(b)** H&E reveals thinning of the cortex in ZIKV-infected samples. Cortical immunostaining was performed for neural cell populations, including radial glia/proliferating cells (Ki67), intermediate progenitors (TBR2), and neurons (TBR1, NeuN, MAP2), (scalebars are 150μm). **(c)** Semi-quantification of immunofluorescence.

Cellular Injury. To determine whether transcriptional changes were accompanied by corresponding changes at the protein level, we performed histological analyses on mock- and ZIKV-infected cortexes infected at E9.5 and collected at E15.5 (**Fig. 4b-c**). H&E staining demonstrated cortical thinning in ZIKV-infected embryos relative to controls (**Fig. 4b**). Cortical immunostaining evaluated radial glia (Ki67), neuroblasts (Tbr2), and neurons (Tbr1, NeuN, Map2), and these markers were semi-quantified in **Fig. 4c**. Together, these molecular and cellular data may indicate that Zika virus infection disrupts coordinated gene expression patterns in the embryonic brain.

1.4.7 Prenatal Zika virus infection may cause developmental delays and neurological deficits

Developmental Delays. Infants prenatally exposed to Zika virus often experience developmental delays in early childhood.[50,51] To evaluate for these outcomes in our experimental system, we developed a postnatal analysis pipeline, adapted from a published protocol (**Fig. 5a**).[56] When mice were infected with the viral dose of $2.33x10^8$ PFU at E9.5, only 1/7 pregnant dams carried viable embryos to term. Therefore, we used a lower viral infectious dose ($7.78x10^7$ PFU) to study postnatal development. By postnatal day 12 (**P**12), 62% of prenatally infected mice died (**Fig. 5b**). ZIKV-infected mice also exhibited reduced body weight, as confirmed by two-way ANOVA (**Fig. 5c**). Gross motor milestone testing between P3-P12 (during infancy) revealed mild developmental delays in prenatally infected mice (**Fig. 5d-h**). Testing included the righting reflex (**5d**), locomotion (**5e**), foot angle (**5f**), hindlimb suspension (**5g**), and forelimb suspension (**5h**). At all timepoints, infected mice performed statistically worse than controls in locomotor movement. At various timepoints, infected mice were delayed in righting reflex and hindlimb strength compared to controls. There was no significant difference in foot angle or forelimb strength tests. To evaluate whether postnatal lethality of the most severely affected mice skewed developmental testing, we also analyzed the dataset after excluding mice that died before P12. In this subset, neurological delays and disabilities were less pronounced, indicating that early mortality disproportionately affected the most severely impacted animals (**Supplemental Fig. 1**). Data were evaluated by litter to account for potential effects of maternal age and were found to be normally distributed (data not shown).

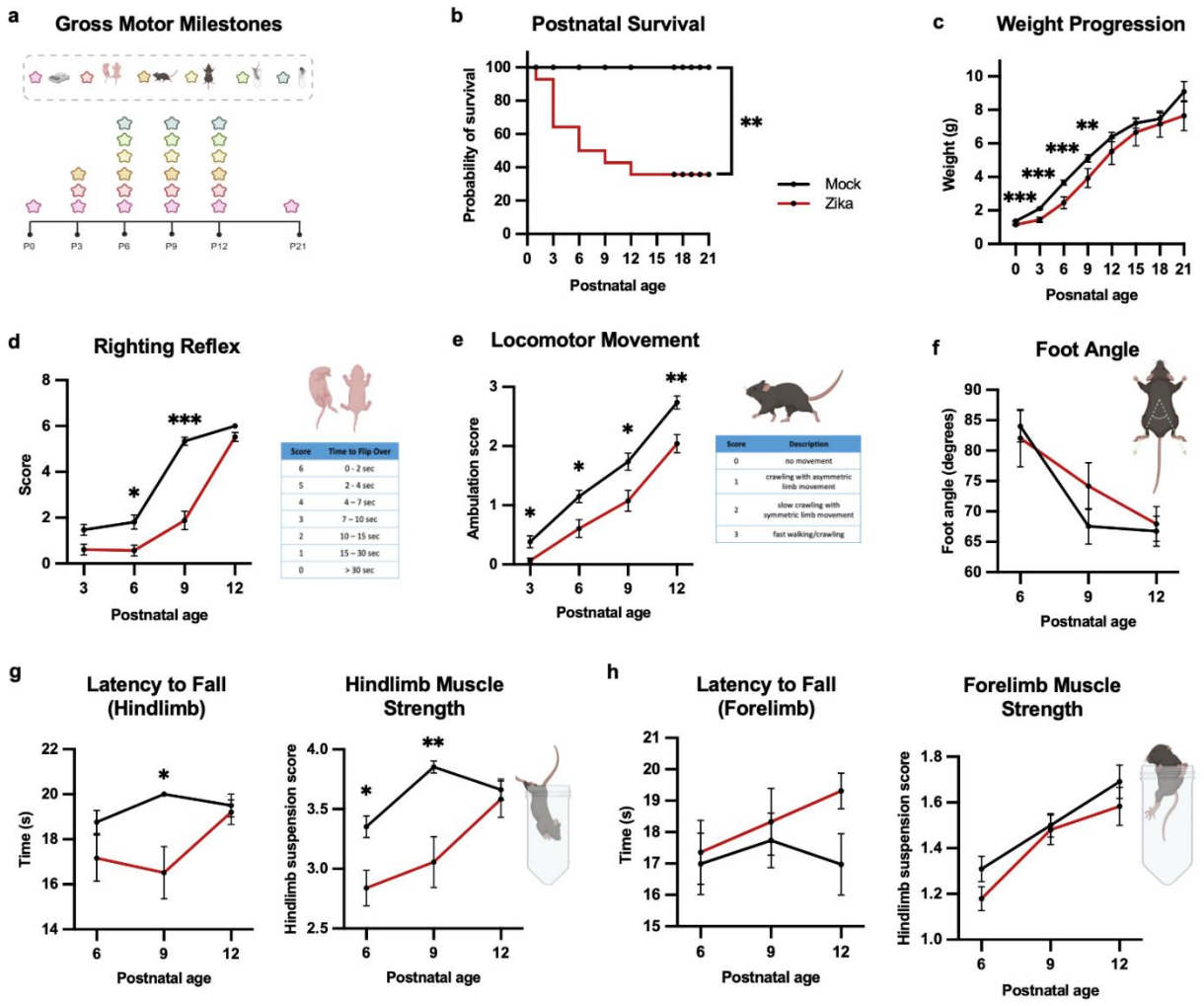

Fig. 5. Prenatal Zika virus infection may cause developmental delays and premature death. **(a)** Postnatal analysis pipeline for mice mock- or ZIKV-infected at E9.5. Gross motor milestone tests are performed from P3-P12. Created in BioRender. Kousa, Y. (2025) https://BioRender.com/q46t306. **(b)** Kaplan-Meier curve of mock- or ZIKV-infected mice from P0-P21 shows death of 62% of infected mice by P12. **(c)** Weight progression of mock- or ZIKV-infected mice from P0-P21. ZIKV-infected mice consistently weighed less than controls, and there is a significant difference between the mock- or ZIKV-infected mice for the rate of weight gain. **(d-h)** Behavioral testing evaluated righting reflex **(d)**, locomotor movement **(e)**, foot angle while walking **(f)**, hindlimb suspension **(g)**, and forelimb suspension **(h)**. At all timepoints, infected mice had delays in locomotor movement. At various timepoints, infected mice demonstrated delays in the righting reflex and hindlimb strength. There was no significant difference in foot angle or forelimb suspension. We used (*) when $P < 0.05$; (**) when $P < 0.01$; and (***) when $P < 0.001$.

Neurological Outcomes. Motor, Anxiety, and Social Testing. In addition to gross motor delays, prenatally infected infants also often suffer motor, social, and learning deficits later in

childhood.[51,52] We evaluated for such deficits among the mice that survived past weaning (P21) using advanced behavior tests, during both late adolescence (P35-P60) and adulthood (> P60) (**Fig. 6a**). First, mice underwent open field testing at P35-P40 to examine basic locomotion and anxiety-like behavior (**Fig. 6b**, full dataset in **Supplemental Fig. 2**). No significant differences between groups were observed, which may be attributed to high variability between mice or the potential loss of the most severely affected individuals prior to assessment. However, some tendencies did trend differently for infected mice such as clockwise rotations, rest time, and jump count (**Fig. 6b**).

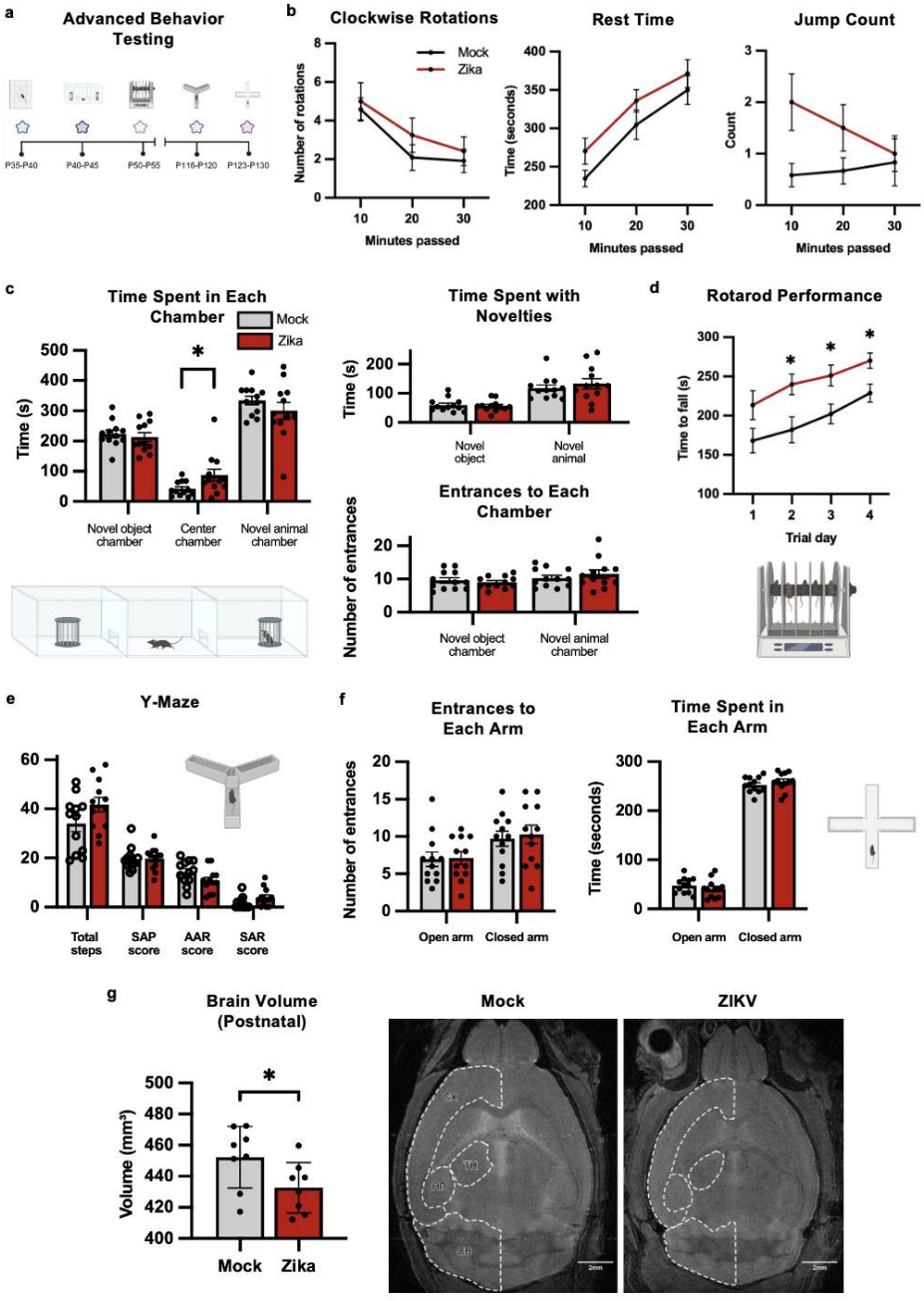

Fig. 6. Prenatal Zika virus infection may cause differences in neurological outcomes. (a) Postnatal analysis pipeline for mice mock- or ZIKV-infected at E9.5. Advanced behavioral tests are performed from P35-P130. Created in BioRender. Kousa, Y. (2025) https://BioRender.com/u18z535. **(b)** Open field test was used to examine locomotion and stereotypical movements of mice. No statistical differences were observed, although some scores, such as for clockwise rotations, rest time, and jump count trended higher for infected mice. Full dataset in Supplemental Fig. 2. **(c)** We evaluated mice for social deficits using the social interaction assay. There was no significant difference between groups in time spent with the novel object or novel animal, nor the number of entrances to either chamber. However, ZIKV-infected mice spent significantly more time in the empty center chamber. **(d)** To assess balance and motor coordination and learning, we evaluated the latency to fall from the rotarod from P50-P55. ZIKV-infected mice stayed on the rotating rod longer than controls. **(e)** To test for differences in short-term memory, we performed the Y-Maze test. There was no significant difference between mock- and ZIKV-infected mice. **(f)** To further evaluate for anxiety, we performed the elevated plus maze test. There was no significant difference between mock- or ZIKV-infected mice. **(g)** MRI of adult brains reveals postnatal brain volume loss, potentially affecting the cortex (CX), thalamus (TH), hippocampus (HP), and cerebellum (CB) (scalebars are 2mm). We used (*) when $P < 0.05$; (**) when $P < 0.01$; and (***) when $P < 0.001$.

To evaluate for social deficits, mice underwent the 3-chamber socialization assay at P40-P45, which evaluates preferences for novel objects versus novel live animals (age- and sex-matched to subject) (**Fig. 6c**). There was no significant difference observed in the time spent with each novelty or the number of entrances to each chamber. However, prenatally infected mice spent significantly more time in the center chamber (alone) than the outside chambers with the novel object or novel animal. At P50-P55, the rotarod test was completed over four days to evaluate both motor ability and learning potential (**Fig. 6d**). Compared to controls, prenatally infected mice remained on the rotarod for a longer amount of time before falling. There was no significant difference in the change over time in the performance of the two groups by a two-way ANOVA mixed model, indicating that there was no difference in the potential for motor learning between groups. To evaluate for short-term memory loss in prenatally infected mice, we performed the Y-Maze test from P116-P120 (**Fig. 6e**). We observed no significant difference in short-term memory between mock- or ZIKV-infected mice.

Given that infants with a history of prenatal viral infection may have social-emotional deficits, we evaluated for anxiety in our mice.[57] We performed the elevated plus maze test at P123-P130 (**Fig. 6f**). However, there was no difference in time spent in enclosed (safe) versus open (exploration) arms between mock- or ZIKV-infected mice.

Postnatal Microcephaly. MRI studies of children with congenital Zika syndrome commonly report a reduction in postnatal brain volume.[4] To characterize postnatal brain development in our model, we performed whole-brain MRI on mock- or ZIKV-infected mice in adulthood (**Fig. 6g**).

ZIKV-infected mice demonstrated a significant loss in brain volume, potentially affecting the cortex (CX), thalamus (TH), hippocampus (HP), and cerebellum (CB).

1.4.8 Prenatally infected females may have enhanced postnatal survival

In humans, outcomes of prenatal viral infection may differ by sex.[58] We evaluated for sex-specific differences in fetal growth restriction and brain injury for the embryos infected at E9.5 and collected at E15.5 shown in Fig. 2c-e (**Fig. 7**). Differences in measurements correlated to infection status, as previously shown, are irrespective of sex. Further, no statistical differences in the outcomes of infection were observed between sexes by a two-way ANOVA (**Fig. 7a-b**). However, from E15.5 to P21, the percentage of males decreased from 65% to 16% (**Fig. 7c**). Fisher's Exact Test shows a statistically significant difference in distribution between sex of mock- or ZIKV-infected mice by P21, indicating a potential postnatal survival advantage for the female sex.

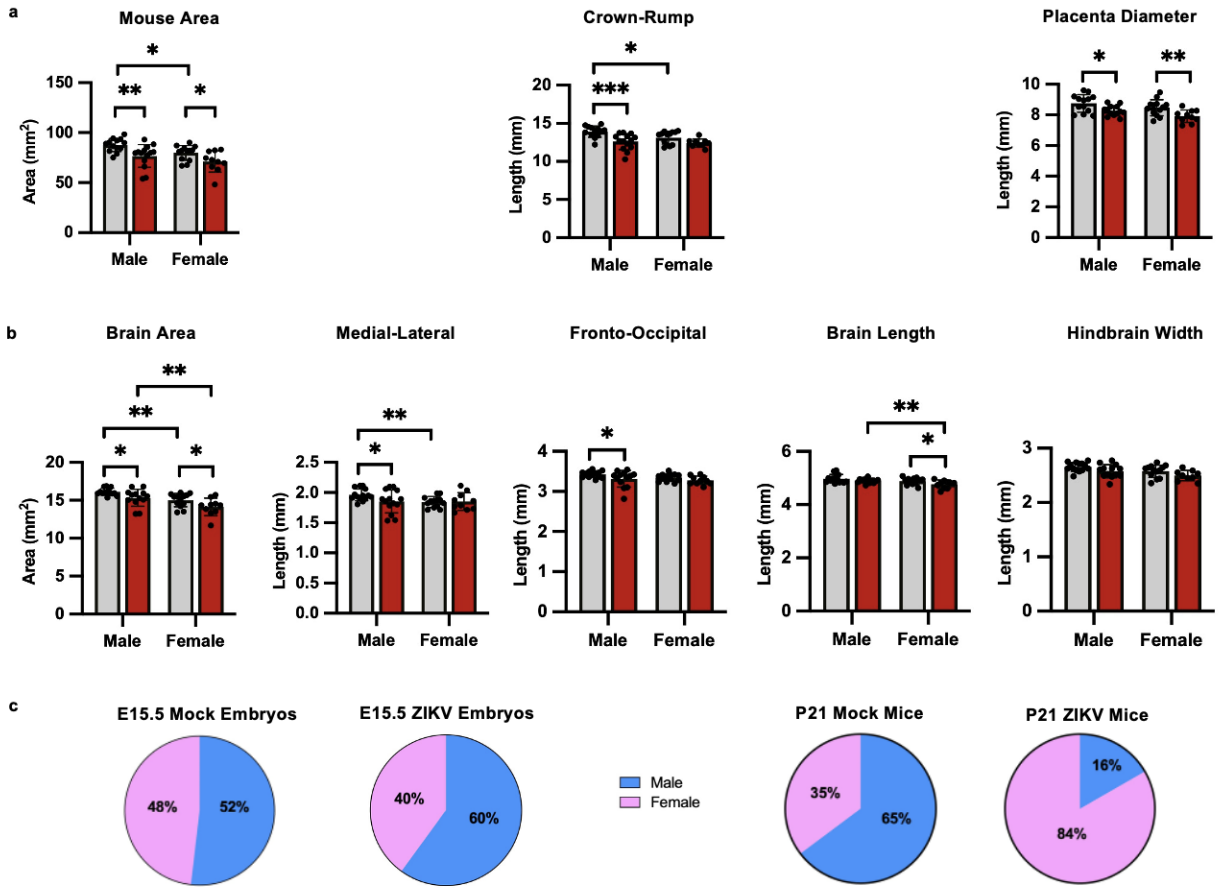

Fig. 7. Prenatally infected females may have enhanced postnatal survival. (a-b) Data from Figure 2c-e, separated and evaluated by sex. Sex and infection condition were significant predictors of prenatal gross measurements individually, but the interaction between sex and infection condition was not significantly correlated with outcome.

1.4.9 Advanced maternal age contributes to adverse prenatal outcomes, particularly at higher viral doses

It is known that the immune system can become weaker and more susceptible to viruses with age, as with West Nile virus.[59] Thus far, the effects of maternal and paternal age on outcomes of prenatal viral infection have not been investigated in humans. While our study was not designed to capture discrepancies due to maternal age, we observed maternal age-associated trends in the outcomes of our dose titration experiment. To investigate this, we retrospectively evaluated the E10.5 dose titration experiment shown in Fig. 2a by litter to determine the effects of differing maternal age (data not shown). Advanced maternal age contributed to adverse prenatal outcomes, particularly at higher viral doses.

1.5 Discussion

Here, we establish a humanized, immunocompetent preclinical system that replicates key features of prenatal Zika virus infection, including transplacental transmission, fetal brain infection, and a spectrum of developmental and neurological outcomes. This model reproduces clinically relevant phenotypes such as fetal growth restriction, microcephaly, spontaneous abortion, and postnatal neurological impairment, while preserving an intact immune system. [45–47,53]

A major strength of this system is its ability to model infection in a biologically relevant context. By combining a human STAT2 knock-in background with a neurotropic, mouse-adapted Zika strain and intraperitoneal inoculation, we achieved consistent maternal infection and efficient placental and fetal transmission. Viral RNA and protein are localized predominantly to embryonic tissues, with levels approximating those reported in human fetal infection, supporting the translational relevance of this model. Although direct viral dose comparisons across species are not possible, the TaqMan-based approach enables sensitive detection of viral RNA and supports approximation of clinically relevant viral burdens.[43,52]

Molecular and immunological profiling further support the validity of this system. Antiviral signaling was most prominent in the placenta, with robust induction of interferon-stimulated genes, while most maternal organs showed minimal changes. Notably, Ifn-α expression was not significantly elevated at the measured timepoints despite downstream activation, suggesting temporally restricted or transient upstream signaling. Together, these findings identify the placenta as a central site of immune activation and support the preservation of an intact immune response in this model. Importantly, the observed interferon-associated transcriptional profile is consistent with an intact innate immune response in C57BL/6 mice, supporting the interpretation that this model remains immunocompetent.[35] Further placental analyses revealed structural injury and increased cell death in the decidua and chorionic plate, supporting the placenta as both a central site of immune activation and a likely contributor to downstream fetal injury.[33,43,60–62]

Our findings demonstrate that both viral dose and developmental timing are key determinants of disease severity. Increasing viral dose was associated with greater fetal growth restriction, brain injury, and lethality, indicating a dose-dependent effect on developmental outcomes. In parallel, infection at E9.5 resulted in significant growth restriction and brain volume loss, whereas infection at E10.5 produced more limited, parameter-specific effects. This narrow developmental window likely reflects the vulnerability of neural stem cell populations during early neurogenesis.[4,39,40,45,63,64]

In addition to global effects on fetal growth, this model reproduced both regional brain injury and marked variability in outcome. Within litters, embryos showed a spectrum of phenotypic severity despite identical experimental exposure, consistent with the heterogeneity observed in human prenatal infection. Histological analyses identified reduced cellularity in discrete regions including the thalamus and lateral habenular region, supporting region-specific susceptibility to injury. These findings align with prior reports that the cortex, germinal zones, and thalamic structures are especially vulnerable during prenatal infection.[44,48,65–72]

At the molecular and cellular level, qPCR and immunostaining analyses suggest region- and stage-dependent effects of infection. Gene expression changes were more pronounced in the hindbrain and varied across developmental timepoints, while cortical changes were more limited. Immunostaining of neural populations, including radial glia, intermediate progenitors, and neurons, demonstrated broadly similar patterns between groups, with only modest differences. These findings suggest subtle disruption of coordinated developmental programs that may not be fully captured at single timepoints.

Although this system demonstrated substantial brain atrophy and developmental injury, ventriculomegaly was not observed. This differs from severe human infection and may reflect species-specific differences in ventricular or choroid plexus biology, or technical factors related to tissue processing.[73] Even so, the absence of ventriculomegaly does not diminish the broader relevance of the model, which captures multiple other hallmark features of prenatal Zika-associated brain injury.

Postnatally, infected mice exhibited reduced survival, decreased body weight, and mild developmental delays, as in humans.[45–47,50–52] Notably, early mortality disproportionately affected the most severely impacted animals, as evidenced by attenuation of neurological deficits when analyses were restricted to survivors. This suggests that postnatal assessments may underestimate the full severity of prenatal injury due to survivorship bias. Behavioral phenotypes in surviving animals were generally subtle, with some trends in exploratory and social behaviors, but limited statistical significance, likely reflecting both biological variability and selective survival. Due to sex-specific differences in postnatal survival, behavioral analyses were performed predominantly in female mice, which may have further influenced these results.

We also identified potential modifiers of disease severity. Female mice demonstrated improved postnatal survival compared to males, suggesting sex-specific susceptibility, as has been reported for other outcomes of infection.[58] Advanced maternal age was also associated with more severe outcomes at higher viral doses, although this observation requires further validation. This finding is consistent with broader evidence that advanced maternal and paternal age contribute to adverse pregnancy outcomes.[59,74,75] Together, these highlight the importance of host and environmental factors in shaping disease trajectory.

Several limitations should be considered. Species-specific differences between mouse and human placentation and immune responses may influence viral dynamics and outcomes. Despite these limitations, the use of a humanized, immunocompetent system represents a significant advance over existing models.

In summary, this model provides a translationally relevant platform for studying the mechanisms of prenatal viral brain injury and for evaluating potential therapeutic strategies. By capturing both the severity and variability of outcomes observed in humans, this system offers a valuable tool for understanding pathogenesis and identifying targets for intervention.

1.6 Supplemental Figures

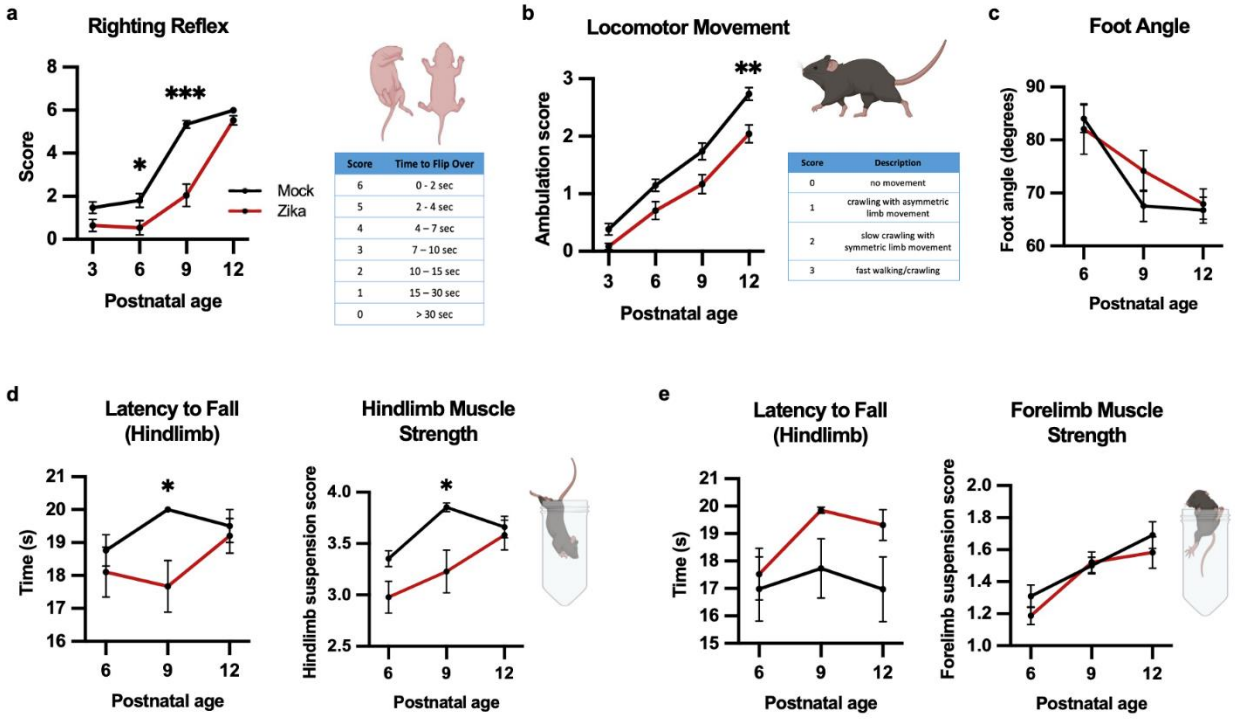

Fig. S1. Postnatal deaths did not affect developmental data. (a-e) Data from Figure 6, only including mice that survived the duration of motor milestone testing (n (litters, embryos) = (2, 12 mock), (4, 12 Zika)). Developmental testing included righting reflex **(a)**, locomotor movement **(b)**, foot angle while walking **(c)**, hindlimb suspension **(d)**, and forelimb suspension **(e)**. For at

least one timepoint, infected mice demonstrated delay in righting reflex, locomotor movement, hindlimb suspension score, and hindlimb strength. There was no significance in foot angle, latency to fall (hindlimb and forelimb), or forelimb suspension score.

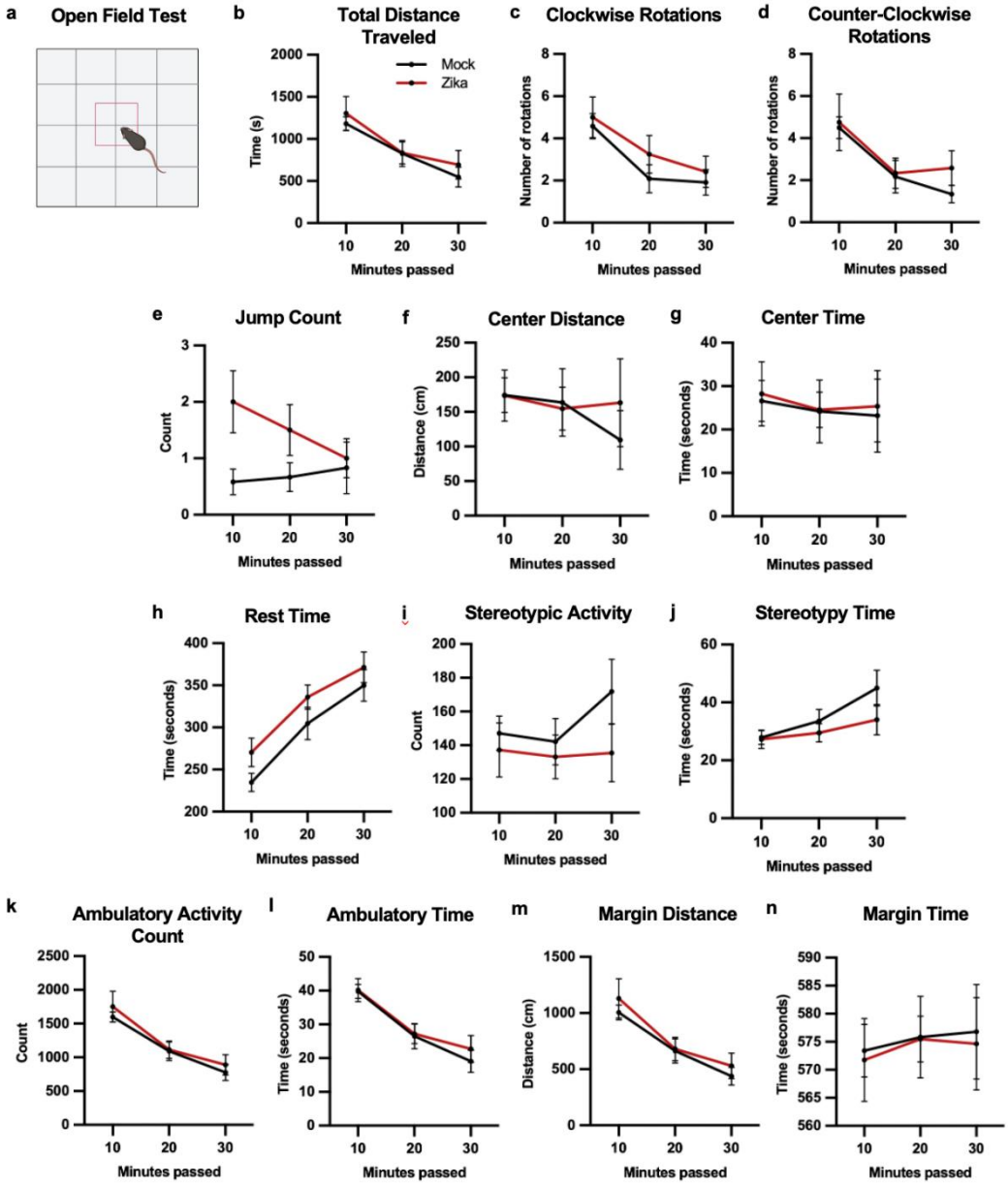

Fig. S2. Open field test for mock- and Zika-infected mice. (a-n) Various ambulatory measurements from mock- or Zika-infected mice in an open field test, which lasted for 30 mins (n (litters, embryos): (2, 12 mock), (2, 12 Zika). There was no significant difference between mock- or Zika-infected mice. We used (*) when $P < 0.05$; (**) when $P < 0.01$; and (***) when $P < 0.001$.

1.7 Supplemental Statistical Information

Fig. 1e: Data were analyzed with individual unpaired t-tests and are as follows: n (litters, embryos) = (2, 5 mock), (2, 4 Zika). Total area: $P = 0.0476$. Decidua: $P = 0.0317$. Junctional zone: $P = 0.2038$. Labyrinth: $P = 0.0588$. Chorionic plate: $P = 0.0094$.

Fig. 2a: Data were analyzed with a one-way ANOVA and Dunnett's test to correct for multiple comparisons and are as follows: DPBS: n (litters, embryos) = (3, 12). Viral titer in PFU: 7.78×10^7, 1.56×10^8, 2.33×10^8, 3.11×10^8, and 3.89×10^8. Virus: n = (2, 15); (2, 15); (3, 18); (3, 18); and (3, 18). ANOVA Summary: P value = 0.03, F = 2.723, DFn, DFd = 5, 82.

Fig. 2b: Data were analyzed by a Logrank (Mantel-Cox) test and a Gehan-Breslow-Wilcoxon test and are as follows: DPBS: n (litters, embryos) = (3, 10). Virus: n = (2, 14), (2, 15), (3, 18), (3, 18), and (3, 15). $P = 0.058$.

Fig. 2d-e: Data were analyzed with two-way ANOVAs with mixed effect method, corrected using Šídák's multiple comparisons test, and are as follows: Placenta Diameter: Timepoint of Infection: $P = 0.13$. F = 2.337. DFn, DFd = 1, 77. IC: $P = 0.004$. F = 8.768. DFn, DFd = 1, 77. Timepoint of Infection x IC: $P = 0.15$. F = 2.130. DFn, DFd = 1, 77. Mouse Area: Timepoint of Infection: $P = 0.01$. F = 6.736. DFn, DFd = 1, 76. IC: $P < 0.001$. F = 16.04. DFn, DFd = 1, 76. Timepoint of Infection x IC: $P = 0.53$. F = 0.4053. DFn, DFd = 1, 76. Crown-Rump: Timepoint of Infection: $P = 0.01$. F = 7.051. DFn, DFd = 1, 75. IC: $P < 0.001$. F = 18.70. DFn, DFd = 1, 75. Timepoint of Infection x IC: $P = 0.21$. F = 1.604. DFn, DFd = 1, 75. Brain Area: Timepoint of Infection: $P = 0.006$. F = 7.917. DFn, DFd = 1, 77. IC: $P = 0.06$. F = 3.573. DFn, DFd = 1, 77. Timepoint of Infection x IC: $P = 0.25$. F = 1.349. DFn, DFd = 1, 77. Brain Length: Timepoint of Infection: $P = 0.16$. F = 2.026. DFn, DFd = 1, 77. IC: $P = 0.78$. F = 0.08149. DFn, DFd = 1, 77. Timepoint of Infection x IC: $P = 0.07$. F = 3.441. DFn, DFd = 1, 77. Hindbrain Width: Timepoint of Infection: $P = 0.91$. F = 0.01159. DFn, DFd = 1, 77. IC: $P = 0.52$. F = 0.4263. DFn, DFd = 1, 77. Timepoint of Infection x IC: $P = 0.02$. F = 5.486. DFn, DFd = 1, 77. Medial-Lateral: Timepoint of Infection: $P = 0.03$. F = 4.714. DFn, DFd = 1, 77. IC: $P = 0.01$. F = 6.754. DFn, DFd = 1, 77. Timepoint of Infection x IC: $P = 0.49$. F = 0.4718. DFn, DFd = 1, 77. Fronto-Occipital: Timepoint of Infection: $P = 0.001$. F = 11.13. DFn, DFd = 1, 77. IC: $P < 0.001$. F = 12.49. DFn, DFd = 1, 77. Timepoint of Infection x IC: $P = 0.98$. F = 0.0007772. DFn, DFd = 1, 77.

Fig. 3d-f: Data were analyzed with Mann-Whitney tests and are as follows: Forebrain (Region 1): n (litters, embryos) = (2, 6 mock), (2, 9 Zika). Lateral Ventricle: P value = 0.8639. Germinal Zone: $P = 0.005$. Cortical Plate: $P = 0.066$. Hemisphere: $P = 0.026$. Anterior Midbrain (Region 2): n = (2, 5 mock), (2, 7 Zika). Lateral Ventricle: $P = 0.530$. Germinal Zone: $P = 0.01$. Cortical Plate: $P = 0.048$. Midbrain: $P = 0.03$. Hemisphere: $P = 0.03$. Posterior Midbrain (Region 3): n = (2, 6 mock), (1, 6 Zika). Lateral Ventricle: $P = 0.589$. Germinal Zone: $P = 0.937$. Cortical Plate: $P = 0.589$. Midbrain: $P = 0.818$. Hemisphere: $P = 0.485$.

Fig. 5: For all measurements in figure 5, n (litters, embryos) = P0: (2, 17 mock), (4, 21 Zika). P3: (2, 17 mock), (4, 16 Zika). P6: (2, 17 mock), (4, 14 Zika). P9: (2, 17 mock), (4, 13 Zika). P12: (2, 17 mock), (4, 12 Zika).

Fig. 5b: Data were analyzed with a log-rank (Mantel-Cox) test and are as follows: Chi square = 9.640, DF = 1, *P* value = 0.0019.

Fig. 5c: Data were analyzed with two-way ANOVAs with mixed effect method with a random coefficient, corrected using Šídák's multiple comparisons test, and are as follows: Fixed Effects: Time: $P < 0.0001$. F = 824.8. DFn, DFd = 1.555, 43.33. Infection Condition (IC): $P < 0.0001$. F = 17.47. DFn, DFd = 1, 36. Time x IC: $P < 0.0001$. F = 6.023. DFn, DFd = 7, 195.

Fig. 5d-h: Data were analyzed with two-way ANOVAs with mixed effect method and a random coefficient, corrected using Šídák's multiple comparisons test, and are as follows: Righting Reflex Fixed Effects Results: Time: $P < 0.0001$. F = 130.9. DFn, DFd = 2.532, 97.08. Infection Condition (IC): $P < 0.0001$. F = 60.27. DFn, DFd = 1, 115. Time x IC: $P < 0.0001$. F = 11.50. DFn, DFd = 3, 115. Locomotor Movement Fixed Effects Results: Time: $P < 0.0001$. F = 113.6. DFn, DFd = 2.547, 71.32. IC: $P < 0.0001$. F = 30.15. DFn, DFd = 1, 31. Time x IC: $P = 0.36$. F = 1.087. DFn, DFd = 3, 84. Foot Angle Fixed Effects Results: Time: $P < 0.0001$. F = 12.70. DFn, DFd = 1.939, 132.8. IC: $P = 0.47$. F = 0.5226. DFn, DFd = 1, 85. Time x IC: $P = 0.39$. F = 0.9368. DFn, DFd = 2, 137. Latency to Fall Hindlimb Fixed Effects Results: Time: $P = 0.1522$. F = 2.021. DFn, DFd = 1.623, 44.62. IC: $P = 0.0597$. F = 3.841. DFn, DFd = 1, 29. Time x IC: $P = 0.0703$. F = 2.788. DFn, DFd = 2, 55. Hindlimb Muscle Strength Fixed Effects Results: Time: $P = 0.0006$. F = 9.310. DFn, DFd = 1.773, 48.77. IC: P = 0.0034. F = 10.16. DFn, DFd = 1, 29. Time x IC: $P = 0.0350$. F = 3.567. DFn, DFd = 2, 55. Latency to Fall Forelimb Fixed Effects Results: Time: $P = 0.6363$. F = 0.4316. DFn, DFd = 1.849, 50.86. IC: $P = 0.3660$. F = 0.8434. DFn, DFd = 1, 29. Time x IC: $P = 0.6733$. F = 0.3984. DFn, DFd = 2, 55. Forelimb Muscle Strength Fixed Effects Results: Time: $P < 0.0001$. F = 19.28. DFn, DFd = 1.869, 51.40. IC: $P = 0.2197$. F = 1.573. DFn, DFd = 1, 29. Time x IC: $P = 0.6481$. F = 0.4371. DFn, DFd = 2, 55.

Fig. 6: For all measurements in figure 5, n (litters, embryos) = (2, 12 mock), (4, 12 Zika).

Fig. 6c: Data were analyzed with individual unpaired t-tests and are as follows: Time spent in each chamber: Novel object chamber: $P = 0.5909$. T ratio = 0.5455. Center chamber: $P = 0.05$. T = 2.115. Novel animal chamber: $P = 0.28$. T = 1.109. Entrances to each chamber: Novel object chamber: $P = 0.55$. T = 0.6045. Novel animal chamber: $P = 0.45$. T = 0.7717. Time spent with novelties: Novel object: $P = 0.73$. T = 0.3445. Novel animal: $P = 0.48$. T = 0.7212. Entrances to each chamber: Novel object chamber: $P = 0.5517$. T = 0.6045. Novel animal chamber: $P = 0.4485$. T = 0.7717. DF for all calculations was 22.00.

Fig. 6d: Data were analyzed with two-way ANOVAs with mixed effect method, corrected using Šídák's multiple comparisons test, and are as follows: Rotarod Fixed Effects

Results: Time: $P = 0.0003$. F = 8.458. DFn, DFd = 2.478, 54.52. Infection Condition (IC): $P = 0.0263$. F = 5.671. DFn, DFd = 1, 22. Time x IC: $P = 0.9158$. F = 0.1707. DFn, DFd = 3, 66.

Fig. 6e: Data were analyzed with individual unpaired t-tests and are as follows: Total steps: $P = 0.10$. T = 1.741. SAP: $P = 0.93$. T = 0.08647. AAR: $P = 0.09$. T = 1.759. SAR: $P = 0.08$. T = 1.808. DF for all calculations was 22.

Fig. 6f: Data were evaluated with individual unpaired t-tests and are as follows: Time spent in each arm: Open: $P = 0.35$. T = 0.9576. Closed: $P = 0.3486$. T = 0.9576. Entrances to each arm: Open arm: $P = 0.8975$. T = 0.1303. Closed arm: $P = 0.7161$. T = 0.3684. DF for all calculations was 22.

Fig. 6g: Data were analyzed with an unpaired t-test and are as follows: P value = 0.05. T value = 2.159, DF = 14.

Fig. 7a-b: Data were analyzed with two-way ANOVAs and are as follows: n (litters, embryos) = Males: (3, 14 mock), (3, 15 Zika). Females: (3,13 mock), (4, 14 Zika). Mouse Area Source of Variation: Sex: P value = 0.01. F = 6.433. DFn, DFd = 1, 46. Infection Condition (IC): $P < 0.001$. F = 13.90. DFn, DFd = 1, 46. Interaction: $P = 0.67$. F = 0.1788. DFn, DFd = 1, 46. Crown-Rump Source of Variation: Sex: $P = 0.05$. F = 3.954. DFn, DFd = 1, 45. IC: $P < 0.001$. F = 17.33. DFn, DFd = 1, 45. Interaction: $P = 0.22$. F = 1.548. DFn, DFd = 1, 45. Placenta Diameter Source of Variation: Sex: $P = 0.02$. F = 5.594. DFn, DFd = 1, 45. IC: $P < 0.001$. F = 14.42. DFn, DFd = 1, 45. Interaction: $P = 0.79$. F = 0.0688. DFn, DFd = 1, 45. Brain Area Source of Variation: Sex: $P < 0.001$. F = 18.52. DFn, DFd = 1, 45. IC: $P = 0.002$. F= 10.26. DFn, DFd = 1, 45. Interaction: $P = 0.84$. F = 0.0430. DFn, DFd = 1, 45. Medial-Lateral Source of Variation: Sex: $P = 0.12$. F = 2.501. DFn, DFd= 1, 47. IC: $P = 0.19$. F = 1.784. DFn, DFd = 1, 47. Interaction: $P = 0.14$. F = 2.311. DFn, DFd = 1, 47. Fronto-Occipital Source of Variation: Sex: $P = 0.13$. F = 2.344. DFn, DFd = 1, 46. IC: $P = 0.02$. F = 5.990. DFn, DFd = 1, 46. Interaction: $P = 0.58$. F = 0.3125. DFn, DFd = 1, 46. Brain Length Source of Variation: Sex: $P = 0.006$. F = 8.230. DFn, DFd = 1, 45. IC: $P = 0.01$. F = 7.085. DFn, DFd = 1, 45. Interaction: $P = 0.57$. F = 0.3352. DFn, DFd = 1, 45. Hindbrain Width Source of Variation: Sex: $P = 0.010$. F = 7.329. DFn, DFd = 1, 45. IC: $P = 0.01$. F = 6.744. DFn, DFd = 1, 45. Interaction: $P = 0.96$. F = 0.0031. DFn, DFd = 1, 45.

Fig. 7c: Data were analyzed with Fisher's Exact Test are as follows: n (litters, embryos): E15.5: (3, 27 mock), (4, 26 Zika). P21: (2, 17 mock), (2, 12 Zika). E15.5: $P = 0.5883$. P21: $P = 0.0216$. We used (*) when $P < 0.05$; (**) when $P < 0.01$; and (***) when $P < 0.001$.

Supplemental Fig. 1: Data were analyzed using two-way ANOVAs with mixed effect method and corrected with Šídák's multiple comparisons test (Righting Reflex Fixed Effects Results: Time: P value < 0.0001. F = 126. DFn, DFd = 2.587, 69.85. Condition: $P < 0.0001$. F = 51.84. DFn, DFd = 1, 27. Time x Condition: $P < 0.0001$. F = 9.917. DFn, DFd = 3, 81. Locomotor Movement Fixed Effects Results: Time: $P < 0.0001$. F = 105.6. DFn, DFd = 2.516, 67.93. Condition: $P < 0.0001$. F = 23.74. DFn, DFd = 1, 27. Time x Condition: $P = 0.4345$. F =

0.9210. DFn, DFd = 3, 81. Foot Angle Fixed Effects Results: Time: $P < 0.0001$. F = 12.70. DFn, DFd = 1.939, 132.8. Condition: $P = 0.47$. F = 0.5226. DFn, DFd = 1, 85. Time x Condition: $P = 0.39$. F = 0.9368. DFn, DFd = 2, 137. Latency to Fall Hindlimb Fixed Effects Results: Time: $P = 0.2034$. F = 1.643. DFn, DFd = 1.970, 53.19. Condition: $P = 0.0280$. F = 5.392. DFn, DFd = 1, 27. Time x Condition: $P = 0.1115$. F = 2.285. DFn, DFd = 2, 54. Hindlimb Muscle Strength Fixed Effects Results: Time: $P = 0.0007$. F = 8.545. DFn, DFd = 1.944, 52.48. Condition: $P = 0.0020$. F = 11.73. DFn, DFd = 1, 27. Time x Condition: P = 0.0773. F = 2.686. DFn, DFd = 1, 54. Latency to Fall Forelimb Fixed Effects Results: Time: P = 0.2477. F = 1.434. DFn, DFd = 1.882, 50.82. Condition: $P = 0.1168$. F = 2.625. DFn, DFd = 1, 27. Time x Condition: $P = 0.5629$. F = 0.5808. DFn, DFd = 2, 54. Forelimb Muscle Strength Fixed Effects Results: Time: $P < 0.0001$. F = 19.38. DFn, DFd = 1.802, 48.67. Condition: $P = 0.3593$. F = 0.8696. DFn, DFd = 1, 27. Time x Condition: $P = 0.4737$. F = 0.7577. DFn, DFd = 2, 54). Error bars represent standard error of the mean. Some error bars are not shown because standard error of the mean is smaller than the space covered by the data point.

Supplemental Fig. 2: Data were analyzed with two-way ANOVAs with mixed effect method, corrected using Šídák's multiple comparisons test, and are as follows: Total Distance Traveled Fixed Effects Results: Time: P value < 0.0001. F = 28.84. DFn, DFd = 1.551, 34.12. Infection Condition (IC): $P = 0.6278$. F = 0.2417. DFn, DFd = 1, 22. Time x IC: $P = 0.6729$. F = 0.3998. DFn, DFd = 2, 44. Clockwise Rotation Fixed Effects Results: Time: P value < 0.0001. F = 13.79. DFn, DFd = 1.723, 37.92. IC: $P = 0.4403$. F = 0.6176. DFn, DFd = 1, 22. Time x IC: $P = 0.7423$. F = 0.3. DFn, DFd = 2, 44. Counter-Clockwise Rotations Fixed Effects Results: Time: $P = 0.0005$. F = 12.09. DFn, DFd = 1.393, 30.64. IC: $P = 0.5585$. F = 0.3530. DFn, DFd = 1, 22. Time x IC: $P = 0.6021$. F = 0.5132. DFn, DFd = 2, 44. Jump Count Fixed Effects Results: Time: $P = 0.5117$. F = 0.6324. DFn, DFd = 1.696, 37.3. IC: $P = 0.0635$. F = 3.818. DFn, DFd = 1, 22. Time x IC: $P = 0.1853$. F = 1.752. DFn, DFd = 2, 44. Center Distance Fixed Effects Results: Time: $P = 0.3993$. F = 0.8807. DFn, DFd = 1.553, 34.16. IC: $P = 0.7787$. F = 0.08093. DFn, DFd = 1, 22. Time x IC: $P = 0.4933$. F = 0.7181. DFn, DFd = 2, 44. Center Time Fixed Effects Results: Time: $P = 0.6967$. F = 0.3427. DFn, DFd = 1.862, 40.97. IC: $P = 0.8687$. F = 0.02799. DFn, DFd = 1, 22. Time x IC: $P = 0.9769$. F = 0.02339. DFn, DFd = 2, 44. Rest Time Fixed Effects Results: Time: $P < 0.0001$. F = 44.87. DFn, DFd = 1.908, 41.97. IC: $P = 0.1466$. F = 2.265. DFn, DFd = 1, 22. Time x IC: $P = 0.8206$. F = 0.1986. DFn, DFd = 2, 44. Stereotypic Activity Count Fixed Effects Results: Time: $P = 0.4680$. F = 0.7640. DFn, DFd = 1.933, 42.52. IC: $P = 0.2283$. F = 1.536. DFn, DFd = 1, 22. Time x IC: $P = 0.5092$. F = 0.6853. DFn, DFd = 2, 44. Stereotypy Time Fixed Effects Results: Time: $P = 0.0128$. F = 5.162. DFn, DFd= 1.775, 39.04. IC: $P = 0.2217$. F = 1.581. DFn, DFd = 1, 22. Time x IC: $P = 0.3936$. F = 0.9524. DFn, DFd = 2, 44. Ambulatory Activity Count Fixed Effects Results: Time: $P < 0.0001$. F = 49.47. DFn, DFd = 1.452, 31.94. IC: $P = 0.6037$. F = 0.2774. DFn, DFd = 1, 22. Time x IC: $P = 0.7477$. F = 0.2927. DFn, DFd = 2, 44. Ambulatory Time Fixed Effects Results: Time: $P < 0.0001$. F = 36.71. DFn, DFd = 1.801, 39.62. IC: $P = 0.6778$. F = 0.1773. DFn, DFd = 1, 22. Time x IC: $P = 0.7322$. F = 0.3140. DFn, DFd = 2, 44. Margin Distance Fixed Effects Results:

Time: $P < 0.0001$. F = 42.39. DFn, DFd = 1.480, 32.56. IC: $P = 0.5944$. F = 0.2920. DFn, DFd = 1, 22. Time x IC: $P = 0.6942$. F = 0.3680. DFn, DFd = 2, 44. Margin Time Fixed Effects Results: Time: $P = 0.6965$. F = 0.3430. DFn, DFd = 1.862, 40.97. IC: $P = 0.8687$. F = 0.02798. DFn, DFd = 1, 22. Time x IC: $P = 0.9768$. F = 0.02345. DFn, DFd = 2, 44.

Chapter 2 - Using Precision Therapies to Protect the Developing Brain from Viral Infection and Injury

Authors: Gemstone Team Viral[1] (Clara Abdelmalek,[1, 2, 3] Ademide Adeyemo,[1, 2, 3] Aubrey Alexander,[1, 2, 3] Hannah Camacho,[1, 2, 3] Zofia Dyba,[1, 2, 3] Caroline Hobson,[1, 2, 3] Haider Hussain,[1, 2, 3] Erin Li,[1, 2, 3] Soumya Maturi,[1, 2, 3] Arnav Patel,[1, 2, 3] Nandi Patel,[1, 2, 3] Ashley Pocasangre,[1, 2, 3] and Janet Ruan[1, 2, 3]), Eunbin Park,[2, 3] Erin Tran,[1, 4] Youssef A. Kousa[1, 3, 5-8]*

Affiliations:
[1]Gemstone Honors Program, University of Maryland; College Park, MD.
[2]Center for Precision Medicine and Genomics Research and [3]Center for Neuroscience Research, Children's National Research Institute; Washington, DC, 20012.
[4]Department of Cell Biology & Molecular Genetics, University of Maryland; College Park, MD.
[5]Division of Neurology, and [6]Division of Neurophysiology, Epilepsy, and Critical Care, Children's National Hospital; Washington, DC, 20010.
[7]Departments of Pediatrics, and [8]Neurology, The George Washington University School of Medicine and Health Sciences; Washington, DC, 20010.
*Corresponding author. Youssef A. Kousa, MS, DO, PhD, Center for Genetic Medicine, Children's National Research and Innovation Campus, 7144 13th Pl NW, Suite 1247, Washington, DC 20012. Phone: (201) 774-7794. Email: YKousa@ChildrensNational.org.

2.1 Abstract

Prenatal viral infections can cause severe damage to the developing brain. Among the most threatening prenatal pathogens, the Zika virus (**ZIKV**) can cause microcephaly, congenital contractures, seizures, and fetal demise. Currently, there is no prenatal standard of care or treatment for ZIKV infection. Whole exome sequencing of severely affected patients identified mTOR (a regulator of autophagy) and HEXB (a lysosomal enzyme) as modifiers of injury, suggesting that the autophagy–lysosomal pathway represents a promising therapeutic target. In this work, we repurpose and test three drugs that modulate distinct components of the autophagy–lysosomal pathway. The drugs tested include chloroquine, a lysosomal inhibitor; metformin, an AMPK signal inducer; and trehalose, a lysosomal flux activator. By targeting multiple regulatory points within this pathway, we aim to determine whether coordinated manipulation of autophagic and lysosomal activity can alter the course of prenatal ZIKV

infection. Here, we tested three prenatal ZIKV treatments in infected, immunocompetent, and virally susceptible (hSTAT2KI/KI) mice at a developmental stage analogous to the late first trimester in humans. Mock and ZIKV-infected mice with drug or mock treatment were monitored for survival, weight progression, and neurodevelopmental outcomes through postnatal developmental testing. Preliminary data show that metformin may increase postnatal survival. At the doses under investigation, chloroquine and trehalose appear safe but do not significantly improve survival. In future work, we will optimize dosing for compounds that demonstrate efficacy and further evaluate treatment safety. This therapeutic strategy may also be translatable to other prenatally transmitted viruses, including cytomegalovirus and oropouche.

2.2 Introduction

2.2.1 Background on Prenatal Viral Infections

Prenatal viral infections occur when certain pathogens cross the placental barrier and infect the developing fetus, posing significant risks to neurodevelopmental outcomes. Common congenital viruses include ZIKV, Cytomegalovirus (**CMV**), Parvovirus B19, Varicella Zoster, and Herpes Simplex Virus (**HSV**).[76] Infection can result in severe outcomes such as microcephaly, seizures, preterm birth, and spontaneous abortion.[77–79]

Among these, ZIKV is particularly destructive due to its ability to infect neural cells and cross both the placental and blood–brain barriers. ZIKV leads to widespread neurodevelopmental injury and often manifests as congenital Zika syndrome (**CZS**), characterized by microcephaly, cortical thinning, ocular defects, and, in severe cases, fetal or neonatal demise[69,76–78]. These consequences distinguish ZIKV from other congenital viruses and highlight the urgent need for effective prenatal interventions.

2.2.2 Gaps in Treatment

ZIKV transmission disproportionately affects tropical and subtropical regions, where the primary mosquito vector, *Aedes aegypti,* thrives. Endemic regions like Central and South America, the Caribbean, and parts of Southeast Asia experience year-round warm temperatures, high rainfall, and dense urban environments that promote rapid mosquito breeding and viral transmission. Limited infrastructure for vector control, such as inconsistent waste management and inadequate access to piped water, further increases exposure risk, particularly in low-income communities.[10,78,79]

These same regions often face barriers to healthcare access, which intensify the impact of prenatal ZIKV infection. For example, pregnant individuals who must travel long distances to reach prenatal care facilities arrive at clinics that lack routine ultrasound imaging, laboratory diagnostics, or specialists trained in congenital infection management.[80] Economic constraints, shortages of healthcare personnel, and fragmented public health systems further hinder early

diagnosis and monitoring. Families caring for infants with CZS report major obstacles in obtaining rehabilitation, specialist follow-up, and essential support services, contributing to long-term disparities in developmental outcomes.[81]

The convergence of environmental risk, vector ecology, and limited healthcare infrastructure means that pregnant individuals in low-resource tropical regions bear the highest burden of ZIKV-related complications. As a result, any effective therapy for prenatal ZIKV infection must be not only biologically effective but also affordable, stable without cold-chain requirements, and easily distributed in resource-limited settings. Treatments fitting this profile, such as orally administered, low-cost drugs, have the most significant potential for real-world implementation and global health impact.

ZIKV is also capable of crossing the placenta and persisting in fetal tissue, complicating treatment, and creating a narrow therapeutic window. Furthermore, many conventional antiviral agents also carry teratogenic risks.[80,81] Immunoglobulin therapies and vaccine candidates have shown promise in preclinical studies. Hyperimmune globulin and engineered antibody mixes reduce maternal viral load and fetal infection.[82] However, these approaches are costly, require cold-chain storage, and have limited efficacy across viral strains, limiting their feasibility in low-resource settings where ZIKV is most prevalent.

2.2.3 Hypothesis and Research Question

During our time in the University of Maryland Gemstone Honors Program, we investigated novel therapeutic strategies for prenatal ZIKV infection with the goal of preventing adverse outcomes in infants who experienced prenatal or fetal exposure to the virus. This study tests the hypothesis that modulating the autophagy–lysosomal pathway can alter the course of prenatal ZIKV infection and reduce virus-induced brain injury. Specifically, team VIRAL asks: Can manipulation of autophagy and lysosomal activity improve fetal and postnatal outcomes following prenatal ZIKV exposure?

Lysosomes play a central role in viral degradation by supporting autophagy, a cellular pathway that can help regulate infection and viral replication. Activating this pathway may enhance lysosomal recycling, reduce viral replication, and protect fetal brain development.[83] Conversely, some evidence suggests that viruses can hijack autophagy to enhance replication and evade immune responses, indicating that autophagy inhibition could also limit ZIKV replication.[84–89] Therefore, our work hopes to clarify and characterize the effect that autophagy, along with lysosomal activators or inhibitors, have on ZIKV disease progression in mice. These strategies may also be applied to other prenatal viral infections with similar mechanisms and clinical outcomes, expanding their potential impact on maternal-fetal health.

2.2.4 Objectives

We aim to identify safe and effective compounds that reduce fetal brain injury, improve postnatal outcomes, and are feasible for implementation in global health settings. To this end, we evaluated three drugs (chloroquine, metformin, and trehalose), chosen for their safety in pregnancy and their ability to modulate the autophagy–lysosomal pathway.[90–96]

2.3 Literature Review

2.3.1 ZIKV Biology

ZIKV is a single-stranded, positive-sense RNA virus in the *Flaviviridae* family, which includes human pathogens such as dengue virus (**DENV**), West Nile virus (**WNV**), and Japanese encephalitis virus (**JEV**). Its ~10.8 kb genome encodes a single polyprotein, which is processed into three structural proteins (capsid, pre-membrane, and envelope) and seven non-structural proteins (NS1–NS5) that regulate viral replication and function.[90–92] The envelope protein mediates host cell entry via membrane fusion and shares over 50% amino acid sequence similarity with DENV envelope protein, contributing to structural and functional conservation across flaviviruses.

ZIKV spreads efficiently through a cell-to-cell mechanism, particularly in neural progenitor cells, where surface antigens remain largely hidden from the extracellular space.[93] Viral attachment is mediated by interactions between the envelope protein and negatively charged glycosaminoglycans, including Dermatan Sulfate (**DS**) and chondroitin sulfate A (**CSA**), on host cell membranes (these form salt bridges with positively charged residues on the viral envelope).[94]

Following maternal infection, ZIKV initially infects keratinocytes and Langerhans cells and spreads to dendritic cells before reaching lymphoid organs. The virus can then infect placental cells, inducing apoptosis and weakening the placental barrier, while also targeting macrophages, endothelial cells, and Hofbauer cells to reach fetal circulation. ZIKV crosses the blood-brain barrier (**BBB**) by degrading tight junction proteins such as ZO-1 and occludin via transcytosis.[2,99] Once in the fetal brain, ZIKV infects neural stem cells (**NSCs**), triggering apoptosis and impairing self-renewal. This disrupts NSC proliferation and differentiation. Bhagat et al. suggest that this could contribute to the neurological deficits observed in congenital infection.[90,95]

Prenatal ZIKV infection severely impacts fetal and infant development, resulting in CZS.[96] CZS is commonly characterized by microcephaly, cortical thinning with subcortical calcifications, agyria or lissencephaly, seizures, developmental delay, intrauterine growth restriction, and auditory and visual deficits.[95,97,98] Microcephaly and cortical thinning are particularly notable due to their long-term consequences for language and cognitive development.[97] Epidemiological

studies indicate that roughly two-thirds of CZS infants present with severe microcephaly, and nearly all of these individuals experience severe-to-profound intellectual disability.[99]

Not all infants exposed to ZIKV in utero show abnormalities at birth, but some develop neurodevelopmental and behavioral impairments over time. This delayed onset is hypothesized to result from postnatal ZIKV replication in the brain, contributing to continued deceleration of brain growth.[51,52,81,100]

2.3.2 ZIKV Antagonism of STAT2

ZIKV evades the host immune response by targeting the *STAT2* signaling pathway, a critical mediator of type I interferon responses. The viral non-structural protein NS5 binds to and promotes degradation of human *STAT2*, preventing activation of antiviral genes and facilitating viral replication.[19] This antagonism is species-specific, as murine *STAT2* is not efficiently targeted by ZIKV, limiting viral replication and immune evasion in standard mouse models. Thus, effective mouse models require humanized *STAT2* (***hSTAT2***) in order to mimic the human-specific immune evasion of ZIKV.[35,101]

2.3.3 Autophagy–Lysosomal Pathway in ZIKV Infection

Autophagy is a process that helps maintain homeostasis by breaking down and recycling damaged cell parts, protein clumps, and invading pathogens.[55] During autophagy, the cell forms a double-membrane bubble called an autophagosome, which collects material for degradation. The autophagosome then fuses with a lysosome that digests the cargo. Once broken down, the pieces are reused by the cell for energy or rebuilding. Autophagy activation depends on the signals inside the cell. The mechanistic target of rapamycin (mTOR) regulates autophagy and cellular metabolism, and its activity influences viral replication and neuronal development. When nutrients are available, the protein complex mTORC1 remains active and prevents autophagy. When the cell is stressed—such as during infection—mTORC1 activity drops and autophagy begins.[102] Lysosomes play a key role in this process because they are the endpoint at which degradation happens (**Fig. 1**).

Autophagy plays a complicated role during viral infections. Sometimes it protects the host by delivering viruses to the lysosome for breakdown. In other cases, viruses take advantage of autophagy for their own benefit. ZIKV is one of the viruses that can hijack this pathway. In human fetal neural stem cells, ZIKV uses two of its proteins (NS4A and NS4B) to block the Akt–mTOR pathway, thereby inducing autophagy. This change helps ZIKV replicate, but it also impairs brain development by interfering with normal growth of neural cells. In the placenta, ZIKV also increases autophagy, and studies in pregnant mice show that blocking autophagy can reduce how much virus reaches the fetus and can prevent some forms of fetal injury. This suggests that, in early pregnancy, ZIKV may rely on autophagy to support its spread.

However, autophagy is not always harmful during ZIKV infection. Some research shows that certain forms of autophagy can limit viral replication, especially in brain tissue. Other studies indicate that ZIKV may use modified autophagy-like pathways, such as secretory autophagy, to cross the placenta and move into fetal circulation. This suggests that the effects of autophagy depend on the tissue type and stage of infection.

Lysosomes themselves are also important in controlling ZIKV. Transient receptor potential mucolipin proteins (**TRPMLs**) localize to the membranes of lysosomes and when lysosomes are activated—for example, by opening TRPML ion channels—the lysosome becomes more acidic and active. This increased activity has been shown to reduce ZIKV replication in cell studies by helping the breakdown of viral proteins more efficiently.

Modulating lysosomal activity can influence cellular defense against pathogens, including ZIKV. One potential approach is to alter the expression of genes that regulate autophagic activity, which may in turn affect ZIKV pathogenesis during pregnancy.[84] Studies on the role of autophagy in ZIKV infection have been contradictory, and it remains unclear whether viral replication can be inhibited by lysosomal activation, inhibition, or both at different stages of infection.[103]

Basal autophagy maintains cellular homeostasis and supports essential processes such as embryonic development, organogenesis, and immune regulation.[84] Impaired autophagy disrupts these processes. During ZIKV infection, autophagy influences viral transmission across the placenta and blood-brain barrier. Enhanced autophagy in early embryonic development can promote viral replication and facilitate maternal-to-fetal transmission.[104]

ZIKV induces macroautophagy in NSCs, enhancing viral replication, while simultaneously suppressing selective autophagy by inhibiting FANCC, a key antiviral factor, allowing the virus to evade host defenses and deplete NSCs.[105] The virus exploits autophagosome formation as a replication platform while manipulating autophagic flux to avoid degradation.[102]

Genetic factors can modulate susceptibility to infection. For example, loss of the autophagy gene Atg16l1 in mice was associated with lower ZIKV titers compared with wild-type controls, suggesting that gene suppression or enhancement can influence autophagic efficacy during infection.[84] The mTOR pathway also plays a complex role in viral replication across flaviviruses. Unlike some viruses that activate mTOR to increase protein synthesis, ZIKV inhibits mTOR activity, enhancing autophagy while disrupting viral protein synthesis.[106] In addition, whole genome sequencing of discordant dizygotic twins revealed a mutation in the 5'-UTR region of *MTOR*, suggesting a role in differential susceptibility to congenital ZIKV infection.

Together, these findings show that autophagy and lysosomal activity can either help or hurt the host during ZIKV infection. Because ZIKV depends on these pathways across multiple tissues,

modulating autophagy and lysosomal function with targeted therapies may help protect the fetus. The three agents in our study (chloroquine, metformin, and trehalose) each affect autophagy or lysosomal activity in different ways, allowing us to test whether increasing or decreasing these pathways can change the outcome of prenatal ZIKV infection.

2.3.4 HEXB and Genetic Susceptibility

Genetic factors can significantly influence host susceptibility to ZIKV infection and the severity of its effects on fetal development. Variants in genes involved in the autophagy–lysosomal pathway, including *HEXB* and *mTOR*, may alter autophagic flux and impact viral replication. *HEXB* encodes the lysosomal enzyme beta-hexosaminidase B, which degrades sphingolipids, oligosaccharides, and gangliosides. Loss-of-function mutations in *HEXB* can cause accumulation of GM2 gangliosides and neuronal loss, leading to lysosomal storage disorders such as Tay-Sachs and Sandhoff disease.[107] Preliminary data from the Kousa lab group (**K-Labs**) suggest that *HEXB* deficiency may also increase susceptibility to prenatal ZIKV infection by impairing lysosomal degradation of viral components.[101]

ZIKV infection has been shown to inhibit mTOR, enhancing autophagy but disrupting viral protein synthesis, highlighting the complex interplay between viral infection and host autophagic regulation.[103] Genetic variation in mTOR may therefore contribute to differences in fetal vulnerability to ZIKV, as evidenced by mutations identified in discordant dizygotic twins exposed to prenatal infection. Together, HEXB and mTOR illustrate how host genetics intersect with autophagic pathways to modulate susceptibility to congenital ZIKV infection.

2.3.5 Therapeutic Rationale

Modulating the autophagy–lysosomal pathway represents a promising approach to mitigating prenatal ZIKV infection, as this pathway plays a central role in both viral replication and neuronal protection. Targeting autophagy and lysosomal function may reduce viral load, limit fetal brain injury, and improve postnatal outcomes.

Several compounds have shown potential through distinct mechanisms. Chloroquine inhibits autophagy and viral replication by impairing the fusion of the lysosome and autophagosome.[108,109] Chloroquine has previously demonstrated protective effects against ZIKV in mouse models, effectively preventing maternal-to-fetal transmission.[89] Metformin inhibits mTORC1 through low-grade activity through AMPK-dependent mechanisms, as well as AMPK-independent pathways, in turn promoting the elongation of the autophagosome and transcription of lysosomal enzymes.[110–113] Trehalose, at clinically relevant doses, causes low-grade lysosomal stress. This inhibits mTORC1, and thus promotes autophagosome elongation, and activates TFEB, which facilitates autophagosome and lysosome biogenesis.[114–118]

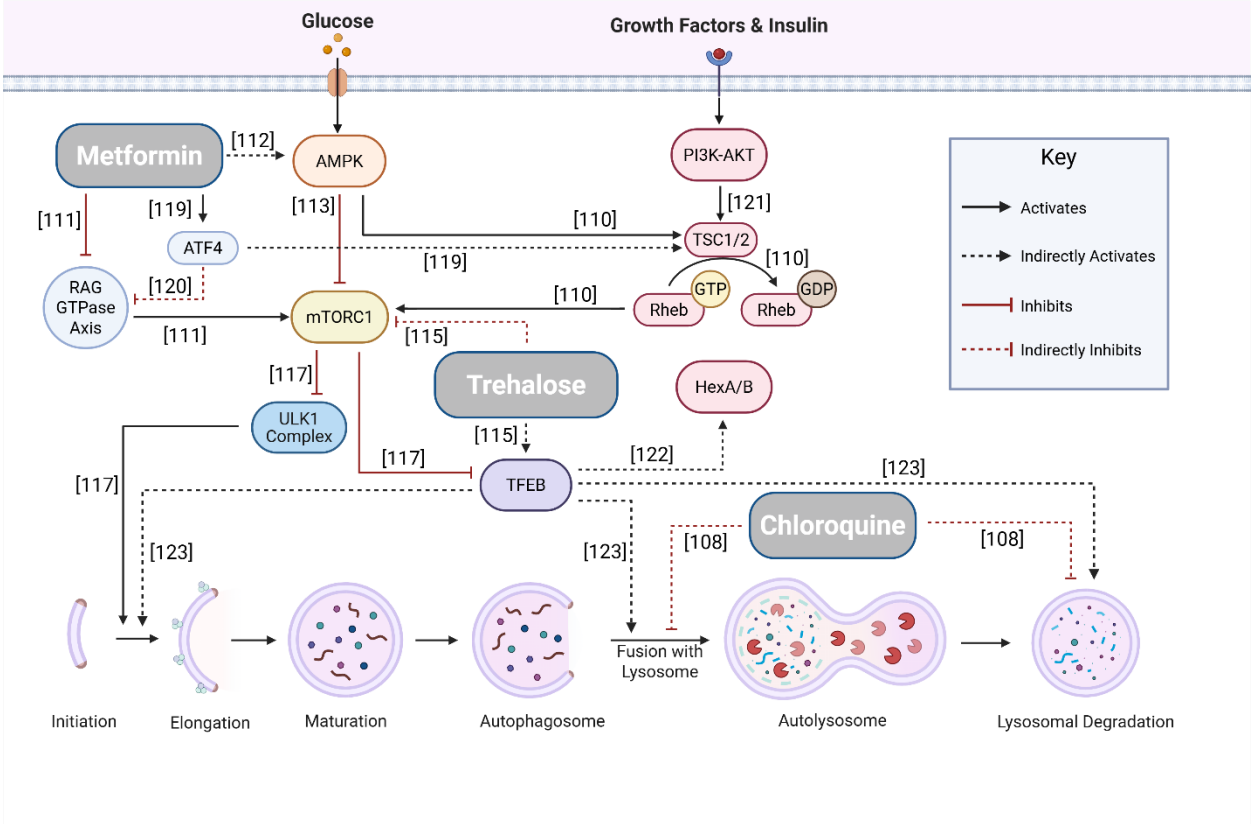

Fig. 1. The autolysosomal pathway: our experimental approach. This diagram shows the major steps of the autophagy–lysosomal pathway. Metformin inhibits mTORC1 and activates AMPK to increase autophagy and lysosomal gene expression. Trehalose enhances lysosomal activity and autophagic flux. Chloroquine raises lysosomal pH and blocks autophagosome–lysosome fusion.[108,110–113,115,117,119–123]

Together, these findings suggest that manipulating the autophagy–lysosomal pathway through distinct pharmacologic mechanisms may provide an effective strategy to protect the developing brain from ZIKV-induced injury. Further, targeting autophagy leverages a host-dependent pathway that the virus cannot easily bypass, offering protection not only against ZIKV but also against other neurotropic viruses that use similar mechanisms. As autophagy intersects with neurodevelopmental processes, moderating its activity may reduce viral injury while preserving its neuroprotective functions.[124] This rationale underlies our investigation of three therapeutics (chloroquine, metformin, trehalose), all of which act on the autophagy–lysosomal pathway (**Fig. 1**).

2.4 Methods

2.4.1 Vero Cell Culture

Vero cells were obtained from American Type Culture Collection (ATCC). Cells are cultured in standard DMEM/F-12 + Glutamax (Gibco) media supplemented with 2.5% fetal bovine serum. Cells were regularly passaged every 2-4 days based on confluency with 0.25% Trypsin-EDTA (Gibco).

2.4.2 Neural Stem Cell Culture

Human induced pluripotent stem cells (**iPSCs**) were cultured in standard media for multiple passages before induction into NSCs. Once healthy iPSCs were established for induction, cells were induced into NSCs with Neurobasal Media (Gibco) supplemented with 2% Neural Induction Supplement (StemPro). Full neural induction was incubated for seven days before expansion into neural stem cells with increasing gradient of NSC and neural induction media over time. Preliminary neural stem cells were expanded for four to six days before standard NSC splitting protocol was performed. The iPSC media was formulated with mTeSR media (Stemcell) and passaged with DPBS (-/-) (Gibco), 1% EDTA (Gibco), and 0.1 g NaCl. The neural stem cell growth media was formulated with DMEM/F-12 Knockout media (Gibco), 2% Neural Supplement (StemPro), 1% Antibiotic-Antimycotic (Gibco), 1% GlutaMax (Gibco), 80 ng/mL EGF, 80 ng/mL FGF. All passaging and assay plating for iPSCs, neural were prepared with 1X Geltrex LDEV-free Reduced-Growth Factor Basement-Membrane Matrix (Gibco) coating in DMEM/F-12 Knockout media (Gibco).

2.4.3 Metformin Efficacy

Preliminary in vitro cell viability studies were performed to test the efficacy of metformin in improving cell viability of both Vero cells and NSCs. For both assays, cell viability was indirectly measured with Cell Titer Glo Luminescent assays. Cells were incubated in the treatment for three days before adding Cell Titer Glo 2D Luminescence (Promega) reagent for luminescence detection. For all experiments, luminescence was further analyzed as a ratio of the experimental group to the mock-infected, mock-treated, negative control cells and converted into percentages.

2.4.4 Determination of Metformin Efficacy in Vero

In 96-well whitewall plates (Greiner), cells were seeded at $1x10^4$ cells/well and incubated at 37°C overnight. Cells were inoculated with ZIKV (MOI 1) or mock infection (standard Vero media) and incubated for 2 hours for viral attachment and entry. After incubation, the viral inoculum was removed, and both infected and mock-infected cells were treated with 100 µL of metformin treatment with variable ranges of doses. (i.e. 0 metformin, 10 mM, 20 mM, 30 mM, 40 mM, and 50 mM) diluted in standard Vero culture media. Cells were subsequently incubated in the treatment for three days before adding Cell Titer Glo 2D Luminescence (Promega) reagent for luminescence detection. Parallel experiments were run to collect supernatant after 72 hours of incubation. Plaque assays were performed on the collected supernatant to quantify viral progeny produced.

2.4.5 Determination of Metformin Efficacy in NSCs

In Geltrex-coated 96-well whitewall plates (Greiner), cells were seeded at $2x10^4$ cells/well and incubated at 37°C overnight. Cells were washed once with DMEM/F-12 Knockout media before inoculating with ZIKV (MOI 3) or mock infection (standard NSC media) and incubating for 3 hours for viral attachment and entry. After incubation, the viral inoculum was removed and cells were washed three times with DMEM/F-12 Knockout media. Both infected and mock-infected cells were treated with 200 µL of metformin (i.e. 0 metformin, 0.01 µM, 0.1 µM, 1 µM, 10 µM, 100 µM, 10,000 µM) diluted in NSC standard culture media. Cells were subsequently incubated in the treatment for three days before adding Cell Titer Glo 2D Luminescence (Promega) reagent for luminescence detection. Parallel experiments were run to collect supernatant after 72 hours of incubation. Plaque assays were performed on the collected supernatant to quantify viral progeny produced.

2.4.6 Quantification of Viral Titer

Standard plaque assay protocols were used to quantify viral titer of the viral supernatant 72 hours after metformin treatment. In Geltrex-coated 24-well plates (ThermoFisher), cells were seeded at $8x10^4$ cells/well and incubated at 37°C overnight. Collected supernatant was serially diluted ten-fold and tested in concentrations of 10^{-1}, 10^{-2}, 10^{-3}, 10^{-4}, 10^{-5}, and 10^{-6} with DMEM/F-12 Knockout media. Cells were inoculated with serially diluted viral supernatants and incubated for 1 hour. After 1 hour incubation, 10% methylcellulose overlay was added to inoculated cells. Plaque assays were incubated for 5 days. On day 5 of the incubation, methylcellulose overlay and viral infection were removed and washed three times with DPBS (Gibco). Cells were stained with 4% paraformaldehyde for 25 minutes at room temperature. Paraformaldehyde was then washed three times with DPBS and stained with 1% cresyl violet stain. Plaques were counted by eye and calculated as titers of PFU/mL.

2.4.7 Model System and IACUC Protocol

Refer to Horvath et al. (Chapter 1) for details about the model system including hSTAT2KI/KI colony generation, ZIKV strain, ZIKV preparation, and ZIKV infection procedure. Prior to the initiation of experiments, an Institutional Animal Care and Use Committee (**IACUC**) protocol was submitted to the Children's National IACUC for review and approval. The protocol detailed the proposed mouse model, justification for the use of an animal model, breeding procedures, experimental methods, pharmacological agents to be administered, anticipated sources of animal distress, and strategies to minimize discomfort. Following committee review, revisions were made in response to reviewer feedback. Upon approval, all experiments were conducted in accordance with the approved protocol and institutional guidelines for animal welfare and safety.

2.4.8 Experimental Design

We assessed how each treatment influenced survival outcomes in ZIKV-infected pups under prenatal conditions (**Fig. 2**). Pregnant dams were infected with $7.78x10^7$ PFU of ZIKV-Dak-MA or DPBS at embryonic day 9.5 (E9.5) via intraperitoneal (IP) injection. Due to limited viral stock, two distinct batches of ZIKV-Dak-MA with different titers were used. Viral amplification and titer quantification were performed as described in Chapter 1. Batch 1 had a titer of $6.75x10^8$ PFU/mL, and batch 2 had a titer of $6.8x10^9$ PFU/mL. A total injection volume of 120 µL was used for all conditions, with DPBS dilution applied as needed to achieve the appropriate viral dose, particularly for batch 2. Data were collected at the postnatal timepoint, with pups harvested after birth.

We determined which treatments increase the survival rate of ZIKV-infected pups by quantifying postnatal survival across treatment groups relative to mock-treated controls. Following infection with $7.78x10^7$ PFU ZIKV at E9.5, each pregnant mouse received either DPBS (mock treatment) or the highest recommended dose of chloroquine, metformin, or trehalose, beginning 4 hours post-infection (**hpi**). Treatments were given daily from E9.5 until E18.5. The specific treatment doses based on prior studies are as follows: chloroquine: 50 mg/kg/day[125]; metformin: 100 mg/kg/day; trehalose: 3,333 mg/kg/day[126]. Pregnant mice were weighed to calculate drug doses, which were dissolved in an equal volume of DPBS. Postnatally, we assessed the percentage of pup survival and recorded pup weights at P3, P6, P9, P12, P15, P18, and P21, the time at which pups were weaned from their mother. Additionally, developmental testing was performed at P3, P6, P9, and P12. The treatment(s) that successfully increased the survival of the pups were used in subsequent experiments.

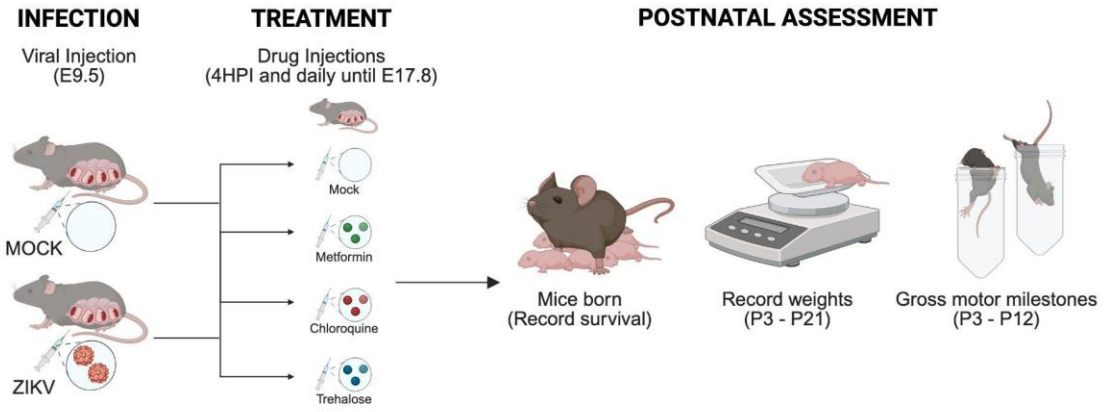

Fig. 2. Experimental workflow for drug treatment in a prenatal ZIKV mouse model. Pregnant dams were either mock- or ZIKV-infected at E9.5. Four hpi and daily until E17.8, pregnant dams received a mock treatment or drug treatment with either metformin, chloroquine, or trehalose. After birth, pup survival was recorded. Postnatal development was assessed by

measuring the pup body weight from P3 to P21 every 3 days and evaluating gross motor milestones from P3 to P12. Postnatal outcomes were compared across treatment groups.

2.4.9 Metformin Dose Optimization

We evaluated the optimal dosing range for metformin following its initial identification as the most effective treatment for improving survival. Using the same infection and treatment timeline, doses were systematically varied to assess a dose-dependent response. ZIKV-infected pregnant mice were administered an initial dose of 100 mg/kg/day, which was selected based on reported in vivo dosing ranges for metformin and used as the lower bound for titration. The dose was subsequently increased to 200 mg/kg/day to evaluate survival outcomes at higher exposure levels. Postnatal survival and development were assessed.

2.4.10 Chloroquine Treatment Safety

Following ZIKV infection and chloroquine treatment, decreased pup survival rates suggested treatment-associated toxicity. To isolate the effects of chloroquine, additional pregnant dams were mock-infected and treated with chloroquine at the same timepoint.

2.4.11 Postnatal Assessment

Gross Motor Assessments and Survival. Refer to Horvath et al. (Chapter 1) for details about postnatal assessment for survival to P21 and gross motor milestone testing including righting reflex, locomotor movement, hindlimb foot angle, hindlimb strength, and forelimb strength.

Litter Size. Litter size for each pregnant dam was recorded on P0. For dams that successfully gained weight during pregnancy but gave birth to no pups after rapid weight loss, litter size was estimated using a standard pup weight.

2.5 Results

2.5.1 Metformin

We evaluated the effects of metformin in both cell culture and mouse models. In Vero cell culture, cells were infected with ZIKV at MOI 1 for 2 hours and subsequently treated with variable metformin doses (0-50 mM) for 72 hours. Following a 72-hour treatment period, ZIKV-infected cells that were mock-treated with regular culture media had a cell viability of 8 percent compared to mock-treated, mock-infected Vero cells (**Fig. 3**).

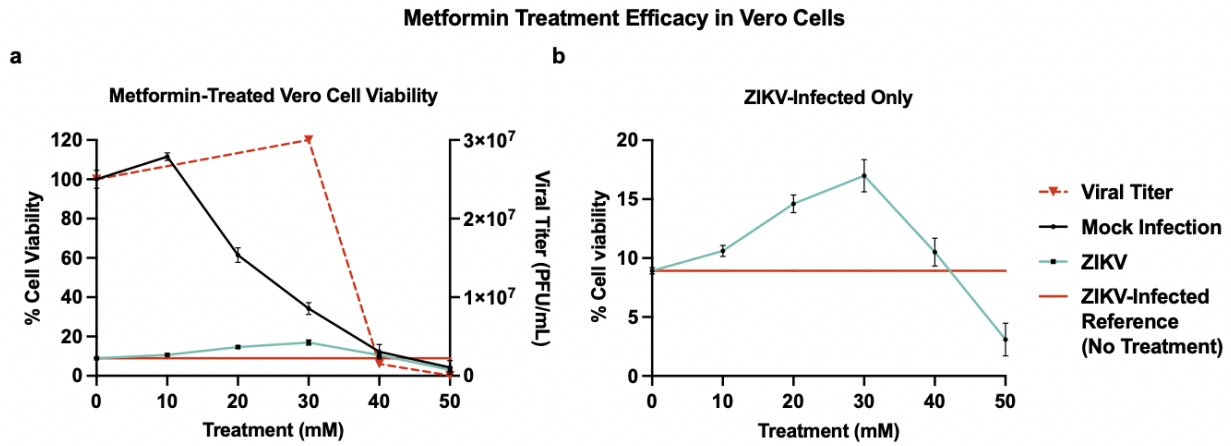

Fig. 3. Metformin treatment of mock and ZIKV-infected Vero cells. Cell viability and viral titer of viral progeny were assessed at 72 hpi with 72 hours of metformin treatment across a range of concentrations (0–50 mM). Solid lines represent cell viability quantification plotted on the left y-axis. The black line represents mock-infected cells; aquamarine lines represent ZIKV-infected cells, and red lines represent mock-treated, ZIKV-infected cells. The dotted red line represents viral titer of progeny virus in the supernatant, plotted on the right y-axis. **(a)** Metformin treatment reduced mock-infected cell viability but increased cell viability of ZIKV-infected Vero cells in a dose-dependent manner. Viral titer increases at 30 mM treatment but decreases at 40 mM and 50 mM doses. **(b)** Magnified cell viability of ZIKV-infected cells shows increased cell viability in a dose-dependent manner. Data are mean (n = 3 biological replicates; n = 12 technical replicates) ± SD.

Treatment with metformin appears to improve cell survival of ZIKV-infected Vero cells at a range of 10-40 mM metformin (**Fig. 3b**). ZIKV-infected cell viability peaks at 30 mM treatment with an overall viability of 16.99 ± 1.36%. Compared to the ZIKV-infected, mock treated negative control viability of 8.9325 ± 0.27%, this is a 1.9 fold increase in cell viability. However, we observed a large decrease of cell viability in mock-infected cells as metformin dose increases (**Fig. 3a**). Although the 10 mM metformin treatment of mock-infected cells showed slight increase in cell viability of 111.51 ± 1.90% compared to mock-treated, mock-infected cells, the overall cell viability progressively decreases for each metformin dose to 4.28 ± 3.51% at 50 mM treatment. However, viral titer of the progeny virus collected in the cell supernatant shows increase in viral titer until 30 mM treatment, followed by 100-fold decrease in titer at 40 mM and 50 mM treatments **(Fig. 3a)**. While cell viability seemingly increases for ZIKV-infected cells in the 10-40 mM metformin range, the viral titer of progeny virus only decreases with 40 mM treatment.

We further investigated the effects of metformin in NSCs. NSCs were treated 3 hpi with metformin doses ranging from 0.01 µM to 10,000 µM by a factor of 10 µM (**Fig. 4**). After 72 hours of treatment, metformin reduces cell viability of both ZIKV and mock-infected NSCs in an

inverse dose-dependent manner, with lower doses in the nanomolar range showing greater decrease in cell viability and subsequent increase in the millimolar dose range (**Fig. 4a**). Despite ZIKV infection of MOI 3, cell viability was only reduced by 10%. However, we observed decreases in cell viability of up to 55% in metformin-treated doses at 0.1 µM and 1000 µM doses, with insignificant differences between mock-infected, metformin-treated and ZIKV-infected, metformin-treated cells except at the 1 µM dose (**Fig. 4b**). While only one dose of metformin showed significant difference between the ZIKV-infected and mock-infected NSCs, most still showed insignificant decreases in ZIKV-infected cell viability compared to the mock-infected cells of the same metformin dose (**Fig. 4c**). Additionally, viral titer of the progeny virus generally decreases with metformin treatment. Mock-treated cells had a calculated titer of $1.5x10^7$ PFU/mL which is at least ten-fold higher than the lowest dose of 0.01 µM treatment.

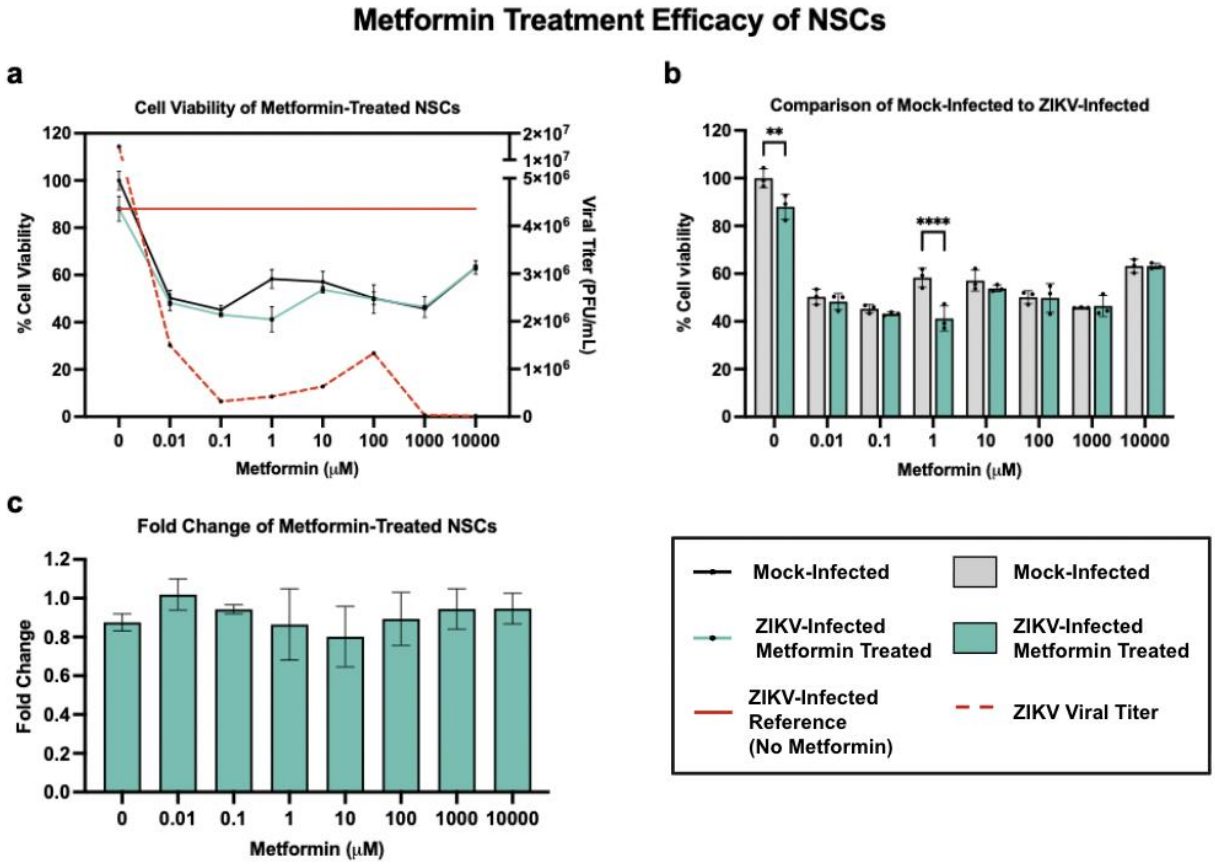

Fig. 4. Metformin treatment of mock and ZIKV-infected NSCs. Cell viability and viral titer of viral progeny were assessed at 72 hpi with 72 hours of metformin treatment across a range of concentrations (0-10,000 µM). Solid lines represent cell viability quantification plotted on the left y-axis. The black line represents mock-infected cells; aquamarine lines represent ZIKV-infected cells, and red lines represent mock-treated, ZIKV-infected cells. The dotted red line represents viral titer of progeny virus in the supernatant, plotted on the right y-axis. **(a)** Metformin reduces overall cell viability in an inverse dose-dependent manner. However, it also reduces viral titer of measured viral progeny. Data is a representative trial of n = 2 biological

replicates with each data point representing mean (n = 3 technical replicates) ± SD. **(b)** Direct comparison of mock-infected and ZIKV-infected cell viability of the same metformin dose shows insignificant differences except for mock-treated and 1 μM treated cells. **(c)** Fold change evaluation of ZIKV-infected cells to mock-infected cells of the same metformin dose show a minor decrease in cell viability of ZIKV-infected cells compared to the mock-infected cell counterpart. Data are representative of n = 2 biological replicates and n = 6 technical replicates with mean ± SD. Two-way ANOVA statistical analysis was performed to compare ZIKV and mock-infected samples. We used (**) to represent $P < 0.01$, (****) to represent $P < 0.0001$.

Given the results observed in vitro, we next investigated whether metformin could provide protective effects in vivo. Our previous work has shown that prenatal ZIKV infection decreases both postnatal survival and weight progression.[104] In mice, prenatal metformin treatment (100 mg/kg/day or 200 mg/kg/day) may or may not have affected survival in pups.[101]Data were collected from three viral batches, and analyzed collectively and separately (**Fig. 5a**). We also examined postnatal weight progression as an indicator of overall developmental health (**Fig. 5b**). No significant difference between mock-treated controls and ZIKV-infected metformin-treated postnatal weight progression was observed, suggesting metformin may restore weight loss caused by ZIKV infection.

We next assessed whether metformin treatment influenced postnatal survival and growth outcomes in pups born to ZIKV-infected dams. Pregnant dams were infected at embryonic day 9.5 (E9.5) with 7.87×10^7 PFU of ZIKV-Dak-MA. Although infections were performed using two independently prepared viral batches with different titers, dosing was normalized to deliver the same number of infectious particles across all conditions (as described in Methods, 2.4.3). Survival analysis combining data from both batches demonstrated that metformin treatment improved postnatal survival compared to DPBS-treated controls, with a dose-dependent effect observed between the 100 mg/kg/day and 200 mg/kg/day treatment groups (**Fig. 5a**).

Metformin treatment did not significantly impact postnatal growth, as all groups exhibited comparable weight trajectories from P3 to P21 (**Fig. 5b**). Direct comparison to ZIKV-infected, mock-treated controls was not feasible due to high mortality in this group, which resulted in insufficient data points for analysis. Therefore, weight comparisons were performed relative to mock-infected, mock-treated controls.

To ensure consistency of these findings across independent viral preparations, we next analyzed each batch separately. In batch 1, metformin treatment at 100 mg/kg/day showed a trend toward improved survival compared to DPBS controls, although this did not reach statistical significance ($P = 0.06$; **Fig. 5c**). No differences in weight progression were observed between treatment groups in this batch (**Fig. 5d**). In batch 2, all pups treated with metformin at 200 mg/kg/day survived to P21, supporting the survival benefit of metformin (**Fig. 5e**). As with batch 1, weight progression remained unchanged across treatment groups (**Fig. 5f**).

Together, these data demonstrate that metformin treatment improves postnatal survival in ZIKV-exposed pups in a dose-dependent manner, while not affecting postnatal growth, with consistent results observed across independently prepared viral batches.

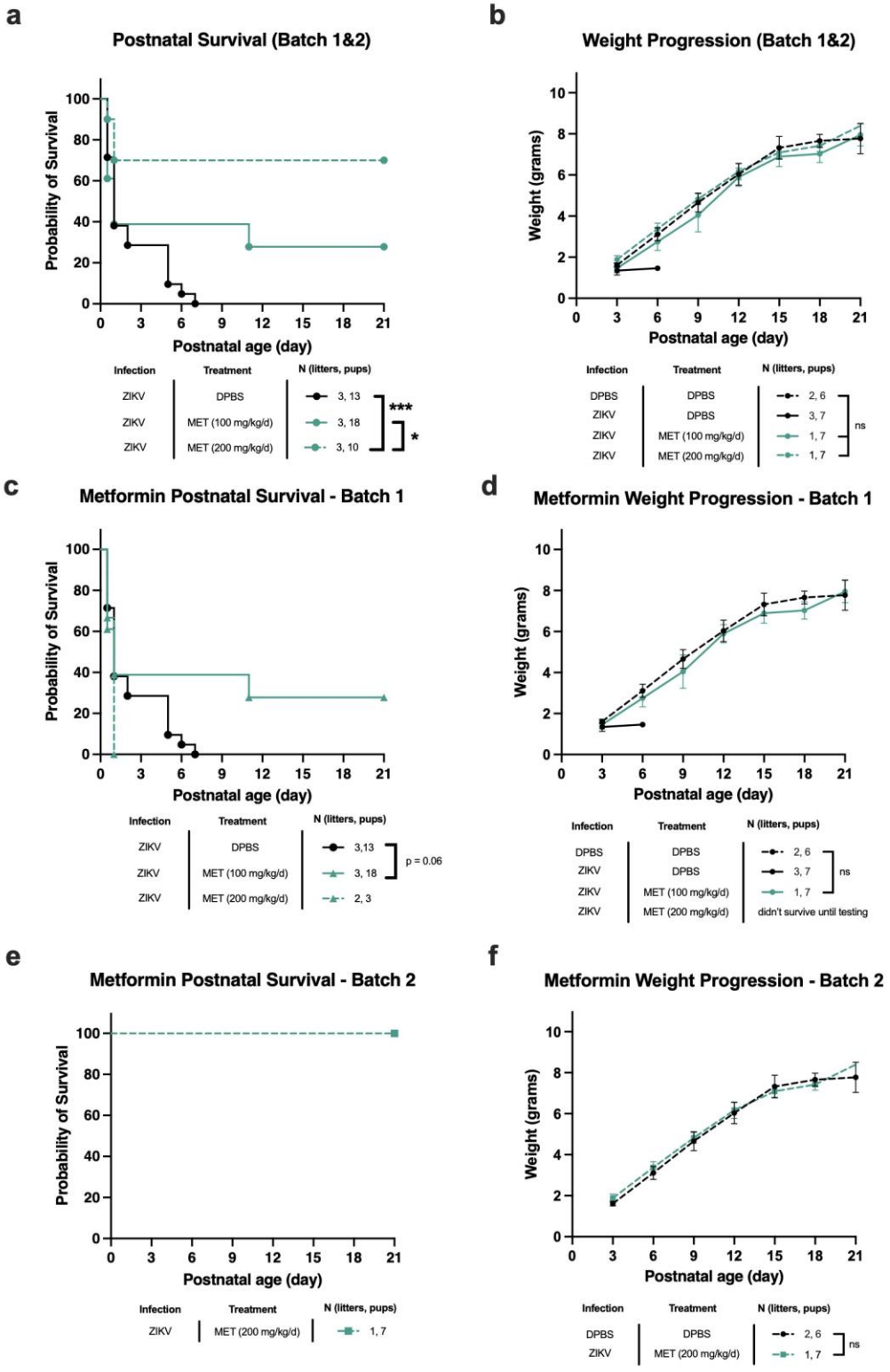

Fig. 5. Postnatal survival and weight progression of ZIKV-infected pups with metformin treatment. (a) Kaplan–Meier survival curves of pups born to ZIKV-infected dams at E9.5 and treated with DPBS, metformin (MET) 100 mg/kg/day, or MET 200 mg/kg/day, combining data from batches 1 and 2. Metformin treatment improved survival in a dose-dependent manner compared to DPBS-infected, DPBS-treated mice. **(b)** Postnatal weight progression (P3-P21) of pups across treatment groups (batches 1 and 2 combined). No significant differences in weight gain were observed between groups. **(c)** Survival analysis for batch 1 alone. Metformin at 100 mg/kg/day treatment showed a trend toward improved survival compared to DPBS controls (P = 0.06). **(d)** Weight progression (P3-P21) for batch 1, showing no significant differences between groups. **(e)** Survival analysis for batch 2. All pups in the MET 200 mg/kg/day group survived until P21. **(f)** Weight progression (P3-P21) for batch 2, demonstrating no significant differences between MET-treated and DPBS-infected, DPBS-treated groups. Data are mean ± SD. We used (***) for $P < 0.001$ and (**) for $P < 0.01$.

2.5.2 Chloroquine

We also evaluated the effects of chloroquine in the mouse model (**Fig. 6**). Prenatal chloroquine treatment did not produce a significant change in postnatal survival. As the treatment appeared to induce spontaneous abortions (**Fig. 6a**), an additional comparison was conducted between the DPBS/DPBS and DPBS/chloroquine groups to assess potential drug toxicity (**Fig. 6b)**. No significant differences were observed between these groups in either postnatal survival or weight progression (**Fig. 6c**). These findings suggest that at a dose of 50 mg/kg/day, chloroquine is likely safe but ineffective in improving pregnancy or postnatal outcomes.

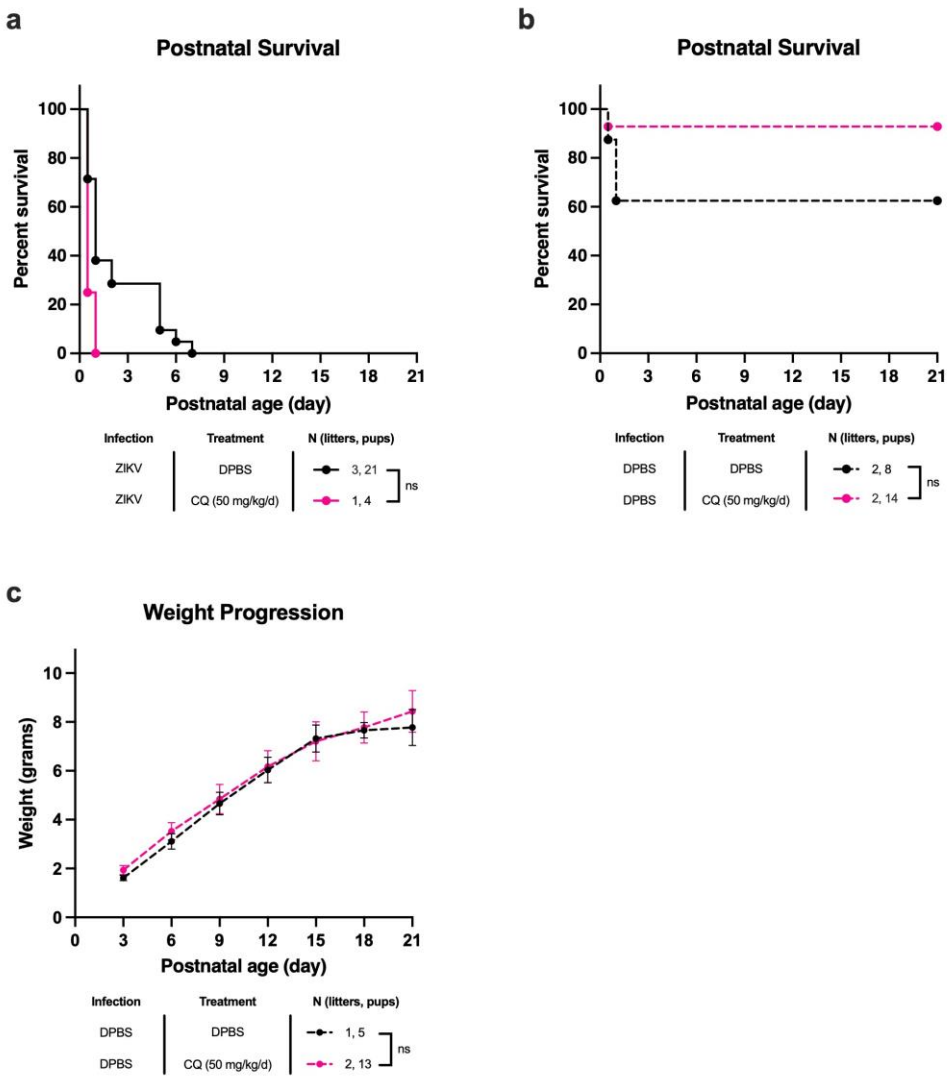

Fig. 6. Postnatal survival and weight progression of ZIKV-infected pups with chloroquine treatment. Chloroquine doses of 50 mg/kg/d were given. **(a)** In ZIKV-infected litters, chloroquine treatment did not increase postnatal survival compared to untreated controls. **(b)** Survival of mock-infected pups treated with DPBS or chloroquine showed no differences **(c)** Weight progression from P3–P21 was similar across groups, indicating that chloroquine did not impact postnatal growth. Data represents the mean ± SD.

2.5.3 Trehalose

We also evaluated the effects of trehalose in the mouse model (**Fig. 7**). Prenatal trehalose treatment did not result in a significant difference in postnatal survival, indicating that it may not be effective at a dose of 3,333 mg/kg/day.

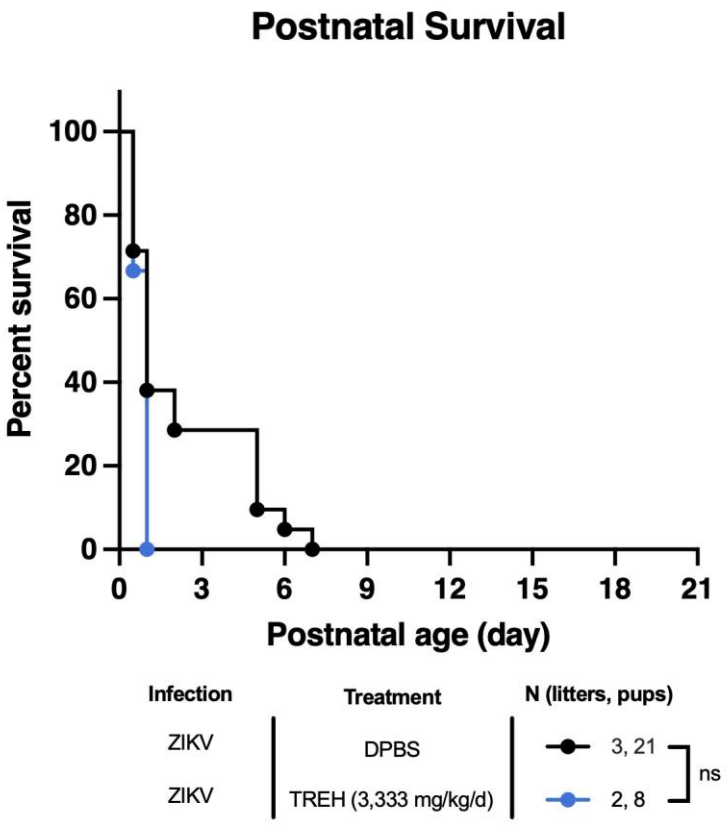

Fig. 7. Postnatal survival of ZIKV-infected pups with trehalose treatment. Postnatal survival curves for pups born to ZIKV-infected dams treated with DPBS or trehalose (3,333 mg/kg/day). Trehalose treatment did not increase survival compared to untreated controls. Data represents the mean ± SD.

2.5.4 Gross Motor Milestones

Outlined in chapter one, our previous work using this model has replicated the finding that prenatal exposure to ZIKV can exhibit developmental delays.[101] In the present study, we assessed whether treatment could impact gross and fine motor development during infancy (P3-P12), including righting reflex (**Fig. 8a**), locomotion (**Fig. 8b**), hindlimb suspension (**Fig. 8c-d**), and forelimb suspension (**Fig. 8e-f**). Data were analyzed using an extra sum-of-squares F test comparing DPBS/DPBS and/or ZIKV/DPBS to ZIKV/MET (200 mg/kd/day). For the righting reflex, mice treated with metformin (200 mg/kg/day) performed better than ZIKV/DPBS mice, but did not fully recover to the level of DPBS/DPBS controls. For locomotor movement, the 200 mg/kg/day metformin-treated group did not differ from ZIKV/DPBS mice, but remained significantly different from DPBS/DPBS controls. In limb strength assays (c-f), ZIKV-infected mice treated with metformin (200 mg/kg/day) performed comparably to DPBS + DPBS controls. Overall, these data suggest that metformin (200 mg/kg/day) improves motor outcomes following ZIKV infection, although effects are not consistent across all measures.

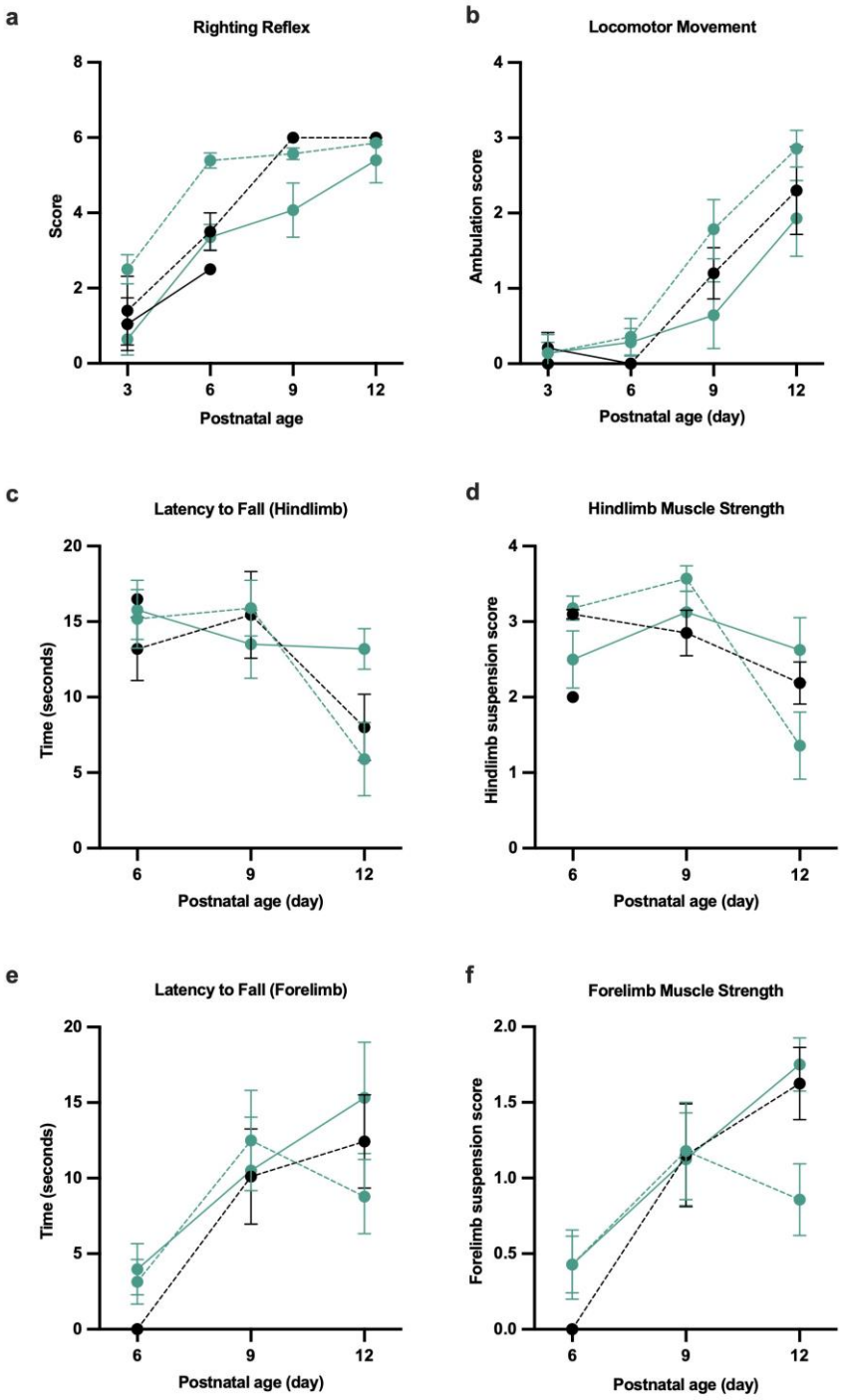

Fig. 8. Gross motor milestones. Developmental assessments of righting reflex **(a)** and locomotor movement **(b)** were performed at P3, P6, P9, and P12. Hindlimb latency to fall **(c)**, hindlimb muscle strength **(d)**, forelimb latency to fall **(e)**, and forelimb muscle strength **(f)** were performed at P6, P9, and P12. Overall, these data suggest that treatment with metformin (200 mg/kg/day) following ZIKV infection improves motor outcomes. Data represents the mean ± SD

and were analyzed using extra sum-of-squares F test comparing DPBS/DPBS and/or ZIKV/DPBS to ZIKV/MET (200 mg/kd/day).

2.5.5 Litter Size

Litter size can serve as an indicator of pregnancy health. We expected that the virus would reduce dam litters and that treatment would reverse this effect. Although the differences between groups did not reach statistical significance by one-way ANOVA ($p = 0.08$), the descriptive trends suggest that treatment effects may contribute more to variation in litter size than the infection alone. More specifically, the low-dose metformin (100 mg/kg/day) resulted in litter sizes similar to untreated controls, whereas chloroquine, high-dose metformin (200 mg/kg/day), and trehalose were associated with smaller litter sizes and, in some cases, spontaneous abortions (1–2 pups/litter) (**Fig. 10**). We observed descriptive trends in litter size across those treatment groups (**Fig. 3**). ZIKV-infected litters prenatally treated with metformin (100 mg/kg/day) had the largest observed average litter size (6 pups/litter), whereas chloroquine and trehalose treatments were associated with spontaneous abortions and smaller litter sizes (1-2 pups/litter) (**Fig. 10**).

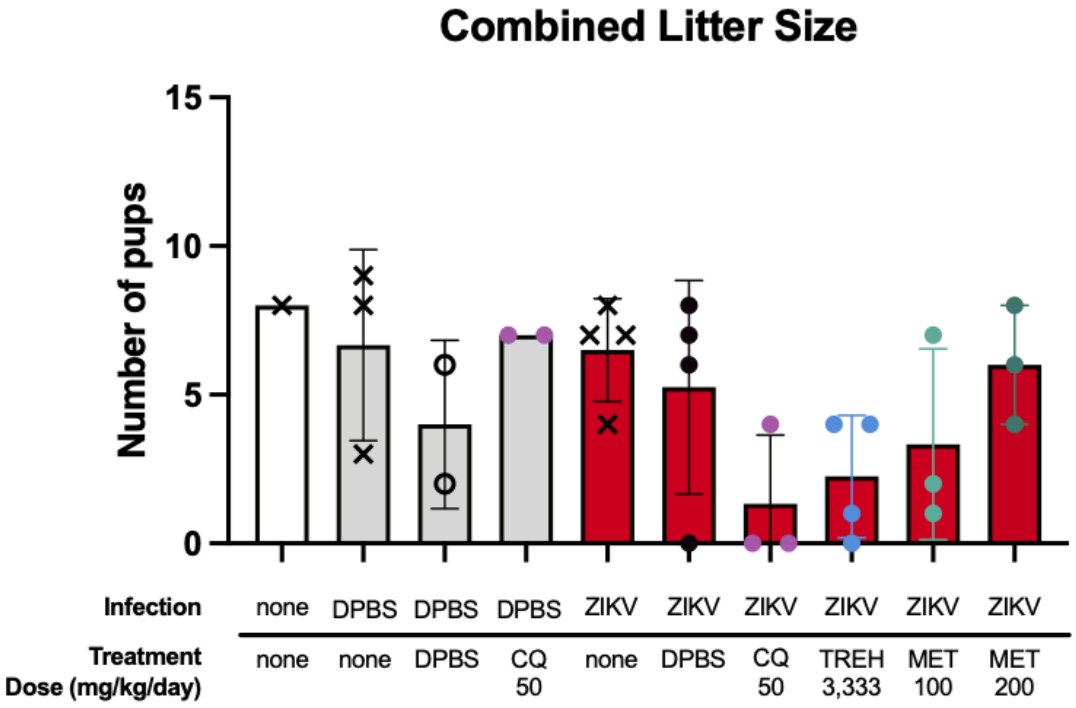

Fig. 10. Litter size. Average number of pups per litter in mock-infected (DPBS) and ZIKV-infected dams treated with DPBS, chloroquine (50 mg/kg/day), metformin (100 or 200 mg/kg/day), or trehalose (3,333 mg/kg/day). Data represent individual litters with mean ± SD.

2.5.6 Effect of Daily IP Injections

In our mouse model for prenatal ZIKV infection, pregnant dams receive ten intraperitoneal (**IP**) injections throughout gestation, which can be a source of stress. To assess the potential impact of injection frequency, we evaluated litter size, postnatal survival, and weight progression in mice that were never injected, injected once, or injected ten times (**Fig. 11**). Survival data were separated to focus specifically on whether injection frequency changes mortality over postnatal days, independent of initial litter size or postnatal growth patterns. Litter size did not differ significantly across groups, although a downward trend was observed with increased injection frequency. Postnatal survival was significantly reduced in litters from dams receiving more injections. Weight progression was not significantly affected.

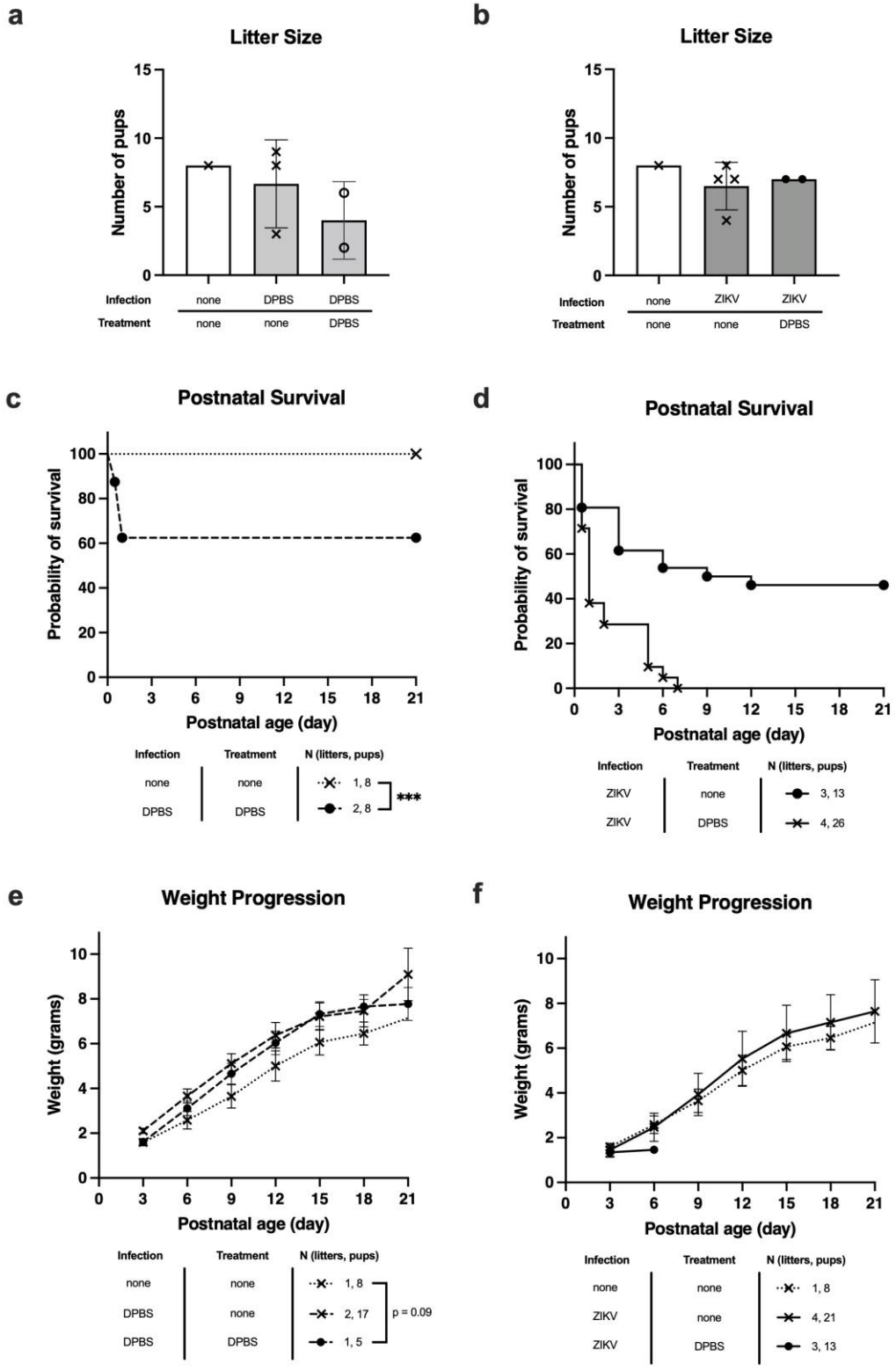

Fig. 11. Effect of daily IP injections. **(a–b)** Litter sizes from mock-infected **(a)** and ZIKV-infected **(b)** dams show no significant differences between DPBS-treated and daily IP-injected groups. **(c–d)** Postnatal survival curves for pups born to mock-infected **(c)** or ZIKV-infected **(d)**

dams indicate that daily IP injections did not alter survival outcomes. **(e–f)** Weight progression from P3–P21 in mock-infected **(e)** and ZIKV-infected **(f)** litters shows comparable growth between treatment and control groups. These findings confirm that the injection procedure itself does not impact litter viability, postnatal survival, or early growth. Data represent mean ± SD.

2.6 Discussion

2.6.1 Interpretation of Key Findings

Our results confirmed that prenatal ZIKV infection leads to outcomes consistent with CZS. Pups exposed to the virus showed reduced survival, slower weight gain, and delayed motor development. This is consistent with prior studies of ZIKV pathogenesis and supports the reliability of our model.

In vitro evaluation of metformin showed inconsistent results across different cell lines. We observed that Vero cells, known for their highly permissive nature for ZIKV infection, showed a dose-dependent increase in cell viability following metformin treatment, alongside a significant reduction in viability in mock-infected cells. While cell viability increased approximately 1.9-fold in infected cells, metformin exhibited pronounced cytotoxic effects in mock-infected Vero cells. Additionally, we observed high titers of viral progeny in metformin treatments of 10-30 mM before decreases in viral progeny titer of the 40 mM and 50 mM treatments compared to mock-treatment. In contrast, metformin showed no protective effect in ZIKV-infected NSCs. Compared to ZIKV-infected, mock-treated NSCs, metformin-treated cells exhibited consistently reduced viability. Additionally, metformin treatment of mock-infected NSCs resulted in a marked decrease in cell viability in an inverse dose-dependent manner. However, metformin notably reduced viral progeny titers at least ten-fold in every treatment dose. Notably, the reduction in viral titer may be attributed to both ZIKV replication reduction or cell death in general. Therefore, further experiments must clarify the reduction of viral titer. The magnitude of viability reduction in both mock and ZIKV-infected NSCs was comparable, suggesting that metformin-induced cytotoxicity may be independent of infection status in this cell type.

Among the tested compounds, metformin demonstrated the most consistent protective effects in vivo. Treated pups showed improved survival without significant changes in postnatal weight gain compared to infected controls, and no teratogenic effects were observed in any treatment group. These findings suggest that metformin may confer protection during prenatal ZIKV exposure, potentially by modulating host cellular pathways rather than directly inhibiting viral replication. Although earlier in vivo studies found limited benefit, our sustained dosing regimen throughout gestation was associated with a more pronounced protective effect.

Chloroquine and trehalose did not show the same benefit. Chloroquine-treated dams exhibited trends toward smaller litter sizes and increased fetal loss, while trehalose-treated groups showed poor survival and reduced litter sizes. These results may reflect limited efficacy or potential off-

target effects of these compounds in this model. The differences between our data and previous reports likely reflect variations in viral strain, dosing strategy, and timing of administration.[88,127] Overall, our results suggest that manipulating the autophagy–lysosomal pathway can change the outcome of prenatal ZIKV infection. Among the three drugs tested, metformin had the most favorable balance of safety and efficacy.

2.6.2 Mechanistic Insight

ZIKV exploits autophagy in a complex, context-dependent manner. In neural progenitor cells (NPCs), ZIKV has been shown to manipulate the Akt–mTOR pathway to induce autophagy and facilitate neurogenesis. Our findings further support the role of autophagy in ZIKV pathogenesis and suggest that targeting this pathway may offer therapeutic potential.

Metformin's observed effects are likely mediated through its regulation of the AMPK and mTOR pathways (**Fig 1**). By activating AMPK and inhibiting mTOR, metformin promotes autophagy.[110,111,113,119,128,129] This is somewhat paradoxical, given that ZIKV is known to induce autophagy as well. However, ZIKV also impairs autophagic flux by disrupting autophagosome–lysosome fusion, likely to prevent degradation of viral components.[110,111,113,119,128,129] Metformin may overcome this blockade by restoring complete autophagic flux through AMPK activation. Notably, metformin has been shown to restore autophagic flux disrupted during SARS-CoV-2 infection.[130] Additionally, metformin-induced autophagy promotes selective degradation of viral proteins such as NS3 and NS5.[130] Beyond autophagy, action of the AMPK–ULK1 pathway also stimulates lipophagy and enhances type I interferon responses.[131] Together, these mechanisms provide a plausible explanation for metformin-mediated restriction of ZIKV replication. However, further studies are needed to confirm these mechanisms and identify more specific therapeutic targets.

Interestingly, despite metformin's established role as an autophagy inducer, its antiviral effects may also involve autophagy suppression in certain contexts. A 2025 study on severe fever with thrombocytopenia syndrome virus (**SFTSV**) demonstrated that metformin inhibits viral replication through suppression of autophagy.[132] This suggests that metformin's effects on autophagy are highly context-dependent and may vary depending on the viral system.

Chloroquine showed limited efficacy in protecting against ZIKV infection in our model and was associated with smaller litters and increased spontaneous abortions. Mechanistically, chloroquine raises lysosomal pH and inhibits degradation, which can be detrimental at higher doses. ZIKV itself inhibits autophagic flux and autophagosome–lysosome fusion,[85,133] and thus chloroquine—which acts through a similar mechanism—may be ineffective in reversing these effects.[89,109,134] This aligns with our observations but contrasts with prior studies demonstrating anti-ZIKV activity of chloroquine through inhibition of endosomal release and autophagy.[89,109,134] These discrepancies can be explained by methodological differences, including our use of

hSTAT2KI/KI mice to better model intact immune signaling, compared to immunocompromised or alternative humanized models used in previous studies.[101,135]

2.6.3 Limitations

Our study had several limitations. The number of animals per treatment group was small, especially for the trehalose group, which limited statistical power. PD146176 was a fourth drug we initially aimed to evaluate due to its involvement in the autophagy and ferroptosis pathway.[136,137] However, because we were unable to deliver the drug in a consistent and uniform manner, we ultimately did not proceed with its inclusion in the study.

Additionally, daily intraperitoneal injections may have introduced stress in pregnant dams, potentially affecting pregnancy outcomes. Future studies will explore oral dosing strategies to reduce stress and improve experimental consistency.

Finally, long-term behavioral data are still being collected, and more detailed histological analyses are needed to determine whether metformin directly reduces brain injury or viral load.

2.6.4 Equity Considerations

If found to be effective in future studies, metformin is an affordable and pregnancy-safe medication that is widely used globally for other indications. Because it is easy to store and can be taken orally, it may represent a realistic option in low-resource areas where ZIKV is most common. Treatments that do not require cold-chain transport or specialized equipment would be especially useful in developing countries, including in Central and South America, where ZIKV is now endemic to the population. Metformin's accessibility makes it a promising candidate for future testing in global health contexts.

2.7 Future Directions

Our next steps will focus on confirming and expanding upon these findings. In vitro, we plan to continue metformin validation while testing chloroquine and trehalose. Additionally, we plan to test the effects of treatments on ZIKV-infected neural progenitor cells with quantification of key markers for autophagy, such as LC3.[86] We plan to continue testing the long-term developmental effects of metformin in postnatal mice.

Complementing these studies, we hope to perform prenatal analyses on brain and placental tissue. These will parallel our previous characterization seen in chapter one, incorporating staining, immunohistochemistry, and anthropometric measurements, to assess structural integrity, patterns of cell death and proliferation, and region-specific injury. This will help us directly compare treated and untreated conditions to determine whether metformin directly lowers viral replication or improves brain structure. We also hope to confirm the mechanism of

action for metformin in ZIKV treatment. This will involve determining the specific role of autophagy and potentially identifying more specific targets.

Although maternal weight was monitored as a general indicator of health, this measure alone does not fully capture the physiological effects of infection and treatment on the dam. In the future, we plan to directly assess maternal health, through measures of stress, inflammatory cytokines, viral burden, and placental histology. Maternal stress and immune activation during pregnancy can influence fetal development, so improved pup survival may be mediated in part through treatment-induced changes in maternal physiology, rather than solely direct effects on the pups.

Additionally, we plan to build full dose–response curves for each drug to better understand the window of effectiveness and toxicity. Genetic studies examining *HEXB* and *mTOR* variants could also help explain why some mice exhibit more severe outcomes than others. In the long term, these preclinical results will guide early-stage safety and feasibility studies in human populations. Partnering with maternal–fetal medicine specialists and public health researchers will be essential to facilitate translation of our findings into real-world applications.

We also plan to do in-depth studies on the mechanisms of action of our drugs, particularly metformin, given its apparent efficacy. This will involve in vitro confirmation of autophagy activation or inactivation by quantifying autophagy markers, such as LC3 or p62.[138] Alternatively, fluorescence microscopy and other imaging techniques can be utilized to visualize key stages of autophagy, potentially confirming the stage-dependent effects of these drugs.[138,139] Finally, targeted pharmacological inhibitors, like 3-MA and Chloroquine, can be used alongside metformin in vitro to confirm a reversal of the antiviral effect, thereby supporting autophagy as the operative mechanism.[140,141] In this search, more specific antiviral targets may be identified and tested.

2.8 Conclusion

Prenatal ZIKV infection remains a serious global health issue that threatens fetal brain development and carries a significant health and economic burden. Our study demonstrates that targeting the autophagy–lysosomal pathway can improve survival and development in a validated mouse model. Of all the drugs tested, metformin produced the most substantial benefit with no signs of toxicity, suggesting that it may be a viable therapeutic option for prenatal ZIKV infection.

These findings demonstrate that pharmacological rescue during pregnancy is possible. By repurposing a safe, widely available drug, this work lays a foundation for future studies that combine scientific evidence with scalable, global accessibility. Our long-term goal is to develop

treatments that not only protect the developing brain but also reach the communities that need them most.

2.9 Supplemental

We originally proposed the use of PD146176 for its direct involvement in the ferroptosis pathway and indirect effects on autophagy. Previous literature tested in vivo effects of PD146176, administering the drug in chow accessible ad libitum. However, our experimental design includes intraperitoneal treatment injections, so we attempted to incorporate PD146176 into this procedure. Unfortunately, the solubility profile of PD146176 does not allow it to be dissolved in a mouse-safe solution. Therefore, we did not continue with PD146176 for drug treatment in vivo.

2.9.1 Acknowledgements

We would like to express our deepest gratitude to our mentors, Dr. Youssef Kousa and Dr. Erin Tran, for their guidance, encouragement, and unwavering support over the last three years. Their mentorship has been invaluable in shaping our research and challenging us to grow. We are especially thankful to Eunbin Park for all her guidance, insight, and dedication in sharing her help, knowledge and experience throughout this process.

We would also like to thank our librarian, Nedelina Tchangalova, for guidance in accessing and synthesizing information. We are grateful for our thesis discussants: Dr. Yanjin Zhang, Dr. Chunbo Shao, Dr. Nat Chaimongkol, and Dr. Hannah Zierdan for their thoughtful feedback and contributions to our research.

We would like to extend our sincere appreciation for the University of Maryland Gemstone staff, including Dr. David Lovell, Dr. Allison Lansverk, Leslie Lizama, Brianna Lucas, and Janelle Dang for their continued support and encouragement throughout our time in Gemstone.

2.9.2 Publications and Presentations

During our time in the Gemstone program, multiple members of the team (bolded below) were supported in developing publications and presentations. We would like to acknowledge the following:

Published Manuscripts

Abdelmalek, C. M., Singh, S., Fasil, B., Horvath, A. R., Mulkey, S. B., Curé, C., Campos, M., Cavalcanti, D. P., Tong, V. T., Mercado, M., Daza, M., Benavides, M. M., Acosta, J., Gilboa, S., Valencia, D., Sancken, C. L., Newton, S., Scalabrin, D. M. F., Mussi-Pinhata, M. M., Vasconcelos, Z., … Kousa, Y. A. (2025). Building a growing genomic repository for maternal and fetal health through the PING Consortium. Pediatric research, 10.1038/s41390-024-03793-1. Advance online publication. https://doi.org/10.1038/s41390-024-03793-1

Marques, F.J.P., **Ruan, J.**, Razal, R.B. et al. A Scoping Review of Genetic Risk Factors Possibly Impacting Virally Induced Brain Injury After Zika Infection. Pediatr Res 98, 2530–2535 (2025). https://doi.org/10.1038/s41390-025-04252-1

Manuscripts Under Review

Horvath, A. R. †, **Abdelmalek, C. M.** †, Park, E., **Alexander, A. P.**, Chaimongkol, N., Aquino, J., Dolan, W. L., Matheswaran, S. A., **Patel, A. H.**, **Patel, N. G.**, **Ruan, J. E.**, **Adeyemo, A. T.**, **Li, E. C.**, Gerlein, M., Helmicki, K. E., Lin, S., Wang, P. C., Li, Z., Wang, L., Gordish-Dressman, H. A., Ku, W. L., Haydar, T. F., Mansour, T. A., & Kousa, Y. A. (2025). Zika Infection During a Critical Window Leads to Neural Progenitor Collapse and Brain Injury. bioRxiv : the preprint server for biology, 2025.02.21.639556. https://doi.org/10.1101/2025.02.21.639556

Chiaratti de Oliveira, A., Kang, Z., **Alexander, A.**, Pires Vieira, A. L., Santos Junior, A., Lima, A., Alves da Frota, M., Neves de Andrade, A., Nepomuceno, P., Donnamaria Morais, R., Coda Pinto Alves Campos Vieira, S. M., Afrange, E., Girão Sinnes, E., PING Consortium, Kousa, Y. A., & Goulart, A. L. (under review). Optimizing developmental outcomes in premature infants through a multidisciplinary approach to care. Manuscript under review at Pediatric Research.

Manuscripts in Preparation

Li, E., Zhou, Y., Chaimongkol, N., Razal, R., Park, E., Tran, L., Cunningham, G., Kousa, Y (manuscript in preparation). Optimization of sensitive HPLC-UV quantification of GM2 with non-toxic reducing reagent. Manuscript drafted for Analytical Biochemistry.

Hussain, H., Razal, R., Kousa, Y. (manuscript in preparation). The role of gangliosides in viral attachment and entry.

Poster Presentations

CM Abdelmalek,* **AP Alexander**,* **EC Li**,* E Park, YA Kousa. Using precision therapies to protect the developing brain from viral infection and injury. Undergraduate Neuroscience Research Fair, University of Maryland. College Park, MD (May 2026).

CM Abdelmalek, AP Alexander, E Park, YA Kousa. *Using Precision Therapies to Protect the Developing Brain from Viral Infection and Injury*. Research, Education & Innovation Week, Children's National Hospital. Washington, DC. (April, 2026).

J Ruan, F Marques, R Razal, M Leyser, Y Kousa. *Genetic Risk Factors Possibly Impacting Virally Induced Brain Injury After Zika Infection: A Scoping Review*. Research, Education & Innovation Week, Children's National Hospital. Washington, DC. (April, 2026).

E Park, A Horvath, **J Ruan, A Patel, A Alexander, C Abdelmalek,** R Razal, L Tran, N Chaimongkol, Y Kousa. *HexB Deficient Mice Exhibit Enhanced Neurodevelopmental Pathology Following Zika Virus Infection*. Research, Education & Innovation Week, Children's National Hospital. Washington, DC. (April, 2026).

R Razal, N Chaimongkol, AR Horvath, LA Tran, **CM Abdelmalek**, E Park, T Mansour, YA Kousa. Genetic Variation in HEXB and GM2 Metabolism Modifies Prenatal Viral Infection and Brain Injury. Annual Meeting of the American Neurological Association. Baltimore, MD (September 2025).

CM Abdelmalek, AP Alexander, E Park, YA Kousa. *Using precision therapies to protect the developing brain from viral infection and injury.* APSA Mid-Atlantic Regional Conference. Philadelphia, PA (June 2025).

CM Abdelmalek, AP Alexander, E Park, YA Kousa. *Using precision therapies to protect the developing brain from viral infection and injury.* Research, Education & Innovation Week, Children's National Hospital. Washington, DC (April 2025).

AP Alexander, CM Abdelmalek, AR Horvath, YA Kousa. *Prenatal Zika Infection Restricts TBR2-Positive Cells in the Developing Brain.* Research, Education & Innovation Week, Children's National Hospital. Washington, DC (April 2025).

CM Abdelmalek, AT Adeyemo, AP Alexander, EC Li, AH Patel, NG Patel, JE Ruan, AR Horvath, YA Kousa. *Optimizing Nissl Staining to Evaluate Prenatal Virally-Induced Brain Injury.* Research, Education & Innovation Week, Children's National Hospital. Washington, DC (April 2025).

SA Aldesoky, **E Li**, C Shao, YA Kousa. *A Novel Rapid and Sensitive Quantification Assay for the Detection of Zika Virus by qRT-PCR*. Research, Education & Innovation Week, Children's National Hospital. Washington, DC (April 2025)

E Li, SA Aldesoky, C Shao, YA Kousa. *Evaluating the Oncolytic Potential of Zika Virus in Brain Tumors.* Research, Education & Innovation Week, Children's National Hospital. Washington, DC (April 2025)

CM Abdelmalek, AP Alexander, E Park, YA Kousa. *Using precision therapies to protect the developing brain from viral infection and injury.* Undergraduate Research Day, University of Maryland. College Park, MD. (April 2025).

CM Abdelmalek, AP Alexander, E Park, YA Kousa. *Using precision therapies to protect the developing brain from viral infection and injury.* Neuroscience Research Day, University of Maryland. College Park, MD (April 2025).

CM Abdelmalek, B Fasil, S Singh, AR Horvath, YA Kousa. *Building a growing genomic data repository for maternal and fetal health through the PING Consortium.* CNH-NIAID Symposium. Washington, DC (September 2024).

AR Horvath, **CM Abdelmalek,** S Matheswaran, **A Alexander, N Patel, J Ruan, A Adeyemo, A Patel**, K Helmicki, YA Kousa. *Establishing an immunocompetent humanized model of prenatal Zika virus infection*. CNH-NIAID Symposium. Washington, DC (September 2024).

B Fasil, LA Tran, **CM Abdelmalek,** YA Kousa. *Analyzing the PING Cohorts: A Comparative Analysis of Zika Exposed Infants Across the Americas.* CNH-NIAID Symposium. Washington, DC (September 2024).

AP Alexander, AT Adeyemo, NG Patel, JE Ruan, AH Patel, CM Abdelmalek, AR Horvath, YA Kousa. *Standardizing a Histological Model for Virally Induced Prenatal Brain Injury.* CNH-NIAID Symposium. Washington, DC (September 2024).

CM Abdelmalek, B Fasil, S Singh, AR Horvath, YA Kousa. *Building a growing genomic data repository for maternal and fetal health through the PING Consortium.* Research, Education & Innovation Week, Children's National Hospital. Washington, DC. (April, 2024). *Awarded 1st place in Global Public Health in the High School & Undergraduate Category*

AP Alexander, AT Adeyemo, NG Patel, JE Ruan, AH Patel, AR Horvath, YA Kousa. *Standardizing a Histological Model for Virally Induced Prenatal Brain Injury.* Research, Education & Innovation Week, Children's National Hospital. Washington, DC. (April, 2024).

A Horvath, **C Abdelmalek**, S Matheswaran, **A Alexander, N Patel, J Ruan, A Adeyemo, A Patel**, K Helmicki, Y Kousa. *Establishing an immunocompetent humanized model of prenatal Zika virus infection.* Research, Education & Innovation Week, Children's National Hospital. Washington, DC. (April, 2024)

B Fasil, LA Tran, **CM Abdelmalek**, YA Kousa. *Analyzing the PING Cohorts: A Comparative Analysis of Zika Exposed Infants Across the Americas.* Research, Education & Innovation Week, Children's National Hospital. Washington, DC. (April, 2024)

CM Abdelmalek, B Fasil, S Singh, AR Horvath, YA Kousa. *Building a growing genomic data repository for maternal and fetal health through the PING Consortium*. Neuroscience Research Day, University of Maryland. College Park, Maryland (April 2024).

CM Abdelmalek, B Fasil, AR Horvath, L Henderson, YA Kousa. *Bioinformatic Analysis of Zika Virus Quantitatively Evaluates Protein-Coding Mutations.* Neuroscience Research Day, University of Maryland. College Park, Maryland. (April 2023).

B Fasil, **CM Abdelmalek**, AR Horvath, YA Kousa. *Developing a Preclinical Model of Virally Induced Prenatal Brain Injury.* Research, Education & Innovation Week, Children's National Hospital. Washington, DC. (April 2023).

AR Horvath, S Matheswaran, B Fasil, **CM Abdelmalek**, YA Kousa. *Characterizing Neurological Consequences from Prenatal Zika Virus Infection*. Research, Education & Innovation Week, Children's National Hospital. Washington, DC. (April 2023).

2.10 Citations

1. Pielnaa P, Al-Saadawe M, Saro A, et al. Zika virus-spread, epidemiology, genome, transmission cycle, clinical manifestation, associated challenges, vaccine and antiviral drug development. *Virology*. 2020;543:34-42. doi:10.1016/j.virol.2020.01.015

2. Chiu CF, Chu LW, Liao IC, et al. The Mechanism of the Zika Virus Crossing the Placental Barrier and the Blood-Brain Barrier. *Front Microbiol*. 2020;11:214. doi:10.3389/fmicb.2020.00214

3. World Health Organization. The history of Zika virus. February 7, 2016. Accessed October 17, 2023. https://www.who.int/news-room/feature-stories/detail/the-history-of-zika-virus

4. Freitas DA, Souza-Santos R, Carvalho LMA, et al. Congenital Zika syndrome: A systematic review. *PloS One*. 2020;15(12):e0242367. doi:10.1371/journal.pone.0242367

5. Woodson SE, Morabito KM. Continuing development of vaccines and monoclonal antibodies against Zika virus. *Npj Vaccines*. 2024;9(1):91. doi:10.1038/s41541-024-00889-x

6. Caine EA, Jagger BW, Diamond MS. Animal Models of Zika Virus Infection during Pregnancy. *Viruses*. 2018;10(11):598. doi:10.3390/v10110598

7. Mesci P, Macia A, Moore SM, et al. Blocking Zika virus vertical transmission. *Sci Rep*. 2018;8(1):1218. doi:10.1038/s41598-018-19526-4

8. Julander JG, Siddharthan V, Park AH, et al. Consequences of in utero exposure to Zika virus in offspring of AG129 mice. *Sci Rep*. 2018;8(1):9384. doi:10.1038/s41598-018-27611-x

9. Li P, Ke X, Wang T, et al. Zika Virus Attenuation by Codon Pair Deoptimization Induces Sterilizing Immunity in Mouse Models. *J Virol*. 2018;92(17):10.1128/jvi.00701-18. doi:10.1128/jvi.00701-18

10. Cugola FR, Fernandes IR, Russo FB, et al. The Brazilian Zika virus strain causes birth defects in experimental models. *Nature*. 2016;534(7606):267-271. doi:10.1038/nature18296

11. Sapparapu G, Fernandez E, Kose N, et al. Neutralizing human antibodies prevent Zika virus replication and fetal disease in mice. *Nature*. 2016;540(7633):443-447. doi:10.1038/nature20564

12. Regla-Nava JA, Elong Ngono A, Viramontes KM, et al. Cross-reactive Dengue virus-specific CD8+ T cells protect against Zika virus during pregnancy. *Nat Commun*. 2018;9(1):3042. doi:10.1038/s41467-018-05458-0

13. Shi Y, Li S, Wu Q, et al. Vertical Transmission of the Zika Virus Causes Neurological Disorders in Mouse Offspring. *Sci Rep*. 2018;8(1):3541. doi:10.1038/s41598-018-21894-w

14. Miner JJ, Cao B, Govero J, et al. Zika Virus Infection during Pregnancy in Mice Causes Placental Damage and Fetal Demise. *Cell*. 2016;165(5):1081-1091.

15. Yockey LJ, Varela L, Rakib T, et al. Vaginal Exposure to Zika Virus during Pregnancy Leads to Fetal Brain Infection. *Cell*. 2016;166(5):1247-1256.e4.

16. Wu KY, Zuo GL, Li XF, et al. Vertical transmission of Zika virus targeting the radial glial cells affects cortex development of offspring mice. *Cell Res*. 2016;26(6):645-654. doi:10.1038/cr.2016.58

17. Shao Q, Herrlinger S, Zhu YN, et al. The African Zika virus MR-766 is more virulent and causes more severe brain damage than current Asian lineage and dengue virus. *Development*. 2017;144(22):4114-4124. doi:10.1242/dev.156752

18. Cui L, Zou P, Chen E, et al. Visual and Motor Deficits in Grown-up Mice with Congenital Zika Virus Infection. *EBioMedicine*. 2017;20:193-201. doi:10.1016/j.ebiom.2017.04.029

19. Grant A, Ponia SS, Tripathi S, et al. Zika Virus Targets Human STAT2 to Inhibit Type I Interferon Signaling. *Cell Host Microbe*. 2016;19(6):882-890. doi:10.1016/j.chom.2016.05.009

20. Kumar A, Hou S, Airo AM, et al. Zika virus inhibits type-I interferon production and downstream signaling. *EMBO Rep*. 2016;17(12):1766-1775. doi:10.15252/embr.201642627

21. Slayden OD. Cyclic remodeling of the nonhuman primate endometrium: a model for understanding endometrial receptivity. *Semin Reprod Med*. 2014;32(5):385-391. doi:10.1055/s-0034-1376357

22. Stouffer RL, Woodruff TK. Nonhuman Primates: A Vital Model for Basic and Applied Research on Female Reproduction, Prenatal Development, and Women's Health. *ILAR J*. 2017;58(2):281-294. doi:10.1093/ilar/ilx027

23. Ashour J, Morrison J, Laurent-Rolle M, et al. Mouse STAT2 restricts early dengue virus replication. *Cell Host Microbe*. 2010;8(5):410-421. doi:10.1016/j.chom.2010.10.007

24. Dudley DM, Aliota MT, Mohr EL, et al. A rhesus macaque model of Asian-lineage Zika virus infection. *Nat Commun*. 2016;7(1):12204. doi:10.1038/ncomms12204

25. Nguyen SM, Antony KM, Dudley DM, et al. Highly efficient maternal-fetal Zika virus transmission in pregnant rhesus macaques. *PLOS Pathog*. 2017;13(5):e1006378. doi:10.1371/journal.ppat.1006378

26. Martinot AJ, Abbink P, Afacan O, et al. Fetal Neuropathology in Zika Virus-Infected Pregnant Female Rhesus Monkeys. *Cell*. 2018;173(5):1111-1122.e10. doi:10.1016/j.cell.2018.03.019

27. Hirsch AJ, Roberts VHJ, Grigsby PL, et al. Zika virus infection in pregnant rhesus macaques causes placental dysfunction and immunopathology. *Nat Commun*. 2018;9(1):263. doi:10.1038/s41467-017-02499-9

28. Magnani DM, Rogers TF, Maness NJ, et al. Fetal demise and failed antibody therapy during Zika virus infection of pregnant macaques. *Nat Commun*. 2018;9(1):1624. doi:10.1038/s41467-018-04056-4

29. Coffey LL, Keesler RI, Pesavento PA, et al. Intraamniotic Zika virus inoculation of pregnant rhesus macaques produces fetal neurologic disease. *Nat Commun*. 2018;9(1):2414. doi:10.1038/s41467-018-04777-6

30. Adams Waldorf KM, Stencel-Baerenwald JE, Kapur RP, et al. Fetal brain lesions after subcutaneous inoculation of Zika virus in a pregnant nonhuman primate. *Nat Med*. 2016;22(11):1256-1259. doi:10.1038/nm.4193

31. Szaba FM, Tighe M, Kummer LW, et al. Zika virus infection in immunocompetent pregnant mice causes fetal damage and placental pathology in the absence of fetal infection. *PLOS Pathog*. 2018;14(4):e1006994. doi:10.1371/journal.ppat.1006994

32. Vermillion MS, Lei J, Shabi Y, et al. Intrauterine Zika virus infection of pregnant immunocompetent mice models transplacental transmission and adverse perinatal outcomes. *Nat Commun*. 2017;8:14575. doi:10.1038/ncomms14575

33. Alippe Y, Wang L, Coskun R, et al. Fetal MAVS and type I IFN signaling pathways control ZIKV infection in the placenta and maternal decidua. *J Exp Med*. 2024;221(9):e20240694. doi:10.1084/jem.20240694

34. Krause KK, Azouz F, Shin OS, Kumar M. Understanding the Pathogenesis of Zika Virus Infection Using Animal Models. *Immune Netw*. 2017;17(5):287-297. doi:10.4110/in.2017.17.5.287

35. Gorman MJ, Caine EA, Zaitsev K, et al. An immunocompetent mouse model of Zika virus infection. *Cell Host Microbe*. 2018;23(5):672-685.e6. doi:10.1016/j.chom.2018.04.003

36. Al Shoyaib A, Archie SR, Karamyan VT. Intraperitoneal Route of Drug Administration: Should it Be Used in Experimental Animal Studies? *Pharm Res*. 2019;37(1):12. doi:10.1007/s11095-019-2745-x

37. Turner PV, Brabb T, Pekow C, Vasbinder MA. Administration of Substances to Laboratory Animals: Routes of Administration and Factors to Consider. *J Am Assoc Lab Anim Sci JAALAS*. 2011;50(5):600-613.

38. Lazear HM, Govero J, Smith AM, et al. A mouse model of Zika virus pathogenesis. *Cell Host Microbe*. 2016;19(5):720-730. doi:10.1016/j.chom.2016.03.010

39. Elmore SA, Cochran RZ, Bolon B, et al. Histology Atlas of the Developing Mouse Placenta. *Toxicol Pathol*. 2022;50(1):60-117. doi:10.1177/01926233211042270

40. McEwan F, Glazier JD, Hager R. The impact of maternal immune activation on embryonic brain development. *Front Neurosci*. 2023;17. doi:10.3389/fnins.2023.1146710

41. Hindle S, Depatureaux A, Fortin-Dion S, et al. Zika virus infection during pregnancy and vertical transmission: case reports and peptide-specific cell-mediated immune responses. *Arch Virol*. 2024;169(2):32. doi:10.1007/s00705-023-05952-x

42. Melo AS de O, Aguiar RS, Amorim MMR, et al. Congenital Zika Virus Infection: Beyond Neonatal Microcephaly. *JAMA Neurol*. 2016;73(12):1407-1416. doi:10.1001/jamaneurol.2016.3720

43. Driggers RW, Ho CY, Korhonen EM, et al. Zika Virus Infection with Prolonged Maternal Viremia and Fetal Brain Abnormalities. *N Engl J Med*. 2016;374(22):2142-2151. doi:10.1056/NEJMoa1601824

44. Besnard M, Eyrolle-Guignot D, Guillemette-Artur P, et al. Congenital cerebral malformations and dysfunction in fetuses and newborns following the 2013 to 2014 Zika virus epidemic in French Polynesia. *Euro Surveill Bull Eur Sur Mal Transm Eur Commun Dis Bull*. 2016;21(13). doi:10.2807/1560-7917.ES.2016.21.13.30181

45. Honein MA, Dawson AL, Petersen EE, et al. Birth Defects Among Fetuses and Infants of US Women With Evidence of Possible Zika Virus Infection During Pregnancy. *JAMA*. 2017;317(1):59-68. doi:10.1001/jama.2016.19006

46. Brasil P, Pereira JP, Moreira ME, et al. Zika Virus Infection in Pregnant Women in Rio de Janeiro. *N Engl J Med*. 2016;375(24):2321-2334. doi:10.1056/NEJMoa1602412

47. Carvalho-Sauer R, Costa M da CN, Barreto FR, Teixeira MG. Congenital Zika Syndrome: Prevalence of low birth weight and associated factors. Bahia, 2015-2017. *Int J Infect Dis IJID Off Publ Int Soc Infect Dis*. 2019;82:44-50. doi:10.1016/j.ijid.2019.02.040

48. Mulkey SB, Bulas DI, Vezina G, et al. Sequential Neuroimaging of the Fetus and Newborn With In Utero Zika Virus Exposure. *JAMA Pediatr*. 2019;173(1):52-59. doi:10.1001/jamapediatrics.2018.4138

49. Alves LV, Hazin AN, Alves JGB. Neuroimaging in Children Born With Congenital Zika Syndrome: A Cohort Study. *J Child Neurol*. 2021;36(12):1066-1070. doi:10.1177/08830738211027719

50. Rose CE, Bertolli J, Attell JE, et al. Early Growth Parameters as Predictors of Developmental Delay among Children Conceived During the 2015–2016 Zika Virus Outbreak in Northeastern Brazil. *Trop Med Infect Dis*. 2020;5(4):155. doi:10.3390/tropicalmed5040155

51. Schuler-Faccini L, del Campo M, García-Alix A, et al. Neurodevelopment in Children Exposed to Zika in utero: Clinical and Molecular Aspects. *Front Genet*. 2022;13. doi:10.3389/fgene.2022.758715

52. Mulkey SB, Corn E, Williams ME, et al. Neurodevelopmental Outcomes of Normocephalic Colombian Children with Antenatal Zika Virus Exposure at School Entry. *Pathogens*. 2024;13(2):170. doi:10.3390/pathogens13020170

53. Kousa YA, Hossain RA. Causes of phenotypic variability and disabilities after prenatal viral infections. *Trop Med Infect Dis*. 2021;6(2):2. doi:10.3390/tropicalmed6020095

54. Zhao Z, Shang Z, Vasconcelos Z, et al. Zika Virus Infection Leads to Variable Defects in Multiple Neurological Functions and Behaviors in Mice and Children. *Adv Sci*. 2020;7(18):1901996. doi:10.1002/advs.201901996

55. Bhatnagar J, Rabeneck DB, Martines RB, et al. Zika Virus RNA Replication and Persistence in Brain and Placental Tissue. *Emerg Infect Dis*. 2017;23(3):405-414. doi:10.3201/eid2303.161499

56. Abrams RPM, Yasgar A, Teramoto T, et al. Therapeutic candidates for the Zika virus identified by a high-throughput screen for Zika protease inhibitors. *Proc Natl Acad Sci U S A*. 2020;117(49):31365-31375. doi:10.1073/pnas.2005463117

57. Neelam V, Woodworth KR, Chang DJ, et al. Outcomes up to age 36 months after congenital Zika virus infection-U.S. states. *Pediatr Res*. 2024;95(2):558-565. doi:10.1038/s41390-023-02787-9

58. Moadab G, Pittet F, Bennett JL, et al. Prenatal Zika virus infection has sex-specific effects on infant physical development and mother-infant social interactions. *Sci Transl Med*. 2023;15(719):eadh0043. doi:10.1126/scitranslmed.adh0043

59. Brien JD, Uhrlaub JL, Hirsch A, Wiley CA, Nikolich-Žugich J. Key role of T cell defects in age-related vulnerability to West Nile virus. *J Exp Med*. 2009;206(12):2735-2745. doi:10.1084/jem.20090222

60. Yang F, Zheng Q, Jin L. Dynamic Function and Composition Changes of Immune Cells During Normal and Pathological Pregnancy at the Maternal-Fetal Interface. *Front Immunol*. 2019;10:2317. doi:10.3389/fimmu.2019.02317

61. Chen S, Shenoy A. Placental Pathology and the Developing Brain. *Semin Pediatr Neurol*. 2022;42:100975. doi:10.1016/j.spen.2022.100975

62. Rabelo K, de Souza LJ, Salomão NG, et al. Zika Induces Human Placental Damage and Inflammation. *Front Immunol*. 2020;11:2146. doi:10.3389/fimmu.2020.02146

63. Shelton SM, Soucy AR, Kurzion R, Zeldich E, Connor JH, Haydar TF. Forebrain neural precursor cells are differentially vulnerable to Zika virus infection. *eNeuro*. 2021;8(5). doi:10.1523/ENEURO.0108-21.2021

64. Yao B, Christian KM, He C, Jin P, Ming GL, Song H. Epigenetic mechanisms in neurogenesis. *Nat Rev Neurosci*. 2016;17(9):537-549. doi:10.1038/nrn.2016.70

65. Pinato L, Ribeiro EM, Leite RFP, et al. Sleep findings in Brazilian children with congenital Zika syndrome. *Sleep*. 2018;41(3):zsy009. doi:10.1093/sleep/zsy009

66. Cristina da Silva Rosa B, Hernandez Alves Ribeiro César CP, Paranhos LR, Guedes-Granzotti RB, Lewis DR. Speech-language disorders in children with congenital Zika virus syndrome: A systematic review. *Int J Pediatr Otorhinolaryngol*. 2020;138:110309. doi:10.1016/j.ijporl.2020.110309

67. Marques FJP, Tran L, Kousa YA, Leyser M. Long-term developmental outcomes of children with congenital Zika syndrome. *Pediatr Res*. 2025;97(3):989-993. doi:10.1038/s41390-024-03389-9

68. Carvalho A, Brites C, Mochida G, et al. Clinical and neurodevelopmental features in children with cerebral palsy and probable congenital Zika. *Brain Dev*. 2019;41(7):587-594. doi:10.1016/j.braindev.2019.03.005

69. Ball EE, Bennett JL, Keesler RI, Van Rompay KKA, Coffey LL, Bliss-Moreau E. Prenatal Zika virus exposure is associated with lateral geniculate nucleus abnormalities in juvenile

rhesus macaques. *Neuroreport*. 2023;34(16):786-791. doi:10.1097/WNR.0000000000001953

70. Gabriel E, Ramani A, Altinisik N, Gopalakrishnan J. Human Brain Organoids to Decode Mechanisms of Microcephaly. *Front Cell Neurosci*. 2020;14. doi:10.3389/fncel.2020.00115

71. Wheeler AC, Toth D, Ridenour T, et al. Developmental Outcomes Among Young Children With Congenital Zika Syndrome in Brazil. *JAMA Netw Open*. 2020;3(5):e204096. doi:10.1001/jamanetworkopen.2020.4096

72. Marques FJP, Amarante C, Elias MAC, Klein R, Nascimento OJM, Leyser M. Neurodevelopmental outcomes in a cohort of children with congenital Zika syndrome at 12 and 24 months of age. *Child Care Health Dev*. 2023;49(2):304-310. doi:10.1111/cch.13044

73. Soares de Oliveira-Szejnfeld P, Levine D, Melo AS de O, et al. Congenital Brain Abnormalities and Zika Virus: What the Radiologist Can Expect to See Prenatally and Postnatally. *Radiology*. 2016;281(1):203-218. doi:10.1148/radiol.2016161584

74. Lean SC, Derricott H, Jones RL, Heazell AEP. Advanced maternal age and adverse pregnancy outcomes: A systematic review and meta-analysis. *PloS One*. 2017;12(10):e0186287. doi:10.1371/journal.pone.0186287

75. Janecka M, Mill J, Basson MA, et al. Advanced paternal age effects in neurodevelopmental disorders—review of potential underlying mechanisms. *Transl Psychiatry*. 2017;7(1):e1019. doi:10.1038/tp.2016.294

76. Al Beloushi M, Saleh H, Ahmed B, Konje JC. Congenital and Perinatal Viral Infections: Consequences for the Mother and Fetus. *Viruses*. 2024;16(11):1698. doi:10.3390/v16111698

77. Alvarado MG, Schwartz DA. Zika Virus Infection in Pregnancy, Microcephaly, and Maternal and Fetal Health. *Arch Pathol Lab Med*. 2017;141(1):26-32.

78. Baud D, Gubler DJ, Schaub B, Lanteri MC, Musso D. An update on Zika virus infection. *Lancet*. 2017;390(10107):2099-2109. doi:10.1016/S0140-6736(17)31450-2

79. Galel SA, Williamson PC, Busch MP, et al. First Zika-positive donations in the continental United States. *Transfusion (Paris)*. 2017;57(3pt2):762-769.

80. Musso D, Gubler DJ. Zika Virus. *Clin Microbiol Rev*. 2016;29(3):487-524. doi:10.1128/CMR.00072-15

81. Musso Didier, Ko Albert I., Baud David. Zika Virus Infection — After the Pandemic. *N Engl J Med*. 2019;381(15):1444-1457. doi:10.1056/NEJMra1808246

82. Nigro G. Hyperimmune globulin in pregnancy for the prevention of congenital cytomegalovirus disease. *Expert Rev Anti Infect Ther*. 2017;15(11):977-986. doi:10.1080/14787210.2017.1398081

83. Bonam SR, Wang F, Muller S. Lysosomes as a therapeutic target. *Nat Rev Drug Discov*. 2019;18(12):923-948. doi:10.1038/s41573-019-0036-1

84. Cao B, Parnell L, Diamond M, Mysorekar I. Inhibition of autophagy limits vertical transmission of Zika virus in pregnant mice. *J Exp Med*. 2017;214(8):2303-2313. doi:https://doi.org/10.1084/jem.20170957

85. Ma X, Jia Y, Yuan J, et al. Inhibiting cardiac autophagy suppresses Zika virus replication. *J Med Virol*. 2023;95(2):e28483. doi:10.1002/jmv.28483

86. Peng H, Liu B, Yves TD, et al. Zika virus induces autophagy in human umbilical vein endothelial cells. *Viruses*. 2018;10(5):5. doi:10.3390/v10050259

87. Delvecchio R, Higa LM, Pezzuto P, et al. Chloroquine, an Endocytosis Blocking Agent, Inhibits Zika Virus Infection in Different Cell Models. *Viruses*. 2016;8(12). doi:10.3390/v8120322

88. Li C, Zhu X, Ji X, et al. Chloroquine, a FDA-approved Drug, Prevents Zika Virus Infection and its Associated Congenital Microcephaly in Mice. *EBioMedicine*. 2017;24:189-194. doi:10.1016/j.ebiom.2017.09.034

89. Zhang S, Yi C, Li C, et al. Chloroquine inhibits endosomal viral RNA release and autophagy-dependent viral replication and effectively prevents maternal to fetal transmission of Zika virus. *Antiviral Res*. 2019;169:104547. doi:10.1016/j.antiviral.2019.104547

90. Bhagat R, Kaur G, Seth P. Molecular mechanisms of zika virus pathogenesis: An update. *Indian J Med Res*. 2021;154(3):433-445. doi:10.4103/ijmr.IJMR_169_20

91. Ke PY. The multifaceted roles of autophagy in flavivirus-host interactions. *Int J Mol Sci*. 2018;19(12):3940. doi:10.3390/ijms19123940

92. Wu Y, Yang X, Yao Z, et al. C19orf66 interrupts Zika virus replication by inducing lysosomal degradation of viral NS3. *PLoS Negl Trop Dis*. 2020;14(3):e0008083. doi:10.1371/journal.pntd.0008083

93. Clark AE, Zhu Z, Krach F, Rich JN, Yeo GW, Spector DH. Zika virus is transmitted in neural progenitor cells via cell-to-cell spread, and infection is inhibited by the autophagy inducer trehalose. *J Virol*. 2021;95(5):10.1128/jvi.02024-20. doi:10.1128/jvi.02024-20

94. Gomez HM, Mejia Arbelaez C, Ocampo Cañas JA. A qualitative study of the experiences of pregnant women in accessing healthcare services during the Zika virus epidemic in Villavicencio, Colombia, 2015-2016. *Int J Gynaecol Obstet Off Organ Int Fed Gynaecol Obstet*. 2020;148 Suppl 2(Suppl 2):29-35. doi:10.1002/ijgo.13045

95. Aguiar RS, Pohl F, Morais GL, et al. Molecular alterations in the extracellular matrix in the brains of newborns with congenital Zika syndrome. *Sci Signal*. 2020;13(635):eaay6736. doi:10.1126/scisignal.aay6736

96. Komarasamy TV, Adnan NAA, James W, Balasubramaniam VRMT. Zika virus neuropathogenesis: the different brain cells, host factors and mechanisms involved. *Front Immunol*. 2022;13:773191. doi:10.3389/fimmu.2022.773191

97. Cranston JS, Tiene SF, Nielsen-Saines K, et al. Association between antenatal exposure to Zika virus and anatomical and neurodevelopmental abnormalities in children. *JAMA Netw Open*. 2020;3(7):e209303. doi:10.1001/jamanetworkopen.2020.9303

98. de Vries LS. Viral infections and the neonatal brain. *Semin Pediatr Neurol*. 2019;32:100769. doi:10.1016/j.spen.2019.08.005

99. Wheeler AC. Development of Infants With Congenital Zika Syndrome: What Do We Know and What Can We Expect? *Pediatrics*. 2018;141(Suppl 2):S154-S160. doi:10.1542/peds.2017-2038D

100. Mulkey SB, Arroyave-Wessel M, Peyton C, et al. Neurodevelopmental Abnormalities in Children With In Utero Zika Virus Exposure Without Congenital Zika Syndrome. *JAMA Pediatr*. 2020;174(3):269-276. doi:10.1001/jamapediatrics.2019.5204

101. Horvath AR, Abdelmalek CM, Park E, et al. A humanized mouse model system mimics prenatal Zika infection and reveals premature differentiation of neural stem cells. *BioRxiv Prepr Serv Biol*. Published online February 25, 2025:2025.02.21.639556. doi:10.1101/2025.02.21.639556

102. Chiramel AI, Best SM. Role of autophagy in Zika virus infection and pathogenesis. *Virus Res*. 2018;254:34-40. doi:10.1016/j.virusres.2017.09.006

103. Zhang ZW, Li ZL, Yuan S. The role of secretory autophagy in Zika virus transfer through the placental barrier. *Front Cell Infect Microbiol*. 2017;6. doi:https://doi.org/10.3389/fcimb.2016.00206

104. Gratton R, Agrelli A, Tricarico PM, Brandão L, Crovella S. Autophagy in Zika virus infection: a possible therapeutic target to counteract viral replication. *Int J Mol Sci*. 2019;20(5):1048. doi:10.3390/ijms20051048

105. Tiwari S. Zika virus depletes neural stem cells and evades selective autophagy by suppressing the Fanconi anemia protein FANCC. doi:https://doi.org/10.15252/embr.201949183

106. Liu B, Zhang Y, Ren H, et al. mTOR signaling regulates Zika virus replication bidirectionally through autophagy and protein translation. *J Med Virol*. 2023;95(1):e28422. doi:10.1002/jmv.28422

107. Dossou A. The Emerging Roles of mTORC1 in Macromanaging Autophagy. Published online 2019. doi:https://doi.org/10.3390/cancers11101422

108. Fedele AO, Proud CG. Chloroquine and bafilomycin A mimic lysosomal storage disorders and impair mTORC1 signalling. *Biosci Rep*. 2020;40(4):BSR20200905. doi:10.1042/BSR20200905

109. Mauthe M, Orhon I, Rocchi C, et al. Chloroquine inhibits autophagic flux by decreasing autophagosome-lysosome fusion. *Autophagy*. 2018;14(8):1435-1455. doi:10.1080/15548627.2018.1474314

110. Howell JJ, Hellberg K, Turner M, et al. Metformin Inhibits Hepatic mTORC1 Signaling via Dose-Dependent Mechanisms Involving AMPK and the TSC Complex. *Cell Metab*. 2017;25(2):463-471. doi:10.1016/j.cmet.2016.12.009

111. Kalender A, Selvaraj A, Kim SY, et al. Metformin, Independent of AMPK, Inhibits mTORC1 in a Rag GTPase-Dependent Manner. *Cell Metab*. 2010;11(5):390-401. doi:10.1016/j.cmet.2010.03.014

112. Stephenne X, Foretz M, Taleux N, et al. Metformin activates AMP-activated protein kinase in primary human hepatocytes by decreasing cellular energy status. *Diabetologia*. 2011;54(12):3101-3110. doi:10.1007/s00125-011-2311-5

113. Van Nostrand JL, Hellberg K, Luo EC, et al. AMPK regulation of Raptor and TSC2 mediate metformin effects on transcriptional control of anabolism and inflammation. *Genes Dev*. 2020;34(19-20):1330-1344. doi:10.1101/gad.339895.120

114. Belzile JP, Sabalza M, Craig M, Clark AE, Morello CS, Spector DH. Trehalose, an mTOR-Independent Inducer of Autophagy, Inhibits Human Cytomegalovirus Infection in Multiple Cell Types. *J Virol*. 2016;90(3):1259-1277. doi:10.1128/JVI.02651-15

115. Jeong SJ, Stitham J, Evans TD, et al. Trehalose causes low-grade lysosomal stress to activate TFEB and the autophagy-lysosome biogenesis response. *Autophagy*. 2021;17(11):3740-3752. doi:10.1080/15548627.2021.1896906

116. Lee HJ, Yoon YS, Lee SJ. Mechanism of neuroprotection by trehalose: controversy surrounding autophagy induction. *Cell Death Dis*. 2018;9(7):712. doi:10.1038/s41419-018-0749-9

117. Paquette M, El-Houjeiri L, C Zirden L, et al. AMPK-dependent phosphorylation is required for transcriptional activation of TFEB and TFE3. *Autophagy*. 2021;17(12):3957-3975. doi:10.1080/15548627.2021.1898748

118. Richards AB, Krakowka S, Dexter LB, et al. Trehalose: a review of properties, history of use and human tolerance, and results of multiple safety studies. *Food Chem Toxicol*. 2002;40(7):871-898. doi:10.1016/S0278-6915(02)00011-X

119. Jang SK, Hong SE, Lee DH, et al. Inhibition of mTORC1 through ATF4-induced REDD1 and Sestrin2 expression by Metformin. *BMC Cancer*. 2021;21:803. doi:10.1186/s12885-021-08346-x

120. Haidurov A, Budanov AV. Locked in Structure: Sestrin and GATOR-A Billion-Year Marriage. *Cells*. 2024;13(18):1587. doi:10.3390/cells13181587

121. Rehbein U, Prentzell MT, Cadena Sandoval M, et al. The TSC Complex-mTORC1 Axis: From Lysosomes to Stress Granules and Back. *Front Cell Dev Biol*. 2021;9:751892. doi:10.3389/fcell.2021.751892

122. Magini A, Polchi A, Urbanelli L, et al. TFEB activation promotes the recruitment of lysosomal glycohydrolases β-hexosaminidase and β-galactosidase to the plasma membrane. *Biochem Biophys Res Commun*. 2013;440(2):251-257. doi:10.1016/j.bbrc.2013.09.060

123. Napolitano G, Ballabio A. TFEB at a glance. *J Cell Sci*. 2016;129(13):2475-2481. doi:10.1242/jcs.146365

124. Ross FA, Hardie DG. Assays of Different Mechanisms of AMPK Activation, and Use of Cells Expressing Mutant AMPK to Delineate Activation Mechanisms. *Methods Mol Biol Clifton NJ*. 2025;2882:81-102. doi:10.1007/978-1-0716-4284-9_4

125. Moore BR, Page-Sharp M, Stoney JR, Ilett KF, Jago JD, Batty KT. Pharmacokinetics, Pharmacodynamics, and Allometric Scaling of Chloroquine in a Murine Malaria Model ▿ . *Antimicrob Agents Chemother*. 2011;55(8):3899-3907. doi:10.1128/AAC.00067-11

126. Morales-Carrizales DA, Gopar-Cuevas Y, Loera-Arias M de J, et al. A neuroprotective dose of trehalose is harmless to metabolic organs: comprehensive histopathological analysis of liver, pancreas, and kidney. *DARU J Pharm Sci*. 2023;31(2):135-144. doi:10.1007/s40199-023-00468-w

127. Farfan-Morales CN, Cordero-Rivera CD, Osuna-Ramos JF, et al. The antiviral effect of metformin on zika and dengue virus infection. *Sci Rep*. 2021;11(1):8743. doi:10.1038/s41598-021-87707-9

128. Liu X, Chhipa RR, Pooya S, et al. Discrete mechanisms of mTOR and cell cycle regulation by AMPK agonists independent of AMPK. *Proc Natl Acad Sci U S A*. 2014;111(4):E435-444. doi:10.1073/pnas.1311121111

129. Lu G, Wu Z, Shang J, Xie Z, Chen C, Zhang C. The effects of metformin on autophagy. *Biomed Pharmacother Biomedecine Pharmacother*. 2021;137:111286. doi:10.1016/j.biopha.2021.111286

130. Zhou P, Zhang Q, Yang Y, et al. Cleavage of SQSTM1/p62 by the Zika virus protease NS2B3 prevents autophagic degradation of viral NS3 and NS5 proteins. *Autophagy*. 2024;20(12):2769-2784. doi:10.1080/15548627.2024.2390810

131. Qin ZL, Yao QF, Zhao P, Ren H, Qi ZT. Zika virus infection triggers lipophagy by stimulating the AMPK-ULK1 signaling in human hepatoma cells. *Front Cell Infect Microbiol*. 2022;12:959029. doi:10.3389/fcimb.2022.959029

132. Wang X, Zheng X, Ge H, et al. Metformin as antiviral therapy protects hyperglycemic and diabetic patients. *mBio*. 2025;16(6):e0063425. doi:10.1128/mbio.00634-25

133. Ahmad F, Kumar P, Singh P, Joshi T, Singh PK. Zika virus impairs autophagic flux in trabecular meshwork, and inhibition of autophagy restricts ocular viral transmission and associated pathology. *Microbiol Spectr*. 2025;13(10):e0103425. doi:10.1128/spectrum.01034-25

134. Geng Y, Kohli L, Klocke BJ, Roth KA. Chloroquine-induced autophagic vacuole accumulation and cell death in glioma cells is p53 independent. *Neuro-Oncol*. 2010;12(5):473-481. doi:10.1093/neuonc/nop048

135. Parisien JP, Lenoir JJ, Alvarado G, Horvath CM. The Human STAT2 Coiled-Coil Domain Contains a Degron for Zika Virus Interferon Evasion. *J Virol*. 2022;96(1):e0130121. doi:10.1128/JVI.01301-21

136. Rochette L, Dogon G, Rigal E, Zeller M, Cottin Y, Vergely C. Lipid Peroxidation and Iron Metabolism: Two Corner Stones in the Homeostasis Control of Ferroptosis. *Int J Mol Sci*. 2022;24(1):449. doi:10.3390/ijms24010449

137. Shah R, Shchepinov MS, Pratt DA. Resolving the Role of Lipoxygenases in the Initiation and Execution of Ferroptosis. *ACS Cent Sci*. 2018;4(3):387-396. doi:10.1021/acscentsci.7b00589

138. Singh B, Bhaskar S. Methods for Detection of Autophagy in Mammalian Cells. *Methods Mol Biol*. 2019;2045:245-258. doi:10.1007/7651_2018_190

139. Hill D, Cosgarea I, Reynolds N, Lovat P, Armstrong J. Research Techniques Made Simple: Analysis of Autophagy in the Skin. *J Invest Dermatol*. 2021;141(1):5-9.e1. doi:10.1016/j.jid.2020.10.004

140. Sciarretta S, Yee D, Nagarajan N, et al. Trehalose-Induced Activation of Autophagy Improves Cardiac Remodeling After Myocardial Infarction. *J Am Coll Cardiol*. 2018;71(18):1999-2010. doi:10.1016/j.jacc.2018.02.066

141. Buckingham EM, Carpenter JE, Jackson W, Grose C. Autophagy and the effects of its inhibition on varicella-zoster virus glycoprotein biosynthesis and infectivity. *J Virol*. 2014;88(2):890-902. doi:10.1128/JVI.02646-13